University of Nebraska - Lincoln
DigitalCommons@University of Nebraska - Lincoln

Theses, Dissertations, and Student Research: Department of Physics and Astronomy

Physics and Astronomy, Department of

2017

THE ORGANIC FERROELECTRIC VINYLIDENE FLUORIDE OLIGOMER: VACUUM DEPOSITION, PROPERTIES, AND INTERFACES

Keith Foreman
University of Nebraska-Lincoln, keith.foreman@unl.edu

Follow this and additional works at: https://digitalcommons.unl.edu/physicsdiss

Part of the Condensed Matter Physics Commons

Foreman, Keith, "THE ORGANIC FERROELECTRIC VINYLIDENE FLUORIDE OLIGOMER: VACUUM DEPOSITION, PROPERTIES, AND INTERFACES" (2017). *Theses, Dissertations, and Student Research: Department of Physics and Astronomy*. 36.
https://digitalcommons.unl.edu/physicsdiss/36

This Article is brought to you for free and open access by the Physics and Astronomy, Department of at DigitalCommons@University of Nebraska - Lincoln. It has been accepted for inclusion in Theses, Dissertations, and Student Research: Department of Physics and Astronomy by an authorized administrator of DigitalCommons@University of Nebraska - Lincoln.

THE ORGANIC FERROELECTRIC VINYLIDENE FLUORIDE OLIGOMER:

VACUUM DEPOSITION, PROPERTIES, AND INTERFACES

by

Keith Foreman

A DISSERTATION

Presented to the Faculty of

The Graduate College at the University of Nebraska

In Partial Fulfillment of Requirements

For the Degree of Doctor of Philosophy

Major: Physics and Astronomy

Under the Supervision of Professor Shireen Adenwalla

Lincoln, Nebraska

May, 2017

THE ORGANIC FERROELECTRIC VINYLIDENE FLUORIDE OLIGOMER:

VACUUM DEPOSITION, PROPERTIES, AND INTERFACES

Keith Foreman, Ph.D.

University of Nebraska, 2017

Advisor: Shireen Adenwalla

Organic ferroelectric materials combine the versatility and customizability afforded by organic synthesis with the functionality of ferroelectric materials. The model ferroelectric polymer, poly(vinylidene fluoride) (PVDF), is used in a wide variety of applications and is still the subject of fundamental research nearly 80 years after it was first polymerized. Unfortunately, PVDF suffers from thermal decomposition during thin film evaporation in vacuum. Since PVDF thin films cannot be deposited in the ferroelectric phase in vacuum conditions, its use in new, 21st century technologies may be limited since the interface between the organic and adjacent metallic thin films is less than pristine.

Thin films of the VDF oligomer, which is comprised of short, well-defined chains of the $–CH_2CF_2–$ monomer, *can* be deposited in the ferroelectric phase in vacuum conditions. The work in this dissertation establishes the VDF oligomer as a viable organic ferroelectric material suitable for use in modern organic-based electronics.

This dissertation describes the design, construction, and operation of a novel thermal evaporator capable meeting the demanding set of vacuum deposition parameters of the VDF oligomer. Also described is the optimization of those deposition parameters

to maximize the quality and yield of the VDF oligomer thin films. A wide battery of experimental techniques are used to definitively establish that vacuum deposition preserves the interface between the VDF oligomer and thin films of Co, an important high Curie temperature ferromagnetic metal. Several important physical properties and characteristics of VDF oligomer thin films are reported with particular emphasis on the ferroelectric properties of the films, including: the temperature and thickness dependence of the coercive field, spontaneous polarization, and the stability of the remanent polarization. Compelling evidence for the existence of the ferroelectric-to-paraelectric phase transition is also presented. Lastly, the remaining challenges and possible future experiments using the VDF oligomer are discussed.

ACKNOWLEDGEMENTS

There are many people who I must thank for their support and encouragement throughout my time as a graduate student at UNL, all of whom helped me more than they know.

First, I must thank my advisor, Professor Shireen Adenwalla. Her never-ending support and encouragement kept me on track when I was convinced that I did not have what it takes to succeed. She deftly balances the role of advisor between the appropriate amount of direction and the freedom to explore. She is the physicist I aspire to be and I am a better person for having known her.

I would like to thank Professor Stephen Ducharme, Professor Axel Enders, Professor Evgeny Tsymbal, and Professor Li Tan for serving on my Supervisory Committee. In particular, I would like to thank Professor Ducharme, not only for generously allowing me extensive use of his laboratory, without which this research would not be possible, but also for the many helpful conversations and insights throughout my time at UNL. Furthermore, I would like to thank him for advice with regards to scientific and technical writing. His suggestions have significantly improved the quality of Chapter 6, in particular.

I would also like to thank my research group, both past and present members: Dr. Nina Hong, Dr. Abhijit Mardana, Dr. Uday Singh, Mr. Christopher Keck, Mr. Sajib Saha, Mr. Mark Shearer, and Ms. Celeste Labedz. In particular, I would like to thank Dr. Hong for her time and help regarding the ellipsometry measurements. I would especially like to thank Dr. Singh, one of the smartest and most hard working individuals I have ever met,

for many useful conversations and his willingness to always offer a helping hand in the laboratory. I also owe a tremendous debt of gratitude to Ms. Labedz. Much of the research in this dissertation was performed with her assistance. She was a true asset in the laboratory and a joy to be around. She helped me learn to be a better mentor, and taught me far more than I taught her.

I am very thankful for my fellow graduate students at UNL, past and present, for both contributions to the research in this dissertation and their friendship: Dr. Shashi Poddar, Dr. Jingfeng Song, Ms. Elena Echeverria, and Dr. Mak Koten among many others. I am especially grateful for the friendships of Mr. Nathan Clayburn and Mr. Evan Brunkow. For hours of studying together, debating useful physics, providing valuable suggestions in the laboratory, and simply being there to lean on during the stressful times of graduate student life, I am forever indebted to them.

I would also like to thank all of the support staff, past and present, in the Department of Physics and Astronomy at UNL: administrative staff – Cyndy Peterson, Jennifer Becic, Amanda Lager Gleason, Patty Fleek, Kim Schaaf, Joyce McNeil, Verona Skomski, Jocelyn Bosley, Theresa Sis, and Kay Haley; electricians – Anatoly Mironov, Brian Farleigh, and Dr. John Kelty; machinists – Keith Placek, Pat Pribil, Bob Rhynalds, and Mike Thompson. In particular, I would like to thank Keith Placek for all of his help with the evaporator described in Chapter 3.

I am also very grateful for my time as an undergraduate at Buena Vista University, a time in my life that I look back upon fondly. For guiding me along my first steps as a scientist, I would like to thank Professor Nasser Dastrange, Professor Benjamin Donath, Professor Richard Lampe, Professor Lisa Mellmann, Professor Timothy Ehler,

and Professor Shawn Stone. In particular, I would like to thank Professor Ehler for giving me my first laboratory research experience and Professor Stone for his constant support and encouragement, even throughout my time as a graduate student.

I would be remiss if I did not also thank the American Taxpayers. The research in this dissertation was made possible by funding from the National Science Foundation (NSF) through Grant No. ECCS-1101256 and by the NSF through the Nebraska Materials Research Science and Engineering Center Grant No. DMR-1420645. This research was performed in part in the Nebraska Nanoscale Facility and the Nebraska Center for Materials and Nanoscience, which are supported by the NSF through Grant No. ECCS-1542182 and the Nebraska Research Initiative. This research may one day lead to useful technologies. Nevertheless, I will endeavor to repay this debt through responsible citizenship and positive contributions to society.

Finally, but above all others, I must thank my family. This would not be possible without them. This achievement is as much theirs as it is mine. For my parents' unwavering love and support, I am grateful. They have helped me to stay the course and have been a constant source of encouragement and inspiration. Their hard work and sacrifice has allowed me to pursue my goals, and for that I am forever thankful. For my wonderful wife, Morgan, I could not have reached this accomplishment without her selflessness, patience, and constant love. She has been an unending source of strength and has always been there when I needed her. I could not imagine having a better partner in life. I love you, Morgan.

Table of Contents

List of Figures ………………………………………………………………………… iv

List of Tables ……………………………………………………………………...….. xiv

List of Digital Videos ……………………………………………………...…….. xv

Acronyms and Abbreviations ……………………………………………...… xvi

Chapter 1: Introduction ……………………………………………………………….. 1

1.1 Introduction ………………………..……………………………………… 1

1.2 Brief Review of Magnetism ……………………………………………….. 4

1.3 Brief Review of Ferroelectricity …………………………………………… 14

1.4 Poly- and Oligo- Vinylidene Fluoride ……………………...…………… 18

1.5 References ………………………………………………………..……… 23

Chapter 2: Sample Preparation and Characterization Techniques …..…..…..…… 28

2.1 Introduction ……………………..…………………………………….. 28

2.2 Magnetron Sputtering ……………………………………………………… 29

2.3 Thermal Evaporation ……………………………...……………….. 34

2.4 Thermal Annealing …………………………..………………………….. 36

2.5 Atomic Force Microscopy and Piezoresponse Force Microscopy …….…... 37

2.6 X-ray Diffraction ……………...……………………………………… 41

2.7 Magneto-Optic Kerr Effect ………………..…………………………….. 47

2.8 Pyroelectric Current Measurements …………………..…….…………… 55

2.9 X-ray Photoelectron Spectroscopy ………………………………………… 59

2.10 Scanning Transmission Electron Microscopy ……………………………. 65

2.11 Spectroscopic Ellipsometry …………………………………………………. 67

2.12 Differential Scanning Calorimetry …………………………………….…. 72

2.13 References ………………………………………………………...…. 75

Chapter 3: Organic Ferroelectric Evaporator with Substrate Cooling and *in situ* Transport Capabilities …………………………………………………..………… 79

3.1 Introduction ………………………………………………………………… 79

3.2 Design and Construction …………………………………………...…. 81

3.3 Operation and Performance ………………………………...……… 93

3.4 Conclusions ………………………………………………………………… 97

3.5 Acknowledgements ……………………………………………………... 98

3.6 References ………………………………………..…………………… 99

Chapter 4: Ferroelectric Characterization and Growth Optimization of Thermally Evaporated Vinylidene Fluoride Thin Films ……………………….…………… 102

4.1 Introduction ……………………………………….…………………. 102

4.2 Sample Preparation and Experimental Techniques ………………………. 105

4.3 Results and Discussion …………………………………………………… 108

4.4 Conclusions ……………………………………………….…………. 133

4.5 Acknowledgements ………………………………….……………. 134

4.6 References ……………………………………………………..…….. 135

Chapter 5: The Metal/Organic Interface in Cobalt/Vinylidene Fluoride Heterostructures ……………………………………………………………….. 140

5.1 Introduction …………………………………………………...…… 140

5.2 Sample Preparation and Experimental Methods ……………..………… 142

5.3 Results and Discussion ………………………………………………… 144

5.4 Conclusions ………………………………………………………………. 164

5.5 Acknowledgements ……………………………………………………… 165

5.6 References ……………………………………………………………… 165

Chapter 6: Ferroelectricity and the Phase Transition in Large Area Evaporated Vinylidene Fluoride Oligomer Thin Films ……………………………………… 170

6.1 Introduction ………………………………………………………………. 170

6.2 Sample Preparation and Experimental Methods ………………………… 173

6.3 Results and Discussion …………………………………………………… 175

6.4 Conclusions ………………………………………………………………. 187

6.5 Acknowledgements ……………………………………………………… 188

6.6 References ……………………………………………………………… 188

Chapter 7: The Future of the Vinylidene Fluoride Oligomer: Remaining Challenges, Future Experiments, and Possible Applications ……………………………………… 192

7.1 Introduction ………………………………………………………………. 192

7.2 Remaining Challenges and Questions Concerning the VDF Oligomer 192

7.3 Magnetoelectric Coupling …………………………………………………… 195

7.4 Polarized Neutron Reflectometry ………………………………………… 198

7.5 Ferroelectric Tunnel Junctions …………………………………………… 201

7.6 Conclusions ………………………………………………………………. 203

7.7 References ……………………………………………………………… 204

Appendix A: X-ray Photoelectron Spectroscopy Data Analysis ………………… 206

Appendix B: Select Presentations ……………………………………………… 210

List of Figures

Figure 1.1 …………………………………………………………………………….. 6

Simple illustration of the diamagnetic response in materials.

Figure 1.2 ………………………………………………………………………………… 7

Simple illustration of the paramagnetic response in materials.

Figure 1.3 ………………………………………………………………………………… 8

One dimensional illustrations of the spontaneous magnetic moment ordering in (a) ferromagnets, (b) antiferromagnets, and (c) ferrimagnets.

Figure 1.4 ………………………………………………………………………………… 9

Temperature dependence of the magnetic susceptibility of (a) paramagnetic and (b) ferromagnetic materials.

Figure 1.5 ……………………………………………………………………………….. 12

Illustration of ferromagnetic exchange ($J > 0$) and antiferromagnetic exchange ($J < 0$).

Figure 1.6 ……………………………………………………………………………….. 15

Euler diagram illustrating the crystal structure hierarchy of dielectric materials as it relates to polarization.

Figure 1.7 ……………………………………………………………………………….. 17

Gibbs free energy as a function of spontaneous polarization for both second- and first-order phase transitions. Figure adapted from reference 53.

Figure 1.8 ………………………………………………………………..……………. 18

Spontaneous polarization as a function for second- and first-order ferroelectric phase transitions.

Figure 1.9 ……………………………………………………………..……………….. 19

Illustrations of a segment of ferroelectric PVDF (left) and the VDF monomer (right), -CH_2CF_2-, with carbon atoms in grey, fluorine in blue, and hydrogen in white.

Figure 1.10 …………………………………………………………….……………… 20

Molecular structure of the α and β-phase chain conformations, with carbon in grey, fluorine in blue, and hydrogen in white (bond lengths not to scale). Figure adapted from reference 54.

Figure 1.11 ……………………………………………………..…………………… 21

Crystalline structure of the α and β-phase chain conformations. Figure adapted from reference 54.

Figure 2.1 ………………………………………………………………………..…….. 30

Illustration of the magnetron sputtering process.

Figure 2.2 ……………………………………………………………………..……….. 34

Calibrated deposition rates for (a) Pt and (b) Co using the Inficon XTM/2 quartz crystal deposition monitor.

Figure 2.3 ………………………………………………………………………………… 35

Illustration of a typical thermal evaporation deposition technique.

Figure 2.4 37

Typical annealing profile used in this work, as controlled by a programmable oven.

Figure 2.5 38

An illustration of the AFM setup.

Figure 2.6 42

Illustration of the diffraction of x-rays by a crystal.

Figure 2.7 44

Depiction of (a) hypothetical diffraction peak and (b) typical x-ray diffraction peak illustrating the effect of finite crystal size.

Figure 2.8 47

Three common MOKE configurations: polar, longitudinal, and transverse MOKE.

Figure 2.9 49

Illustrations of experimental setups for LMOKE and PMOKE measurements.

Figure 2.10 56

Illustration of the pyroelectric effect. Figure adapted from reference 30.

Figure 2.11 58

Illustration of the pyroelectric current measurement setup.

Figure 2.12 60

Simple illustration of the effect of photon absorption on electron energy levels.

Figure 2.13 ……………………………………………………………………….. 62

Illustration of energy level diagrams of a sample (left) and the spectrometer (right) in electrical contact. Figure adapted from reference 35.

Figure 2.14 ………………………………………………………….……………… 67

Illustration of a simple ellipsometry setup.

Figure 2.15 ……………………………………………………………………….. 68

Illustration of reflection and transmission of a plane wave at a planar interface between two media.

Figure 2.16 ……………………………………………………………...……… 72

Schematic of a typical DSC setup.

Figure 2.17 ……………………………………………………………..…………… 74

Illustration of hypothetical DSC data demonstrating a sample undergoing endothermic and exothermic reactions.

Figure 3.1 ……………………………………………………………………..…….. 82

Photograph of the organic evaporator (left)/sputtering and e-beam chamber (middle)/load lock (right) system.

Figure 3.2 ………………………………………………………………………… 83

External side view (a) and top view (b) of the organic thin film deposition chamber.

Figure 3.3 ………………………………………………………………………… 85

Side view (a) and bottom view (b) of the custom eight inch flange mounted on the bottom of the six-way cross.

Figure 3.4 …………………………………………………………………………………… 86

Photograph of the effusion cells atop the water cooled mount. The effusion cell housing is removed in the photograph.

Figure 3.5 …………………………………………………………………………………… 88

Side view (a) and top view (b) of the custom eight inch flange mounted on the top of the six-way cross.

Figure 3.6 …………………………………………………………...………………… 90

(a) Photograph of the substrate cooling system (b) Photograph of the assembled organic deposition system as viewed through the front window, showing the need for vertical motion. The inset of (b) provides a view of the shutter above the effusion cell housing.

Figure 3.7 ……………………………………………………………………...……. 92

(a) Photograph of the partially disassembled cassette holder showing the BeCu/Cu hangers. (b) A cassette in position within the cassette holder (as viewed from below). (c) Simple diagram showing the how the hangers perform during cassette loading.

Figure 3.8 ……………………………………………………………..………….. 94

Substrate temperature versus time for both cooling and warming cycles.

Figure 3.9 ……………………………………………………………..………….. 96

Deposition rate (blue), total thickness (black), and crucible temperature (green) as functions of time.

Figure 3.10 97

Pyroelectric hysteresis loop collected from a VDF oligomer thin film grown in the deposition system described here.

Figure 4.1 107

(Left) VDF oligomer structure. The β-phase chain conformation shown results in ferroelectric ordering. (Center) An electric dipole moment forms across the carbon chain, directed from the highly electronegative F atoms to the H atoms. (Right) Sample structure: glass (1 mm)/Pt (50 nm)/Co (1.2 nm)/VDF (t nm)/Al (20 nm).

Figure 4.2 109

XRD data for the as-grown VDF oligomer thin film.

Figure 4.3 111

AFM measurements, photographs, and pyroelectric hysteresis loops from rough and smooth samples.

Figure 4.4 114

Illustration of roughness induced sample failure.

Figure 4.5 115

(a) Histogram showing the numbers of successful and unsuccessful samples as a function of maximum peak-to-valley distance, Δz. (b) Δz as a function of crucible temperature during deposition.

Figure 4.6 117

(a) Map of the ordinary component of the index of refraction over a large area for a VDF oligomer thin film measured using ellipsometry. The top

left corner corresponds to the edge of the sample. (b) VDF oligomer film thickness map across the same area. The inset is a cross section of this map with a $1/r^2$ fit in red.

Figure 4.7 ……………………………………………………………………..…… 119

Two typical sample architectures with (a) small area and (b) large area electrodes.

Figure 4.8 ……………………………………………………………………..……. 121

Pyroelectric current as a function of temperature.

Figure 4.9 ……………………………………………………………………..……. 123

Still frames from digital video 4.1, a movie of a VDF oligomer thin film on a Pt/Co electrode being heated.

Figure 4.10 ……………………………………………………………..…………….. 126

Room temperature XRD data (from top to bottom) for an as-grown, unannealed VDF oligomer thin film, after annealing at 68 °C for 90 minutes, after heating at 75 °C, after heating at 98 °C, and for a blank Si substrate for reference.

Figure 4.11 ……………………………………………………...……………………. 132

(a) VDF oligomer thin film switching voltage as a function of film thickness. (b) VDF oligomer thin film pyroelectric hysteresis loops for various film temperatures. (c) Coercive field measurements as a function of temperature.

Figure 5.1 ……………………………………………………………………………. 147

Time dependence of PMOKE magnetic hysteresis loops for the Co/VDF heterostructures shown in the insets.

Figure 5.2 ……………………………………………………………………………. 151

Magnetic signatures obtained from the hysteresis loops shown in figure 5.1.

Figure 5.3 ……………………………………………………………………………. 153

Thickness dependence of the VDF oligomer's ability to preserve the magnetic properties of a Co thin film.

Figure 5.4 ……………………………………………………………………………. 154

PMOKE as a function of time demonstrating that a VDF oligomer film as thin as 15 nm is capable of preserving the magnetic properties of the Co.

Figure 5.5 ……………………………………………………………………………. 156

Line scans across the metal/organic interface from elemental composition maps of Co/VDF heterostructures acquired with STEM.

Figure 5.6 ……………………………………………………………………………. 158

Co(2p) XPS spectra of Co/VDF heterostructures.

Figure 5.7 ……………………………………………………………………………. 162

F(1s) peak location as a function of VDF oligomer film depth for both exposed and all-vacuum deposited Co/VDF heterostructures.

Figure 6.1 ……………………………………………………………………………. 176

(a) Heating (black and blue) and cooling (red and cyan) calorimetry measurements. (b) Pyroelectric current as a function of substrate

temperature from a 100-nm thick VDF oligomer film. (c) Capacitance as a function of substrate temperature from a 200-nm thick VDF oligomer film.

Figure 6.2 179

(a) Capacitance and (b) loss tangent for three consecutive voltage loops, demonstrating the characteristic butterfly loops of ferroelectric materials, for a 200-nm thick VDF oligomer film. (c) Current as a function of voltage for a 200-nm thick VDF oligomer film. (d) Background corrected XRD peak of an as-deposited VDF oligomer thin film (fit in red).

Figure 6.3 182

(a) Hysteresis in the pyroelectric response from a 175-nm thick VDF oligomer film. (b) Pyroelectric current as a function of time at the negative remanent state (i.e., at zero voltage).

Figure 6.4 184

(a)-(d) PFM measurements of topography (left), piezoelectric response (PR) amplitude (center), and PR phase (right) from VDF oligomer thin films under various ac (red) and dc (green) bias conditions. Local (e) PR phase and (f) PR amplitude demonstrating clear hysteretic behavior. (g) An illustration of ferroelectric domain writing with a PFM tip, as demonstrated in part (d).

Figure 7.1 194

(a) AFM image of VDF oligomer thin film surface. (b) AFM image of LB deposited polyethylene surface atop the VDF oligomer film in part (a). (c)

Illustration of possible sample cross-section depicted a smooth top electrode.

Figure 7.2 197

Demonstration of magnetoelectric coupling in Co/VDF oligomer heterostructures.

Figure 7.3 200

(a) PNR profile for a Co/VDF oligomer heterostructure with in-plane Co magnetization. (b) PNR profile for a Co/VDF oligomer heterostructure with out-of-plane Co magnetization. (c) spin asymmetry calculated from the simulations in parts (a) and (b).

Figure 7.4 202

Demonstration of resistance dependence on VDF oligomer polarization, possibly due to the TER effect. Linear fits are shown in blue.

Figure A.1 207

Peak extraction for Co(2p) spectra collected close to the Co/Pt interface. (a) Example of Co(2p) spectrum, both as-collected (black) and smoothed (red). (b) First derivative of as-collected (black) and smoothed (red) spectrum. (c) First derivative smoothed Co(2p) spectrum (black) and Gaussian fit (red).

Figure A.2 208

XPS spectra of Pt(4f) peaks.

Figure A.3 209

XPS spectra of F(1s) peaks.

List of Tables

Table 1.1 …………………………………………………………………..……… 22

Crystallographic parameters for the α and β-phase chain conformations [54, 60].

Table 2.1 …………………………………………………………………………….. 53

Important specific PEM retardation amplitudes, φ_0, in radians. This value is a user-defined setting on the PEM controller.

Table 4.1 ……………………………………………………………………………… 128

Tabulated results of XRD and AFM measurements before and after various annealing conditions.

List of Digital Videos

Digital Video 4.1 122

A movie of a VDF oligomer thin film heated from room temperature to 81 °C. The film clearly starts to melt starting at 75 °C. The movie can be viewed at https://www.youtube.com/watch?v=0OrAySUlU0I

Acronyms & Abbreviations

ac	Alternating Current
AES	Auger Electron Spectroscopy
AFM	Atomic Force Microscope/Microscopy OR
	Antiferromagnetic/Antiferromagnet/Antiferromagnetism
CF	ConFlat
C-V	Capacitance-Voltage
dc	Direct Current
DSC	Differential Scanning Calorimetry
EDS	Energy-Dispersive Spectroscopy
FET	Field-Effect Transistor
FM	Ferromagnetic/Ferromagnet/Ferromagnetism
FTJ	Ferroelectric Tunnel Junction
FWHM	Full-Width Half Maximum
HAADF	High-Angle Annular Dark Field
ICDD	International Center for Diffraction Data
I-V	Current-Voltage
LB	Langmuir-Blodgett
LG	Landau-Ginzburg
LMOKE	Longitudinal Magneto-Optic Kerr Effect
MOKE	Magneto-Optic Kerr Effect
MRSEC	Materials Research Science and Engineering Center

MTJ	Magnetic Tunnel Junction
NCMN	Nebraska Center for Materials and Nanoscience
NSF	National Science Foundation
OFHC	Oxygen-Free, High Thermal Conductivity
OLED	Organic Light-Emitting Diode
PEM	Photoelastic Modulator
PFM	Piezoresponse Force Microscope/Microscopy
PMOKE	Polar Magneto-Optic Kerr Effect
PNR	Polarized Neutron Reflectometry
PVDF	Poly(Vinylidene Fluoride)
P(VDF-TrFE)	Poly(Vinylidene Fluoride-Trifluoroethylene)
RAM	Random-Access Memory
RF	Radio Frequency
RMS	Root Mean Square
STEM	Scanning Transmission Electron Microscopy
TER	Tunneling Electroresistance
TrFE	Trifluoroethylene
VDF	Vinylidene Fluoride
XPS	X-ray Photoelectron Spectroscopy
XRD	X-ray Diffraction

CHAPTER 1

INTRODUCTION

1.1 Introduction

Since the development of the first organic light emitted diodes (OLEDs) by Tang and Van Slyke in 1987 [1], interest in organic electronics has exploded. In fact, the latest market projections indicate the value of the organic electronics market share will exceed $73 billion by 2027, up from under $30 billion in 2017 [2]. Indeed, OLED-based displays have become commonplace items. Reasons for this increased interest in organic-based electronics stem from the advantages they provide over inorganics, including versatility and ease of processing, low weight, and mechanical flexibility [3-8]. Perhaps the biggest reason, however, is the practically unlimited customizability of organic molecules [7, 9]. Organic molecules can be specifically selected, or designed, to suit specific needs for particular applications. For example, organic chemists and materials engineers have become quite proficient at determining molecular conformations and energy levels, thus facilitating optimization of energy level alignment and charge carrier transport across devices [7, 9, 10].

The advantages provided by organic materials, coupled with ever improving molecular design capabilities, have led to organic materials becoming integral components of numerous technologies [5, 6, 8]. Extending beyond light emission, organic materials are now employed in transistors [5, 11, 12], photovoltaics [13-16], antireflection coatings [17], flexible/stretchable electronics [11, 18-21], sensors [22-24], and the rapidly growing area of spintronics [25-27].

Ferroelectricity, which is discussed in more detail in Section 1.3, is an important physical phenomenon of great interest for investigations of fundamental physics and technological applications. Ferroelectricity was first experimentally observed in 1920 [28], and interest in technological applications of ferroelectric materials intensified during World War II. When the supply of mica was severed by German U-boats, the United States required replacement, high-dielectric permittivity materials for use in capacitors, and perovskite ferroelectrics, such as $BaTiO_3$, met those demands [29, 30]. Today, ferroelectric materials are used in a wide range of devices and applications including transducers [31, 32], tunable capacitors [32-34], data storage [19, 32, 35], electro-optic devices [32, 36], and sensors [32, 37, 38]. Ferroelectric materials are still the subject of novel, cutting-edge research as well. Recently, for example, ferroelectric tunnel junctions that exhibit high tunneling electroresistance [39, 40] have also sparked considerable interest.

Organic ferroelectric materials combine the advantages of organic and ferroelectric materials, uniting the processing advantageous and customizability of organic synthesis with the functionality of ferroelectric materials. For example, non-destructive readout, non-volatile ferroelectric random access memory (FeRAM) cells have been demonstrated using organic ferroelectric thin films [41].

Poly(vinylidene fluoride) (PVDF) is one of the most famous examples of an organic ferroelectric material and is widely used in applications (PVDF and related materials are discussed in more detail in Section 1.4). PVDF and its copolymers (in particular, its copolymers with trifluoroethylene (TrFE)) exhibit many properties that make them well-suited for applications including high piezoelectricity, low weight, high

corrosion resistance, chemical inertness, a flexible carbon backbone, and a high dipole moment to name a few (see "Why Ferroelectric Polyvinylidene Fluoride is Special" by M. Poulson and S. Ducharme [42]).

For all the boons that PVDF and its copolymers offer, however, there is one crucial drawback: PVDF thin films cannot be deposited in vacuum. Instead, PVDF thin films are commonly deposited via techniques such as Langmuir-Blodgett deposition [43, 44] or spin coating [41, 45], methods that expose the sample to ambient conditions during the deposition process. An essential facet to all modern organic electronics is the interface between the organic material and adjacent layers [9], i.e. metallic electrodes necessary to enable device functionality. Unfortunately, the ambient deposition methods used for PVDF thin films will compromise the quality of the interface between the organic material and metallic electrodes, thus hindering the applicability PVDF in next generation, frontier devices. For example, the quality of the metal-organic interface can affect charge injection and spin lifetime in spintronics [9, 25, 27, 46].

The VDF oligomer, short well-defined chains of the vinylidene fluoride monomer, shares many similar properties with PVDF. Unlike the polymer, however, VDF oligomer thin films *can* be deposited in vacuum, a key advantage. Despite this advantage, the VDF oligomer has not been thoroughly studied, nor is it widely used in technological applications (if at all).

The work in this dissertation endeavors to establish the VDF oligomer as a viable ferroelectric organic material suitable for use in advanced, 21st century organic electronic devices. This objective is accomplished by: (1) demonstrating that ferroelectric VDF oligomer thin films can, in fact, be deposited in vacuum conditions, (2) optimizing the

deposition parameters, (3) confirming that vacuum deposition preserves interfacial cleanliness, (4) reporting, for the first time, several physical properties and characteristics of VDF oligomer thin films, (5) establishing the existence of the ferroelectric-to-paraelectric phase transition in VDF oligomer thin films, (6) characterizing ferroelectricity in VDF oligomer thin films with large areas, suitable for device production, and (7) providing experimental proof-of-concept measurements for several potential applications of the VDF oligomer.

The remainder of this chapter introduces and reviews important concepts related to the work in this dissertation. Two particularly important physical phenomena related to this work are reviewed: magnetism and ferroelectricity. Lastly, PVDF and the VDF oligomer, the principal material investigated here, are introduced.

1.2 Brief Review of Magnetism

Both historically and scientifically, magnetism has proven to be a physical phenomenon of paramount importance. The magnetization, $\vec{M}$, of materials is defined as the magnetic dipole moment per unit volume, and was first observed long ago in lodestones. Magnetization has been exploited in devices ranging from the compasses of antiquity to the state-of-the-art magnetic memory devices of the 21st century [47-49].

At an atomic scale, the source of the magnetic moment is closely linked to the orbital ($\vec{L}$) and spin ($\vec{S}$) angular momentum of electrons, and as such, is quantum mechanical in origin (the moment created by nuclear spin is often ignored, as it is far smaller than the electronic moment [48]). There are several distinct forms of magnetism, or types of magnetic ordering. Magnetic susceptibility, χ, given by [48]:

$$\chi = M/H \tag{1.1}$$

describes the magnetization induced within a material in response to an externally applied field. Magnetic susceptibility can be used to delineate various types of magnetic ordering.

A material with a negative susceptibility exhibits diamagnetism. In this case, an external magnetic field induces a small magnetic moment in the opposite direction of the field, as shown in figure 1.1. Although quantum mechanical in origin, a simple heuristic explanation of diamagnetism is as follows: orbiting electrons experience a Lorentz force when in the presence of an external magnetic field, and via Lenz's Law, this force decreases the orbital moments aligned parallel to the field while increases those aligned antiparallel to the field. Strictly speaking, diamagnetism is a property of all matter. However, diamagnetic *behavior* is relatively weak by comparison and is only observed in materials that do not exhibit any other form of magnetic ordering (materials in which there are no unpaired electrons, and $\vec{L}$ and $\vec{S}$ are zero). Therefore, materials that *only* exhibit diamagnetism are referred to as having diamagnetic ordering [47-49].

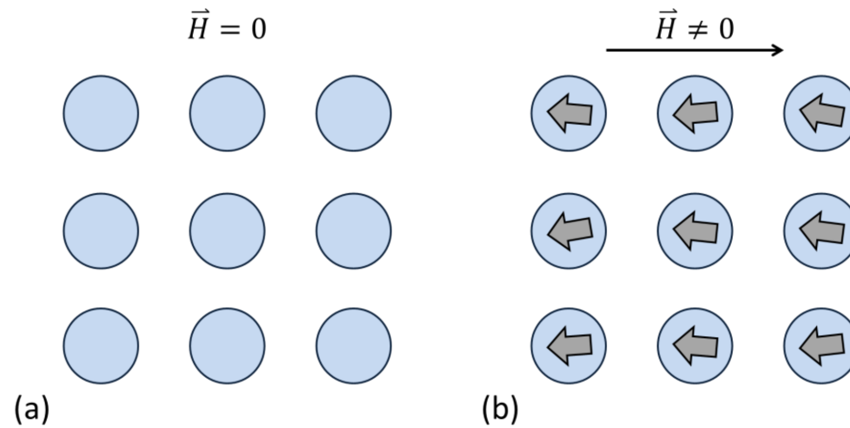

Figure 1.1: Simple illustration of the diamagnetic response in materials. A small, bulk magnetic moment forms opposite the direction of an externally applied field.

Materials with a (small) positive magnetic susceptibility exhibit paramagnetic ordering. In contrast to diamagnetism, in the case of paramagnetism, materials are attracted to an externally applied field. Here, materials with unpaired electrons have randomly oriented magnetic moments when no external field is present. However, when an external field is applied, the moments align in the direction of the field, as shown in figure 1.2 [47-49].

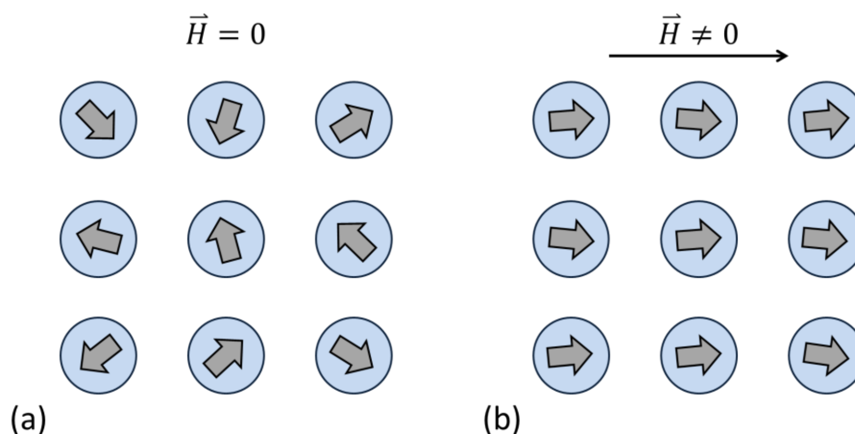

Figure 1.2: Simple illustration of the paramagnetic response in materials. Randomly oriented magnetic moments associated with unpaired electrons become ordered in the presence of an external field and result in a small, net moment parallel to the field.

In the above cases, net magnetic ordering only occurs in response to an external magnetic field. Certain materials can, however, exhibit a non-zero spontaneous magnetic ordering even in the absence of a magnetic field. Arguably the most important of these materials, by any measurable metric, are ferromagnetic materials. For transition metal ferromagnets (Co, Fe, Ni), the magnetization is primarily due to unpaired spins. Etymologically, the prefix ferro- derives from the Latin noun *ferrum*, meaning iron. As mentioned above, ferromagnetism was first observed in lodestones, a naturally magnetized piece of manganite, an iron based mineral. However, ferromagnetic ordering is not restricted to iron-based materials.

The spontaneous magnetization exists due to the regular arrangement of neighboring magnetic moments, the cause of which is discussed below. In a ferromagnetic material, these neighboring moments are aligned in the same direction. In

an antiferromagnetic material, the neighboring moments are antiparallel, and as a result the bulk, net magnetization is zero. A third common type of spontaneous magnetic ordering is ferrimagnetism, in which the neighboring moments are antiparallel, but the spin moments in each direction have unequal magnitudes, thus a net moment exists. All three cases are illustrated in figure 1.3 [47-49]. Only ferromagnetism is relevant to work in this dissertation, and therefore, the remaining discussion in this section will be framed in the context of ferromagnetism.

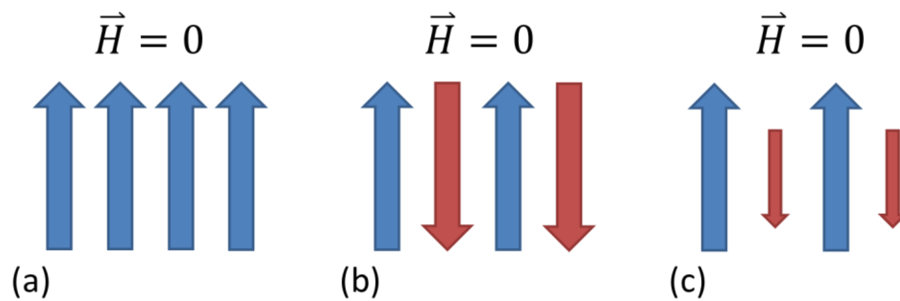

Figure 1.3: One dimensional illustrations of the spontaneous magnetic moment ordering in (a) ferromagnets, (b) antiferromagnets, and (c) ferrimagnets.

Thermal energy tends to create disorder within a system, and as such, magnetism and temperature are intimately linked. In a paramagnetic material, the temperature dependence of the magnetic susceptibility follows the Curie Law, given by [48, 50]:

$$\chi = \frac{C}{T} \tag{1.2}$$

where C is the Curie constant (a material-dependent constant) and T is the temperature. The competition between the magnetic ordering in a ferromagnet and thermal disorder results in a temperature, T_c, above which the magnetic order vanishes, called the Curie temperature. Above the Curie temperature, the susceptibility of a ferromagnet behaves like that of a paramagnetic material. This behavior can be described by the modified Curie Law for ferromagnets, called the Curie-Weiss Law, and is given by [48, 50]:

$$\chi = \frac{C}{T - T_c} \tag{1.3}$$

The temperature dependence of the magnetic susceptibility for both paramagnetic and ferromagnetic materials is shown in figure 1.4.

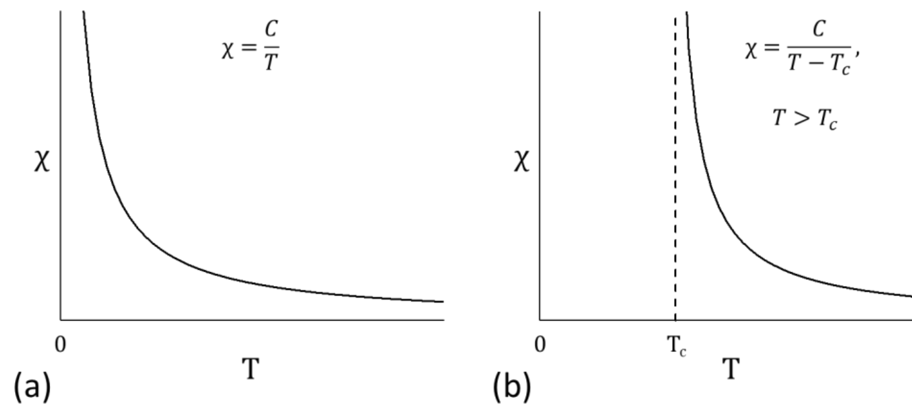

Figure 1.4: Temperature dependence of the magnetic susceptibility of (a) paramagnetic and (b) ferromagnetic materials.

The cause of the spontaneous magnetic ordering in a ferromagnetic material is the *exchange interaction*, or just *exchange*, a quantum mechanical effect with no classical analogue. An erroneous classical approach would be to explain the magnetic ordering via a magnetostatic dipole interaction, in which the field from one dipole moment causes the neighboring moment to come into alignment. However, the atomic magnetic moments are too small for this mechanism to explain ferromagnetism. In fact, it can be shown that any order created this way will be destroyed at temperatures of the order of 1 K [49].

There are numerous models of ferromagnetism and the exchange interaction (Ising model, Heisenberg model, Stoner model, RKKY model to name just a few) with entire textbooks devoted to the subject (see references 47-49 for instance). For the sake of discussion in this dissertation, it is simplest to consider two electrons. Ultimately, the competition between kinetic and Coulomb energies determines whether a spin state is ferromagnetic (FM) or antiferromagnetic (AFM), that is, parallel or antiparallel. The Pauli Exclusion Principle states that no two fermions can occupy the same quantum state. Therefore, double occupancy of an orbital is only possible for antiparallel spin states, not parallel spin states, since spin is a quantum number. For a parallel spin configuration, an electron must be in an excited, one-electron orbital. The requisite energy is supplied by the Coulomb interaction between the two electrons at coordinates $\vec{r}_1$ and $\vec{r}_2$ [49]:

$$V_C = \frac{e^2}{4\pi\epsilon_0|\vec{r}_1 - \vec{r}_2|} \tag{1.4}$$

This interaction does not depend on the spin of the electrons, but does favor the parallel spin alignment, as it is smaller for this spin state. This is true for both inter- and intra-

atomic exchange [3], but this discussion is restricted to interatomic exchange. From the Heisenberg model, the exchange constant can be calculated by comparing the total energy of the FM and AFM wave functions, given by [49]:

$$\psi_{FM}(\vec{r}_1, \vec{r}_2) = \frac{1}{\sqrt{2}}[\varphi_l(\vec{r}_1)\varphi_r(\vec{r}_2) - \varphi_r(\vec{r}_1)\varphi_l(\vec{r}_2)] \tag{1.5}$$

$$\psi_{AFM}(\vec{r}_1, \vec{r}_2) = \frac{1}{\sqrt{2}}[\varphi_l(\vec{r}_1)\varphi_r(\vec{r}_2) + \varphi_r(\vec{r}_1)\varphi_l(\vec{r}_2)] \tag{1.6}$$

where φ_l and φ_r are the atomic wave functions of the two atoms, designated "left" and "right". The energy is calculated in the usual manner:

$$E_{FM,AFM} = \int \psi^*_{FM,AFM} \hat{H}(\vec{r}_1, \vec{r}_2) \psi_{FM,AFM} dr_1^3 dr_2^3 \tag{1.7}$$

From the energies of the parallel and antiparallel states, the exchange constant, *J*, is calculated using [48, 49]:

$$J = \frac{1}{2}(E_{AFM} - E_{FM}) \tag{1.8}$$

If *J* is positive, the system favors a parallel, or ferromagnetic spin coupling, while if *J* is negative, the system favors an antiparallel, or antiferromagnetic spin coupling [48, 49], as shown in figure 1.5.

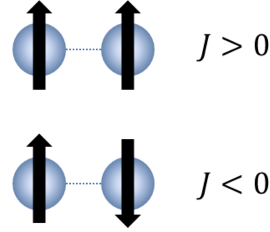

Figure 1.5: Illustration of ferromagnetic exchange ($J > 0$) and antiferromagnetic exchange ($J < 0$).

The energy of the interatomic exchange is on the order of 0.1 eV, or ~1000 K [49]. This is in agreement with experimental measurements of the Curie temperature of various ferromagnetic materials. Indeed, $T_c \approx 1400$ K for cobalt, the principal ferromagnetic material studied in this dissertation [50].

When a magnetic material is used for technological applications, the direction of the magnetization is often a crucial factor. In a magnetic system that exhibits magnetic anisotropy, the magnetization favors a natural direction called the easy axis (an anisotropic system may have one or more easy axes). This natural alignment of the spontaneous magnetization is such that the energy associated with the directional dependence, the anisotropy energy, is a minimum. The leading term of the anisotropy energy, E_a, for a uniaxial system is given by [47-49]:

$$E_a = K_u V \sin^2 \theta \tag{1.9}$$

where V is the volume, K_u is an anisotropy constant and θ is the angle between $\vec{M}$ and the easy axis. The anisotropy of a ferromagnetic material plays an important role in its

magnetic behavior. For instance, via the Stoner model, the coercive field, H_c, of a ferromagnet and the anisotropy constant are related by [47-49]:

$$H_c = \frac{2K_u}{\mu_0 M_s} \tag{1.10}$$

where M_s is the saturation magnetization and μ_0 is the permeability of free space.

There are several sources of magnetic anisotropy and the most significant will be discussed here. Shape anisotropy is an extrinsic property associated with the demagnetization field, which tends to reduce the total magnetic moment inside the material. The demagnetization field can be difficult to calculate for arbitrary shapes, but for a simple ellipsoid, the magnetostatic energy is given by [48]:

$$E_m = \frac{1}{2}\mu_0 V N M_s^2 \tag{1.11}$$

where N is the demagnetizing factor. The magnetic easy axis is along the major axis of the ellipsoid, and the shape anisotropy energy is given by [48]:

$$K_{shape} = \frac{1}{4}\mu_0 M_s^2 (1 - 3N) \tag{1.12}$$

and, as expected, is zero for a symmetric sphere ($N = 1/3$).

Magnetocrystalline anisotropy is an intrinsic property and arises from the spin-orbit interaction, an interaction between $\vec{S}$ and $\vec{L}$. Essentially, magnetocrystalline anisotropy causes a preferential spin direction with respect to the orbital shape and

orientation. The first order contribution to magnetocrystalline anisotropy is the single-ion anisotropy, in which the orbitals containing the electrons electrostatically interact with the crystal-field, the potential at the site of the orbital due to the rest of the crystal. The second order contribution is the ion-ion contribution, which arises from the interaction between dipoles (though, as mentioned above, the magnetostatic dipole interaction is quite weak). As the name suggests, the exact expression for the magnetocrystalline anisotropy energy depends on the crystal symmetry of the system [47-49].

1.3 Brief Review of Ferroelectricity

Ferroelectricity, as the name might suggest, is the electrical analogue to ferromagnetism. A ferroelectric material has a non-zero spontaneous polarization in the absence of an electric field, though the true defining feature of ferroelectricity is that this polarization is reversible with the application of an external electric field. In 1920, Valasek discovered that the electric polarization of Rochelle Salt ($NaKC_4H_4O_6 \cdot 4H_2O$) could be reversed by an externally applied electric field, resulting in a hysteresis in the polarization vs. field curve, similar to ferromagnetic hysteresis [28, 51]. Ferromagnetism was already known at this time, and so this effect was given the name ferroelectricity, although this effect has nothing to do with iron.

Crystal structure and ferroelectricity are intimately linked. The Bravais crystal classification system groups (three dimensional) crystal lattices into seven crystal groups, according to their geometry. Amongst these seven classes, there are 32 point groups, a set of symmetry operations about a fixed point in the crystal. Of these 32 crystalline point groups, 20 are non-centrosymmetric (do not contain an inversion center) and allow

piezoelectricity, the onset of a polarization upon the application of a mechanical stress. (Technically, there are 21 non-centrosymmetric point groups, but the induced charges in the cubic O(432) group cancel each other [52], and so this class is considered non-piezoelectric.) Of these 20 point groups, 10 have a unique polar direction, and thus have a spontaneous polarization. The spontaneous polarization of these polar classes can be modified with changes in temperature, and exhibit pyroelectricity (the pyroelectric effect will be discussed in more detail in Chapter 2). If the polarization of a material belonging to one of these polar classes can be reversed upon application of an electric field, the material is called a ferroelectric. Hence, all ferroelectrics belong to one of the polar classes, and show both the piezoelectric and the pyroelectric effect, as shown in figure 1.6 [50, 51, 53].

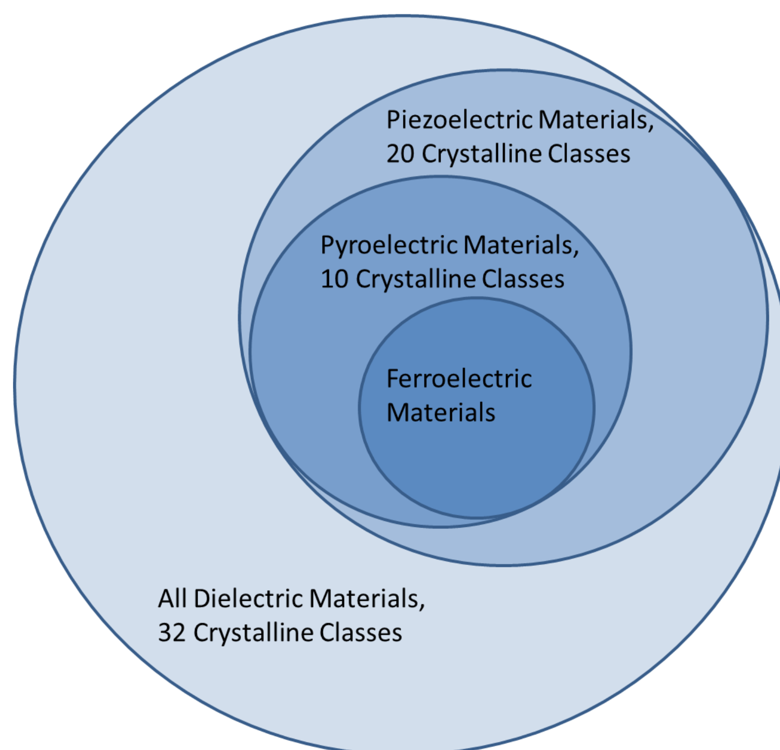

Figure 1.6: Euler diagram illustrating the crystal structure hierarchy of dielectric materials as it relates to polarization.

As with a ferromagnetic system, thermal disorder competes with ferroelectric ordering. As a result, there is a characteristic temperature, T_c, also sometimes referred to as the Curie temperature, at which the spontaneous polarization goes to zero, and above which, the material is in the paraelectric phase. According to the Landau-Devonshire-Ginzburg theory, the (strain free) Gibbs free energy, G, for a ferroelectric is given by [54]:

$$G = G_0 + \frac{1}{2}a_0(T - T_0)P^2 + \frac{1}{4}bP^4 + \frac{1}{6}cP^6 \quad (1.13)$$

where T_0 is a constant, a_0, b, and c depend on temperature and pressure, and P is the polarization (the temperature dependence of a_0 originates from the coupling between the ionic polarizability and thermal expansion [32]). The non-zero spontaneous polarization, P_s, can be calculated by minimizing the free energy [54]:

$$\left(\frac{\partial G}{\partial P}\right)_T = a_0(T - T_0)P_s + bP_s^3 + cP_s^5 = 0 \quad (1.14)$$

$$P_s^2 = \frac{-b \pm \sqrt{b^2 - 4a_0(T - T_0)c}}{2c} \quad (1.15)$$

Clearly, the spontaneous polarization depends on temperature. With equation 1.15, G vs. P_s can be plotted for various temperatures. The G vs. P_s curve changes with the sign of b, and figure 1.7 shows G vs. P_s curves at various temperatures for both signs of b.

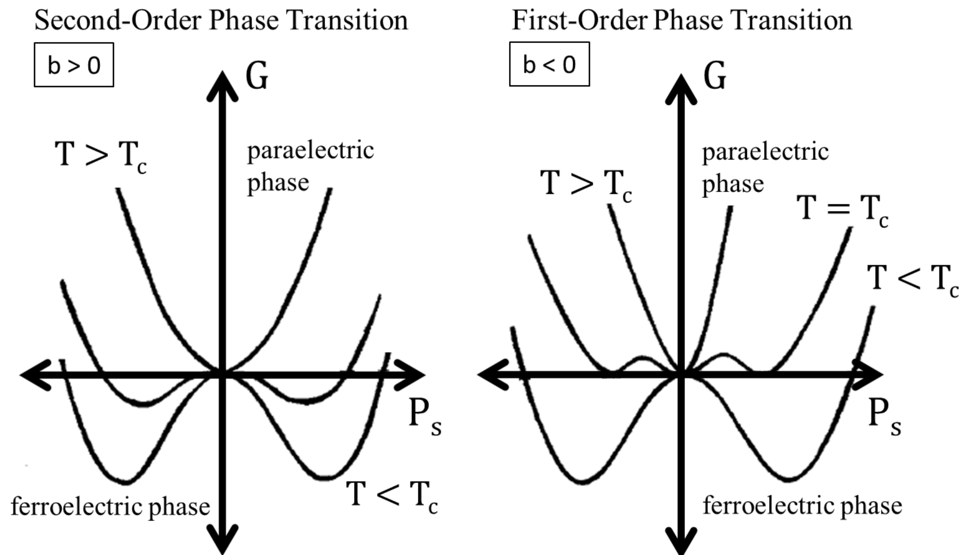

Figure 1.7: Gibbs free energy as a function of spontaneous polarization for both second- and first-order phase transitions. Figure adapted from reference 53.

For $b > 0$, G changes continuously with decreasing temperature from a curve with one minimum at $P_s = 0$ to a curve with two minimums, one above and one below $P_s = 0$. A transition of this type is called a second-order phase transition. For $b < 0$, G has one minimum at $P_s = 0$ for temperatures above T_c. However, unlike the second-order transition, at T_c there appears a state with three minima: one at $P_s = 0$, a second at $P_s > 0$, and a third at $P_s < 0$. At temperatures below T_c, the curve has one minima above and one minima below $P_s = 0$. A transition of this type is called a first order transition, and has an intermediate state where the ferroelectric and paraelectric phases exist simultaneously at T_c. The spontaneous polarization continuously drops to zero at T_c in a second-order transition, while there is an abrupt drop to zero at T_c in a first-order transition. The

temperature dependence of the spontaneous polarization is shown in figure 1.8 [50, 51, 53, 54].

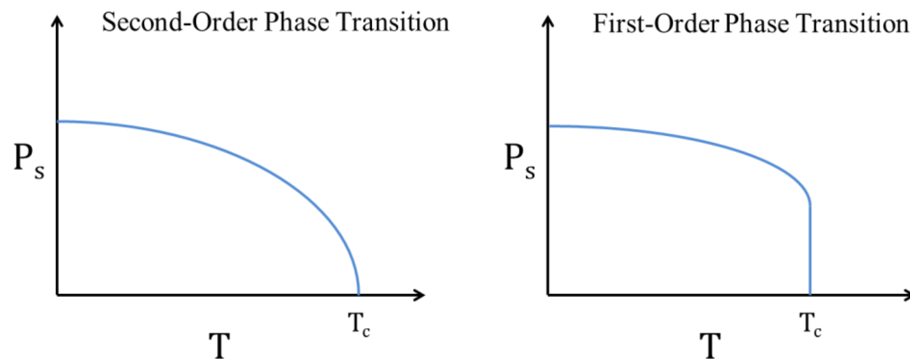

Figure 1.8: Spontaneous polarization as a function for second- and first-order ferroelectric phase transitions.

1.4 Poly- and Oligo- Vinylidene Fluoride

Poly(vinylidene fluoride) (PVDF) was first polymerized in the 1940s. Kawai discovered that PVDF exhibited a large piezoelectric effect in 1969, and by the early 1970s, ferroelectric properties in PVDF were observed [54, 55] though it would not be until the 1980s that ferroelectricity was confirmed [56, 57]. But even before the piezoelectric and ferroelectric properties of PVDF were known, it was already being used in an enormous number of applications, including as an electric insulator, in exterior finishes, and in water pipes. The piezo- and ferroelectric properties of PVDF opened up the material to a whole new range of applications. In fact, the piezoelectric panels on the dust counter of the New Horizons spacecraft utilize PVDF [58].

Ferroelectric materials can be classified as either displacive or order-disorder in character. Perovskite ferroelectrics, like $BaTiO_3$, are the canonical examples of displacive

ferroelectrics, while PVDF is a prime example of an order-disorder ferroelectric. One way to distinguish these types of ferroelectrics is the microscopic behavior in the paraelectric phase. Above the transition temperature, the unit cell of a displacive ferroelectric will have no net ionic displacement, and thus will be microscopically non-polar. In contrast, an order-disorder ferroelectric still contains a dipole moment in the unit cell above the transition temperature. However, these dipole moments will be randomly oriented, and thus the material is only non-polar over a macroscopic scale [42, 51].

The ferroelectric nature of PVDF (and the VDF oligomer) arises from the structure of the VDF monomer, $-CH_2CF_2-$, shown in figure 1.9. The monomer consists of two fluorine atoms attached to one carbon atom and two hydrogens atoms attached to the other carbon atom, while the carbon atoms themselves form the “backbone” of the polymer. A dipole moment forms across the carbon chain from the highly electronegative fluorine towards the hydrogen [54, 55].

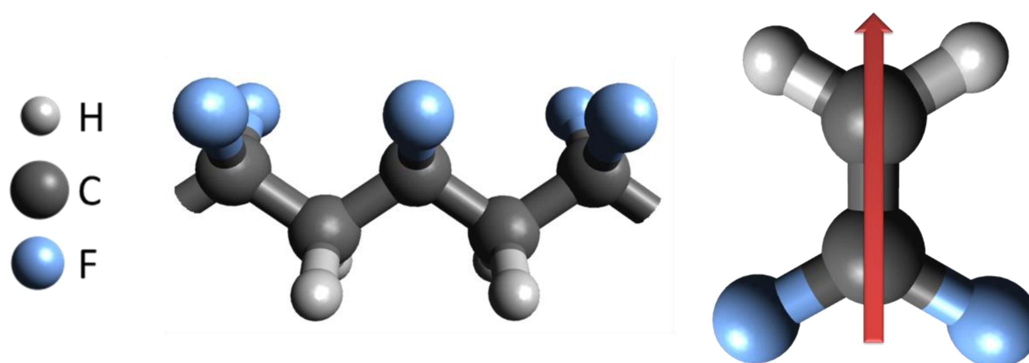

Figure 1.9: Illustrations of a segment of ferroelectric PVDF (left) and the VDF monomer (right), $-CH_2CF_2-$, with carbon atoms in grey, fluorine in blue, and hydrogen in white. A dipole moment (depicted by the red arrow) forms across the carbon chain from the electronegative fluorine to the hydrogen.

The distinguishing feature between PVDF and the VDF oligomer is the number of monomers that form the carbon chain, or degree of polymerization. While the polymer can be on the order of 10^4 monomers long [59], the VDF oligomer is made of short, well-defined chains of the -CH_2CF_2- monomer, usually between 10 and 20 monomers long.

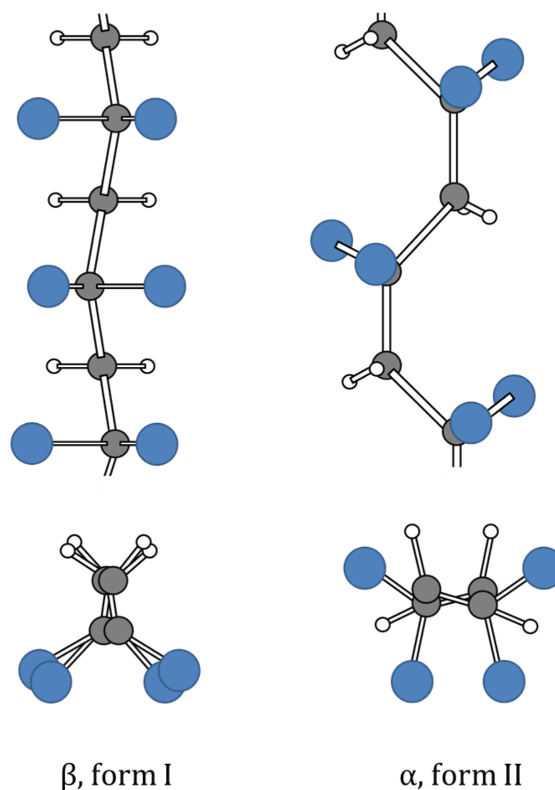

Figure 1.10: Molecular structure of the α and β-phase chain conformations, with carbon in grey, fluorine in blue, and hydrogen in white (bond lengths not to scale). Figure adapted from reference 54.

PVDF, as well as the VDF oligomer, can adopt several different chain confirmations, and not all exhibit strong ferroelectric properties. The crystalline chain conformations in order of discovery are the α, β, γ, and δ-phase, or forms II, I, III, and IV,

respectively (though, form IV is just a polar form II). Only the α and β-phase conformations are relevant the work in this dissertation, and further discussion is limited to these forms. Figure 1.10 shows "top-down" and "end-on" views of the α and β-phase chain conformations, while figure 1.9 shows a "side" view of the β-phase conformation [54, 55].

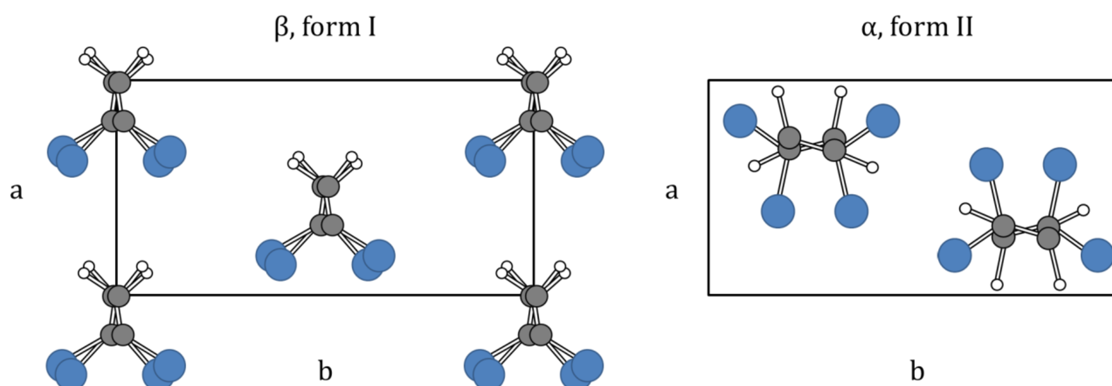

Figure 1.11: Crystalline structure of the α and β-phase chain conformations. Figure adapted from reference 54.

The unit cell of the α-phase conformation consists of opposing polar sublattices. This renders the net polarization of the α-phase conformation very low in comparison to β-phase conformation, which is polar. The crystal packing structures for the α and β-phase chain conformations are shown in figure 1.11. The unit cell of the α-phase is monoclinic with lattice parameters a = 4.96 Å, b = 9.64 Å, c (fiber axis) = 4.62 Å, and β (the angle between the a and c axes) = 90°, while the β-phase unit cell is orthorhombic with lattice parameters a = 8.58 Å, b = 4.91 Å, and c = 2.56 Å. These lattice parameters are listed in table 1.1 below [54, 55, 60].

	Unit Cell Parameters (Å)			Crystal System	Chains in Unit Cell
	a	b	C		
α, form II	4.96	9.64	4.62	monoclinic	2
β, form I	8.85	4.91	2.56	orthorhombic	2

Table 1.1: Crystallographic parameters for the α and β-phase chain conformations [54, 60].

The rest of the dissertation is organized as follows: Chapter 2 describes the sample preparation and experimental techniques used in this study. Chapter 3 describes the design, construction, and operation of a novel thermal evaporator used to deposit the thin films of the VDF oligomer studied in this work. Chapter 4 details the parameter space for successful deposition of these thin films, and reports several physical properties of the VDF oligomer. Vital to all organic electronics is the interface between the organic and adjacent metallic layers: Chapter 5 provides a thorough analysis and characterization of the metal/organic interface in Co/VDF oligomer heterostructures. Chapter 6 reports on the ferroelectric properties of the VDF oligomer, with emphasis on those properties relevant to devices, establishing the VDF oligomer as a viable organic for device applications. More importantly, compelling evidence for the ferroelectric-to-paraelectric phase transition is also presented in Chapter 6. Chapter 7 reviews the remaining challenges and presents potential applications related to the VDF oligomer using actual experimental data.

1.5 References

1. C. W. Tang and S. A. Van Slyke, Appl. Phys. Lett. **51**, 913 (1987)
2. R. Das, K. Ghaffarzadeh, G. Chansin, and X. He, *Printed, Organic & Flexible Electronics Forecasts, Players & Opportunities 2017-2027*, in: IDTechEx, 2017, available at: http://www.idtechex.com/research/reports/printed-organic-and-flexible-electronics-forecasts-players-and-opportunities-2017-2027-000510.asp
3. Z. Bao, *Polymers for Microelectronics and Nanoelectronics*, edited by Q. Lin, R. A. Pearson, and J. C. Hedrick (Oxford University Press, Oxford, 2004)
4. J. H. Lai, *Polymers for Electronic Applications*, edited by J. H. Lai (CRC Press, Inc., New York, 1989)
5. G. Horowitz, *Organic Electronics: Materials, Manufacturing and Applications*, edited by H. Klauk (WILEY-VCH Verlag GmbH & Co., Germany, 2006)
6. F. So, *Organic Electronics: Materials, Processing, Devices and Applications*, edited by F. So (CRC Press, Inc., New York, 2010)
7. A. Facchetti, Nat. Mater. **12**, 598 (2013)
8. Editorial, *Embracing the Organics World*, Nat. Mater. **12**, 591 (2013)
9. J. Hwang, A. Wan, and A. Kahn, Mater. Sci. Eng. R-Rep. **64**, 1 (2009)
10. N. J. Watkins, G. P. Kushto, and A. J. Mäkinen, J. Appl. Phys. **104**, 013712 (2008)
11. G. H. Gelinck *et al*. Nat. Mater. **3**, 106 (2004)
12. Y. Watanabe, M. Nakamura, and K. Kudo, *Organic Electronics: Materials, Processing, Devices and Applications*, edited by F. So (CRC Press, Inc., New York, 2010)

13. G. Li, V. Shrotriya, J. Huang, Y. Yao, T. Moriarty, K. Emery, and Y. Yang, Nat. Mater. **4**, 864 (2005)

14. Y. Sun, G. C. Welch, W. L. Leong, C. J. Takacs, G. C. Bazan, and A. J. Heeger, Nat. Mater. **11**, 44 (2012)

15. Y. Yang, Y. Yao, and G. Li, *Organic Electronics: Materials, Processing, Devices and Applications*, edited by F. So (CRC Press, Inc., New York, 2010)

16. J. Xue, *Organic Electronics: Materials, Processing, Devices and Applications*, edited by F. So (CRC Press, Inc., New York, 2010)

17. D. Z. Garbuzov, S. R. Forrest, A. G. Tsekoun, P. E. Burrows, V. Bulović, and M. E. Thompson, J. Appl. Phys. **80**, 4644 (1996)

18. T. Sekitani, H. Nakajima, H. Maeda, T. Fukushima, T. Aida, K. Hata, and T. Someya, Nat. Mater. **8**, 494 (2009)

19. J. Song, H. Lu, K. Foreman, S. Li, L. Tan, S. Adenwalla, A. Gruverman, and S. Ducharme, J. Mater. Chem. C **4**, 5914 (2016)

20. I. Manunza, A. Sulis, and A. Bongfiglio, Appl. Phys. Lett. **89**, 143502 (2006)

21. M.-F. Chang, P.-T. Lee, S. P. McAlister, and A. Chin, Appl. Phys. Lett. **93**, 233302 (2008)

22. A. Mardana, M. Bai, A. Baruth, S. Ducharme, and S. Adenwalla, Appl. Phys. Lett. 97, 112904 (2010)

23. R. Shinar, Y. Cai, and J. Shinar, *Organic Electronics: Materials, Processing, Devices and Applications*, edited by F. So (CRC Press, Inc., New York, 2010)

24. T. Someya and T. Sakurai, *Organic Electronics: Materials, Manufacturing and Applications*, edited by H. Klauk (WILEY-VCH Verlag GmbH & Co., Germany, 2006)

25. C. Barraud *et al*. Nat. Phys. **6**, 615 (2010)

26. V. A. Dediu, L. E. Hueso, I. Bergenti, and C. Taliani, Nat. Mater. **8**, 707 (2009)

27. M. Galbiati, *Molecular Spintronics: From Organic Semiconductors to Self-Assembled Monolayers* (Springer Theses, New York, 2016)

28. J. Valasek, Phys. Rev. **15**, 537 (1920)

29. A. Lüker, *A Short History of Ferroelectricity*, available at: http://groups.ist.utl.pt/rschwarz/rschwarzgroup_files/Ferroelectrics_files/A%20Short%20History%20of%20Ferroelectricity.pdf

30. L. E. Cross and R. E. Newnham, Ceram. Civil. **3**, 289 (1987)

31. L. E. Cross, Mater. Chem. Phys. **43**, 108 (1996)

32. K. Uchino, *Ferroelectric Devices: Second Edition* (CRC Press, Inc., New York, 2010)

33. R. Ott and R. Wördenweber, Physica C **372**, 540 (2002)

34. A. Jamil, T. S. Kalkur, and N. Cramer, IEEE Trans. Ultrason. Ferroelectr. Freq. Control 54, 222 (2007)

35. A. Q. Jiang, C. Wang, K. J. Jin, X. B. Liu, J. F. Scott, C. S. Hwang, T. A. Tang, H. B. Lu, and G. Z. Yang, Adv. Mater. **23**, 1277 (2011)

36. S. Abel *et al.* Nat. Commun. **4**, 1671 (2013)

37. D. Damjanovic, P. Muralt, and N. Setter, IEEE Sens. J. **1**, 191 (2001)

38. L. Cima, Sensor. Actuat. A-Phys. **119**, 120 (2005)

39. M. Ye. Zhuravlev, R. F. Sabirianov, S. S. Jaswal, and E. Y. Tsymbal, Phys. Rev. Lett. **94**, 246802 (2005)

40. M. Ye. Zhuravlev, Y. Wang, S. Maekawa, and E. Y. Tsymbal, Appl. Phys. Lett. **95**, 052902 (2009)

41. S. Das and J. Appenzeller, Nano Lett. **11**, 4003 (2011)

42. M. Poulsen and S. Ducharme, IEEE Trans. Dielectr. Electr. Insul. **17**, 1028 (2010)

43. A. Bune, S. Ducharme, V. Fridkin, L. Blinov, S. Palto, N. Petukhova, and S. Yudin, Appl. Phys. Lett. **67**, 3975 (1995)

44. S. E. Rickert, *Polymers for Electronic Applications*, edited by J. H. Lai (CRC Press, Inc., New York, 1989)

45. S. J. Kang, Y. J. Park, J. Sung, P. S. Jo, C. Park, K. J. Kim, and B. O. Cho, Appl. Phys. Lett. **92**, 012921 (2008)

46. M. Galbiati, S. Tatay, C. Barraud, A. V. Dediu, F. Petroff, R. Mattana, and P. Sensor, MRS Bulletin **39**, 602 (2014)

47. R. C. O'Handley, *Modern Magnetic Materials: Principles and Applications* (John Wiley & Sons, New York, 2000)

48. J. M. D. Coey, *Magnetism and Magnetic Materials* (Cambridge University Press, Cambridge, 2009)

49. R. Skomski, *Simple Models of Magnetism* (Oxford University Press, Oxford, 2008)

50. C. Kittel, *Introduction to Solid State Physics: Eighth Edition* (John Wiley & Sons, New York, 2005)

51. M. E. Lines and A. M. Glass, *Principles and Applications of Ferroelectrics and Related Materials* (Clarendon Press, Oxford, 1977)

52. A. L. Kholkin, N. A. Pertsev, and A. V. Goltsev, *Piezoelectric and Acoustic Materials for Transducer Applications*, edited by A. Safari and E. K. Akdogan (Springer Science, New York, 2008)

53. J. F. Nye, *Physical Properties of Crystals: Their Representations by Tensors and Matrices* (Clarendon Press, Oxford, 1957)

54. K. Tashiro, *Ferroelectric Polymers: Chemistry, Physics, and Applications*, edited by H. S. Nalwa (Marcel Dekker, Inc., New York, 1995)

55. R. G. Kepler, *Ferroelectric Polymers: Chemistry, Physics, and Applications*, edited by H. S. Nalwa (Marcel Dekker, Inc., New York, 1995)

56. T. Furukawa, M. Date, and E. Fukada, J. Appl. Phys. **51**, 1135 (1980)

57. T. Furukawa, Phase Transitions **18**, 143 (1989)

58. M. Horányi *et al*. Space Sci. Rev. **140**, 287 (2008)

59. Y. Koseki, K. Aimi, and S. Ando, Polym. J. **44**, 757 (2012)

60. K. Noda, K Ishida, A, Kudono, T. Horiuchi, H. Yamada, and K. Matsushige, J. Appl. Phys. **93**, 2866 (2003)

CHAPTER 2

SAMPLE PREPERATION AND CHARACTERIZATION TECHNIQUES

2.1 Introduction

This chapter introduces the sample preparation and characterization techniques used in this dissertation. Inorganic thin films were deposited using either magnetron sputtering or thermal evaporation, while the organic thin films were deposition using a custom low-temperature thermal evaporation system, discussed in detail in Chapter 3. Select samples were also thermally annealed after deposition. After preparation, samples were characterized using a wide variety of techniques. Structural characterization of the samples was primarily performed using atomic force microscopy (AFM) and x-ray diffraction (XRD). The magnetic properties of the samples were characterized using the magneto-optic Kerr effect (MOKE). The ferroelectric properties of the samples were characterized primarily using pyroelectric measurements and piezoresponse force microscopy (PFM). Other characterization techniques used in this work include x-ray photoelectron spectroscopy (XPS), scanning transmission electron microscopy (STEM), spectroscopic ellipsometry, and differential scanning calorimetry (DSC).

It is important to note that the design, construction, and operation of a low-temperature thermal evaporator capable of depositing thin films of ferroelectric VDF oligomer, as well as the deposition conditions and parameters themselves, were crucial to the work in this dissertation. Therefore, the important and original work regarding these topics is not discussed in this chapter, but rather in Chapters 3 and 4 instead.

2.2 Magnetron Sputtering

Sputtering is a popular and powerful technique that can be used to deposit both metallic and insulating thin films. Sputtering is the process of removing atoms, clusters of atoms, or molecules from a target material. The ejected material then deposits onto any surface in a line-of-sight direction with the target. Should a substrate be placed in the path of ejected target material, such as a glass slide or Si wafer in the case of this work, the ejected material will coat the substrate and form a film.

The ejection of target material is achieved via bombardment of energetic ions. A voltage is applied across a grounded sample holder and the target in contact with a cathode. As a result, an electric field is generated between the target and substrate. Meanwhile, an inert gas (Ar is used exclusively in this work) is introduced into the sputtering chamber. Free electrons are accelerated away from the cathode and collide with the Ar atoms. When the electron energy is sufficient (>15 eV), the collision is inelastic and the Ar atom is ionized, producing a plasma of Ar^+ and free electrons. The newly created Ar^+ accelerates towards the target due to the electric field. When the Ar^+ collides with the target, momentum is transferred to the target, and target material is ejected, some of which coats the substrate as desired. Control of the Ar pressure within the sputtering chamber and the cathode voltage allows for control of the deposition rate of the target material. The Ar^+, meanwhile, may recombine with a free electron, emitting a photon upon decaying to the ground state resulting in a distinctive glow [1, 2].

The process described above is sometimes called diode sputtering or just sputtering. *Magnetron* sputtering is similar to diode sputtering, except this process employs the use of permanent magnets immediately behind the target to create a

magnetic field above the target and approximately perpendicular to the applied electric field. The addition of this magnetic field serves to trap the free electrons in a helical path above the target and increases the probability that they will ionize an Ar atom (increasing the deposition rate) while also decreasing the probably that they will collide with the substrate and cause damage [3]. Magnetron sputtering is depicted in figure 2.1.

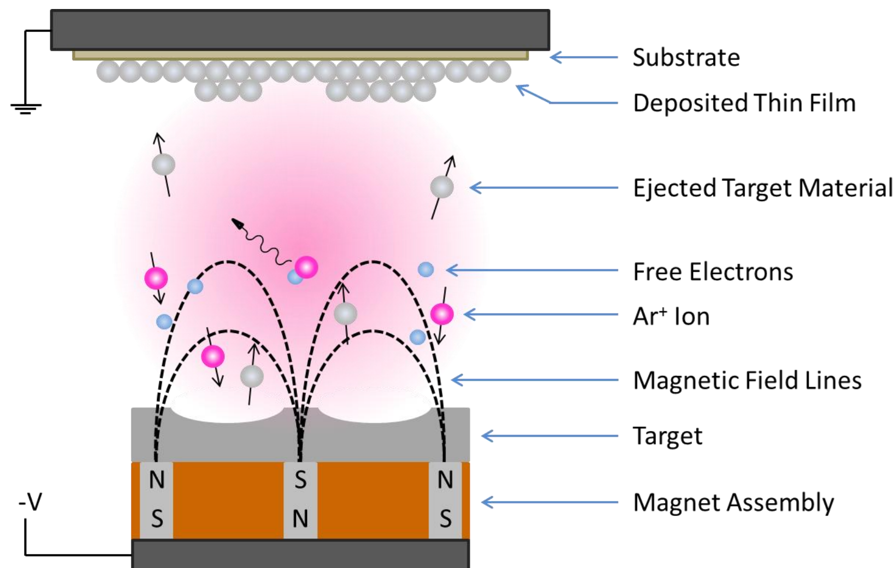

Figure 2.1: Illustration of the magnetron sputtering process. Ar atoms are ionized as a result of collisions with electrons accelerated by an electric field. The Ar^+ then accelerate toward, and collide with, the target, ejecting material. The dashed lines indicate the magnetic field due to the permanent magnets under the target, which helps contain electrons above the target, increasing ionization events and the deposition rate. The pink background represents the distinctive glow of the Ar^+ plasma.

When the target material is insulating, an applied DC voltage will lead to an accumulation of charge on the target surface. Therefore, for an insulating target, an RF voltage source is used. The choice of frequency is important, since at too low a frequency, both the electrons and Ar+ switch with each half cycle, and both the substrate and target will be bombarded. At a high enough RF frequency, the heavy Ar^+ do not respond to the RF field, and the positive charge built up on the insulating target during one half cycle can be discharged during the next half cycle. The frequency used in this work, and nearly all RF sputtering systems, is 13.56 MHz (this frequency is usually chosen due to government communications regulations [2]). Although the Ar^+ do not respond to the RF field, they must still be accelerated toward the target in order to eject material. To that end, a capacitor is placed in series with the electrode, and since the free electrons are far more mobile than the Ar^+, more electrons are collected by the electrode than Ar^+ during each cycle. After a few cycles, a sufficient DC bias is built up between the substrate and target causing the Ar^+ to accelerate toward the target. A detailed discussion on RF plasma sputtering can be found in reference 2.

The magnetron sputtering system used in this work is an AJA International ATC 2000-V with Phase II Computer Control (figure 3.1 shows a photograph of the system). This system consists of two separate chambers, a load lock and the main deposition chamber, separated by a gate valve. Both the load lock and main deposition chamber are evacuated by independent roughing and turbomolecular vacuum pumps. An automated gate valve is positioned between the main chamber and the turbo pump for precision pressure control. The base pressures of the load lock and deposition chamber are 9×10^{-8} Torr and 1×10^{-8} Torr, respectively. The load lock can hold up to six cassette substrate

holders on an elevator. A cassette can be lowered onto a transfer arm and moved into the deposition chamber through the open gate valve. This system allows for multiple depositions without breaking vacuum. In fact, the main chamber is never opened to air except for target exchange and maintenance. Furthermore, the load lock is equipped with a rotatable cassette holder that can be used to change shadow masks *in situ*. The cassettes and lock load system are described in more detail in Chapter 3.

The deposition chamber contains four sputtering guns, each equipped with a pneumatic shutter, allowing for the deposition of up to four different materials onto a substrate without breaking vacuum. Two of these sputtering guns are powered by DC sources (for metallic targets), and two by RF sources (for insulating targets). The angle of the sputtering gun and the distance between the gun and substrate can be adjusted without breaking vacuum, allowing for confocal sputtering. The cassette holder in the main chamber is capable of continuous rotation to ensure uniform substrate coating during deposition. The main deposition chamber is also equipped with an e-beam evaporation gun, but this deposition technique is not used in this work.

A mass flow controller regulates the flow of Ar into the deposition chamber. The mass flow controller combined with the automated gate valve between the deposition chamber and the vacuum pumps allows for control of the Ar pressure within the chamber during deposition. For most deposition processes, an Ar pressure 25 mTorr is maintained during the initial plasma striking, and reduced to 2 mTorr for the actual deposition. During a typical deposition of a metallic material, the DC power supply is set to 40 W, while during a typical deposition of an insulating material the RF power supply is usually set to 75-100 W. The supplied power is directly proportional to the deposition rate of the

material. It is important to note that the power ramp up/down rate needs to be quite slow for insulating targets to avoid thermal shock and subsequent cracking of the target [4]. A ramp rate per unit surface area of the sputtering target of 75 $mW/s \cdot in^2$ was used for insulating targets.

Phase II Computer Control is a proprietary LabVIEW based computer program. This program allows for simultaneous and *automated* control of the mass flow controller, pneumatic sputter gun shutters, the automated gate valve, and the DC/RF power supplies. The Phase II Computer Control program allows for precision control of deposition parameters and, as a result, high quality thin films.

The magnetron sputtering chamber is also equipped with an Inficon XTM/2 quartz crystal deposition monitor. This deposition monitor is capable of resolving and displaying deposition rates as low as 0.01 Å/s [5]. The deposition monitor is mounted on a bellows with 15 cm of travel and must be moved in to the position of the sample for use, meaning that real-time thickness monitoring is not possible. Instead, deposition rates must be calibrated prior to the actual deposition of a thin film on a substrate. This calibration is done by sputtering onto the deposition monitor for several different preset durations. A linear fit to the recorded thicknesses gives the deposition rate. Although real-time monitoring is not possible, these calibrated deposition rates are very accurate. Figure 2.2 shows the deposition rate calibrations for Pt and Co (two materials used extensively in this work) using the ideal deposition conditions described above. Once the deposition rates are measured, the thickness of a sputter deposited thin film is governed by controlling the deposition time.

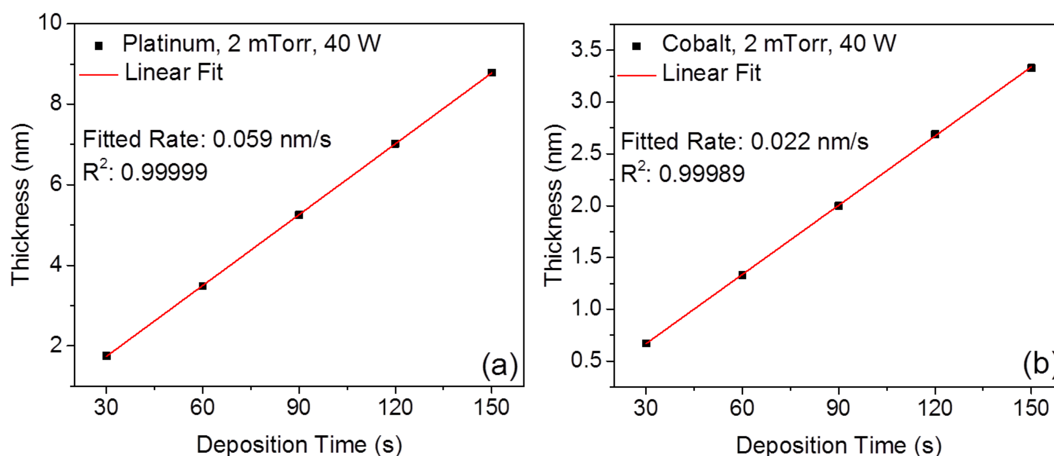

Figure 2.2: Calibrated deposition rates for (a) Pt and (b) Co using the Inficon XTM/2 quartz crystal deposition monitor. The slope of the thickness vs. time line gives the deposition rate. The red lines are linear fits to the thicknesses as a function of deposition time as measured by the quartz crystal deposition monitor.

2.3 Thermal Evaporation

For samples requiring metal contacts on a VDF oligomer thin film, thermal evaporation was used to deposit a metallic thin film rather than magnetron sputtering. The deposition source material, in this case Al shot, is loaded into a tungsten wire basket. An electric current is passed through the wire basket to heat and ultimately evaporate the source material as depicted in figure 2.3. This wire basket technique is also known as resistive evaporation. Similar to magnetron sputtering, thermal evaporation is performed in vacuum to maintain sample cleanliness and reduce scattering events, which in turn reduce the deposition rate.

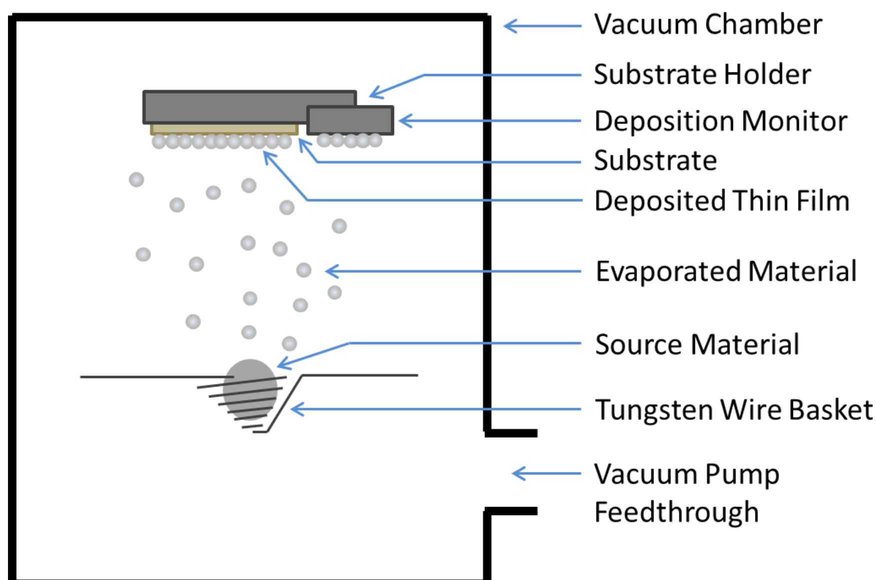

Figure 2.3: Illustration of a typical thermal evaporation deposition technique. A current is passed through a resistive wire basket to heat and evaporate source material contained within the basket onto a substrate.

Thermal evaporation was preferred over magnetron sputtering for the deposition of metallic thin films on top of VDF oligomer thin films because the energy of thermally evaporated material (<0.2 eV) is far less than that of ejected sputtered material (10-100 eV) [1, 6, 7]. The soft organic VDF oligomer thin films can far better withstand the lower energies of thermal evaporation. Indeed, many attempts were made to sputter metallic thin films on top of VDF oligomer thin films, and in each case, the sputtered material was found to have punctured through the organic film, shorting the top and bottom electrodes.

The thermal evaporator used for this work was a Bal-Tec MED 020 Coating System. Depositions were performed at pressures no higher than 3.75×10^{-5} Torr. A Sycon Instruments STM-100/MF quartz crystal deposition monitor was mounted on the substrate holder in close proximity to the substrate itself for real-time deposition rate and

thickness monitoring. A current of 10-12 A passed through the tungsten wire basket corresponded to a deposition rate 2-3 Å/s for the Al shot, which has a melting point of 660 °C.

2.4 Thermal Annealing

Thermal annealing is commonly used to improve the crystallinity of thin films. For example, thermal annealing has been found to affect the crystallinity and morphology of thin films of the copolymer poly(vinylidene fluoride-trifluoroethylene) (P(VDF-TrFE)) [8]. In general, this process involves heating the film, in a controlled manner, to a temperature above its crystallization temperature, maintaining the film at that temperature for some time, and then slowly cooling the film back to room temperature.

Select VDF oligomer thin film samples were annealed under various conditions in a Cascade TEK oven equipped with a Watlow Series 981 Programmable Temperature Controller. The temperature controller allowed for precise control over the annealing temperature, time, and ramp rates. Samples were annealed using trapezoidal temperature vs. time profiles, starting and ending at room temperature with an example profile shown in figure 2.4. Following previous work on P(VDF-TrFE) thin films, the films were annealed for no less than 1 hour, with ramp up/down rates less than 1 °C/minute. Specific annealing conditions and the effects of annealing on VDF oligomer thin films are discussed in Chapter 4.

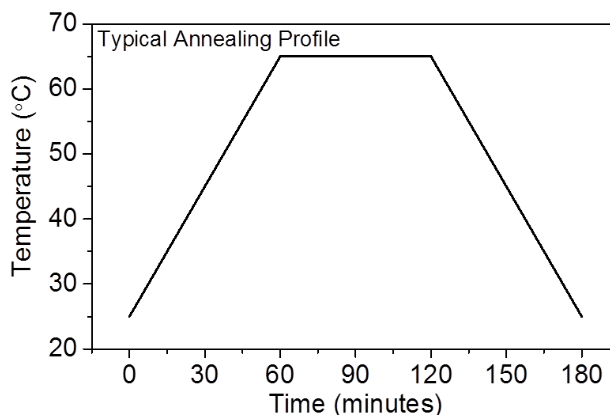

Figure 2.4: Typical annealing profile used in this work, as controlled by a programmable oven. The ramp up/down rates are equal, and kept below 1 °C/minute. The plateau temperature is held for at least one hour.

2.5 Atomic Force Microscopy and Piezoresponse Force Microscopy

First developed in the 1980s, atomic force microscopy (AFM) has become an indispensable method with which one can measure topographical features of a surface with sub-nanometer resolution, far better than the optical diffraction limit [9, 10]. A cantilever with a sharp tip, usually with a radius of curvature on the order of nanometers, is used to scan the surface of a sample. When the tip is brought within close proximity to the sample surface, forces between the tip and the sample (van der Waals forces, electrostatic forces, etc.) cause a deflection of the cantilever. These deflections can be recorded and used to map the topography of the sample.

AFM can be performed in a variety of configurations, or imaging modes, but only tapping mode was used in this work. A schematic of the AFM setup is shown in figure 2.5. While in tapping mode, the cantilever oscillates up and down and is driven at its resonance frequency by a piezoelectric transducer. The frequency and amplitude, which

can range from a few nm up to ~200 nm, are kept constant until the tip is brought close enough to the surface. The interaction between the tip and surface causes the amplitude of oscillation of the cantilever to change. The position of the tip is measured by a laser reflecting from the cantilever onto a photodiode. Feedback electronics control the height of the cantilever above the sample in order to keep the amplitude of oscillation constant as the sample surface is scanned, and a topographical image is produced by imaging the forces between the tip and surface. Tapping mode is preferred to other imaging modes, such as contact mode (in which the tip is not oscillated, but rather dragged across the surface), because the intermittent contact is less damaging to the sample surface.

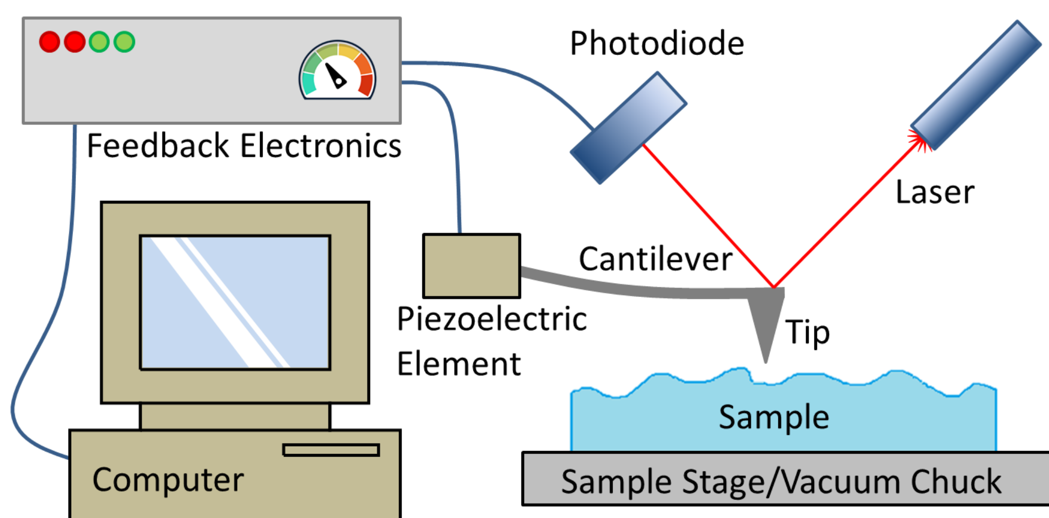

Figure 2.5: An illustration of the AFM setup. Laser light is reflected off a cantilever onto a photodiode, recording deflections in the tip due to variations in sample topography.

A Digital Instruments Nanoscope IIIa Dimension 3100 SPM system was used to perform the AFM measurements in this work [11]. Si tips with a radius of curvature of

about 6 nm and a resonance frequency of 138.26 kHz were used. Scanned areas ranged from 1×1 μm^2 to 10×10 μm^2, at scan speeds of 1-10 μm/s.

Piezoresponse force microscopy (PFM), commonly used to image and manipulate ferroelectric domains, is a variant of AFM and many of the basic principles described above apply to PFM measurements as well. PFM was introduced the early 1990s and, interestingly, the first samples to be measured via PFM were thin films of P(VDF-TrFE) [12]. Though similar to AFM, the key difference is the application of voltage across the sample. The tip itself serves as one electrode, while the sample substrate usually serves as the other. In this case, Pt thin films underneath the VDF oligomer thin films served as the bottom electrode. This technique takes advantage of the converse piezoelectric electric effect, in which an applied electric field causes strain and physical deformations in piezoelectric materials (note that all ferroelectric materials are necessarily piezoelectric). Because these displacements are usually small, the applied voltage is modulated, i.e. AC voltage, to increase the signal-to-noise ratio. The sample is deformed in response to this AC voltage and the cantilever is deflected, allowing detection of vertical, or out-of-plane, ferroelectric domains. When the polarization of the sample is parallel to the electric field, the piezoresponse of the sample is in phase with the oscillating cantilever. However, when the polarization of the sample is antiparallel to the electric field, the piezoresponse is 180° out of phase with the oscillating cantilever, meaning there is excellent contrast between these two polarization directions [13].

The strain, S, induced via the converse piezoelectric effect is given by [14]:

$$S = \frac{\Delta L}{L} = \pm d_{33} E \tag{2.1}$$

where, d_{33} is the converse piezoelectric coefficient. Domain imaging is possible due to the linear coupling between the piezoelectric coefficients and spontaneous polarization in ferroelectrics, given by [15]:

$$d_{33} = 2\varepsilon_{33}Q_{33}P_{s3} \tag{2.2}$$

for the out-of-plane direction. In equation 2.2, ε_{33} is the dielectric constant tensor and Q_{33} is the electrostriction coefficient. Application of voltage along the polar direction leads to expansion (contraction) of the sample when the electric field and polarization are parallel (anti-parallel). Solving equation 2.1 for ΔL, the expansion or contraction in the out-of-plane direction, gives:

$$\Delta L = \pm d_{33}V \tag{2.3}$$

where V is the applied voltage and the ± sign reflects the opposite piezoelectric coefficient for oppositely oriented out-of-plane domains. It is this ΔL that the cantilever detects. Note that in-plane ferroelectric domains can be detected as well since they will undergo shear deformations in response to the electric field and exert torsional forces on the cantilever. However, only out-of-plane domains were studied here.

A Bruker Dimension Icon Atomic Force Microscope in Piezoresponse Mode was used for this work [16]. Bruker SCM-PIC-V2 conductive Pt/Ir coated tips with a spring constant of 0.1 N/m were used to image out-of-plane ferroelectric domains in VDF oligomer thin films. The AC voltage frequency used was 45 kHz.

2.6 X-ray Diffraction

X-ray diffraction (XRD) is an extremely useful technique used to probe the structural properties of crystals. The atoms of a solid act as scattering sites for incident x-rays, and should these atoms be arranged in regular repeating arrays, such as in a crystalline solid, certain conditions can give rise to high intensity peaks in the scattered x-ray intensity. In 1913, the father and son team of W. H. Bragg and W. L. Bragg proposed a model to interpret the scattering of x-rays by a crystalline solid and is briefly introduced below [17].

The Braggs observed that for crystalline materials, intense peaks in the scattered x-ray intensity could be produced for certain well-defined incident angles and x-ray wavelengths. They explained this observation by considering the crystalline structure of the material as sets of parallel planes of evenly spaced atoms, as illustrated in figure 2.6. The planes of atoms are spaced a distance d apart. When (monochromatic) x-rays illuminate the solid, the atoms scatter the x-rays in all directions (though not necessarily uniformly). Some incident x-rays will be specularly reflected from adjacent atomic planes. In that case, the path length difference traveled by these two x-ray beams is $2d\sin\theta$, where θ is the angle is incidence of the x-rays, as shown in figure 2.6. If this path length difference is an integer multiple of the x-ray wavelength, the two scattering beams will constructively interfere. This condition is called Bragg Diffraction and is described by:

$$n\lambda = 2d\sin\theta \tag{2.4}$$

where λ is the wavelength of the x-rays and n is an integer. Equation 2.4 is also known as the Bragg Diffraction Condition or Braggs' Law, and the angle satisfying the equation is sometimes called the Bragg angle, θ_B. As a side note, the transmitted angle is 2θ and it is usually this angle, not θ, which is measured during a diffraction experiment [18, 19].

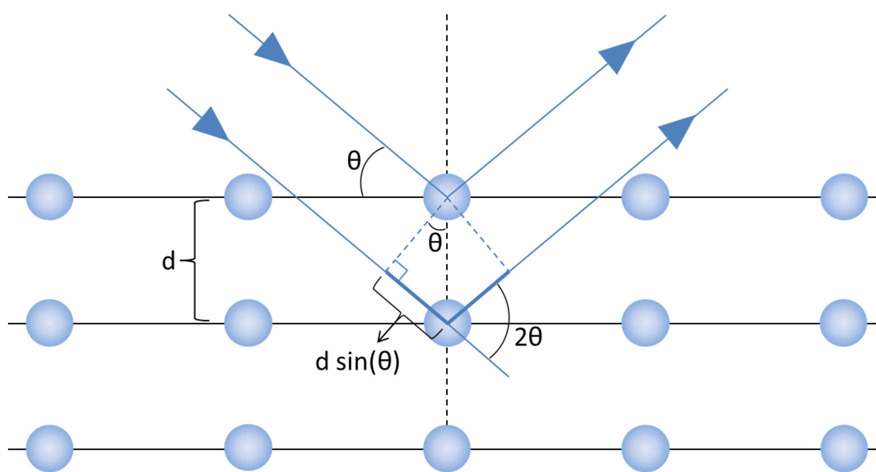

Figure 2.6: Illustration of the diffraction of x-rays by a crystal. The x-ray scattered from the lower atomic plane travels an extra distance of $2d \sin \theta$. If this extra distance equals an integer multiple of the x-ray wavelength, the two scattered x-rays will constructively interfere.

Braggs' Law sheds light on why these measurements require x-rays, and not photons with some other wavelength: in equation 2.4, $\sin \theta < 1$, and therefore $n\lambda/2d < 1$ as well. It then follows that $n\lambda < 2d$. For diffraction, the smallest value of n is 1. Therefore, for diffraction at any observable angle 2θ, the condition $\lambda < 2d$ must be satisfied. Typical values of d are on the order of 3 Å and so the wavelength of the photons used in a diffraction measurement should be less than 6 Å, making x-rays ideal candidate photons for diffraction experiments [18].

Using Braggs' Law, one can determine the distance between any two adjacent interatomic planes, as well as the orientation of the planes, since x-ray diffraction peaks occur when the scattering vector is normal to the lattice plane. It is convenient to choose a reciprocal lattice vector to represent this normal scattering vector since reciprocal lattice vectors are, by definition, normal to the set of planes. The indices of this vector are the integers h, k, and l, and are called Miller indices (hkl). A typical diffraction experiment involves finding the location of the diffraction peak in 2θ, then cross referencing this location with the International Center for Diffraction Data (ICDD) [19] to determine the orientation of the atomic planes responsible for producing the peak.

The width of the diffraction peak can also yield useful information about the crystal structure of the sample. In fact, a delta function-like diffraction peak with intensity only at the Bragg angle is a mere hypothetical for a perfect crystal with infinitely many atomic planes. Indeed, by definition, $\delta(\boldsymbol{r}) = \frac{1}{2\pi}\sum_{\boldsymbol{k}=-\infty}^{\infty} e^{i\boldsymbol{k}\cdot\boldsymbol{r}}$. The effect of the finite size of a real crystal on a diffraction peak is similar to truncating the above summation, which would result in not a delta function, but rather a peak of finite width. In reality, diffraction peaks have width as illustrated in figure 2.7. It is important to remember that just like constructive interference, destructive interference is also a result of the crystalline structure of a solid. Should the scattered x-rays from the first two atomic planes differ only slightly in phase, then the atomic plane that scatters x-rays exactly out of phase with the x-rays scattered from the first plane will lie deep within the crystal. If the crystal is too small, this requisite plane may not exist, implying that small crystals cause diffraction peak broadening [18].

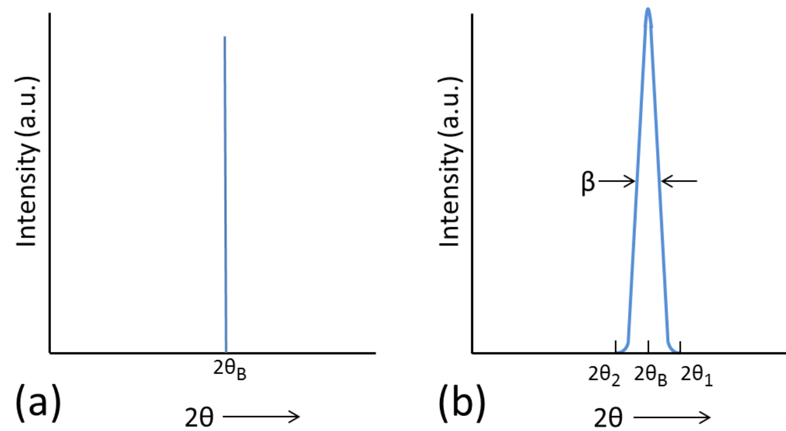

Figure 2.7: Depiction of (a) hypothetical diffraction peak and (b) typical x-ray diffraction peak illustrating the effect of finite crystal size.

The Scherrer equation relates the width of a diffraction peak with the crystallite size, and a rough derivation follows. Following the simple derivation provided by Cullity and Stock [18], consider a crystal with a total thickness τ made of m + 1 atomic planes. There exists an angle, θ_1, slightly larger than the Bragg angle for which the x-rays scattered from the surface plane are m + 1 wavelengths out of phase with those scattered from the bottom. Similarly, there exists an angle, θ_2, slightly smaller than the Bragg angle for which the x-rays scattered from the surface are m – 1 wavelengths out of phase with those scatter from the surface. In other words, θ_1 and θ_2 define the angles at which the diffraction peak goes to zero, shown in figure 2.7b. From equation 2.4:

$$2\tau \sin\theta_1 = (m+1)\lambda \tag{2.5a}$$

$$2\tau \sin\theta_2 = (m-1)\lambda \tag{2.5b}$$

By subtraction:

$$\tau(\sin\theta_1 - \sin\theta_2) = \lambda \tag{2.6}$$

With sum-to-product trigonometric identity substitution:

$$2\tau\cos\left(\frac{\theta_1+\theta_2}{2}\right)\sin\left(\frac{\theta_1-\theta_2}{2}\right) = \lambda \tag{2.7}$$

But θ_1 and θ_2 are very near θ_B, so $\theta_1 + \theta_2 \cong 2\theta_B$. Additionally, $\theta_1 - \theta_2 \ll 1$. Then, $\sin\left(\frac{\theta_1-\theta_2}{2}\right) \cong \left(\frac{\theta_1-\theta_2}{2}\right)$ and equation 2.7 can be written as:

$$2\tau\left(\frac{\theta_1-\theta_2}{2}\right)\cos\theta_B = \lambda \tag{2.8}$$

Finally, the angular width β (full-width at half maximum (FWHM) in radians), can be approximated as $\beta \cong \frac{1}{2}(2\theta_1 - 2\theta_2) = \theta_1 - \theta_2$ and equation 2.8 becomes:

$$\tau = \frac{\lambda}{\beta\cos\theta_B} \tag{2.9}$$

Usually, however, this equation appears as [18, 20]:

$$\tau = \frac{0.9\,\lambda}{\beta\cos\theta_B} \tag{2.10}$$

where the coefficient of 0.9 is called the shape factor. Equation 2.10 is the more accepted form of the Scherrer equation and gives the average crystallite size of the sample.

Finally, it useful to consider how the requisite x-rays are produced to perform a diffraction measurement. Typically, this is done with a device called an x-ray tube. The x-ray tube consists of an electron source, usually a heated filament, and electrodes. A large voltage held across the electrodes accelerates electrons towards the anode (usually Cu and sometimes Co). Bremsstrahlung radiation (braking radiation) is produced by rapidly decelerating electrons, which by conservation of energy, emit photons. However, the spectrum of the Bremsstrahlung radiation is continuous and thus filtered out by a monochromator. Alternatively, if the electrons strike the anode with sufficient energy, an electron can be ejected from the K shell of the Cu or Co anode. When an electron from an outer shell decays into this vacancy, an x-ray is produced at a specific wavelength, or characteristic line. These characteristic lines are referred to as the $K\alpha$, $K\beta$, etc. lines depending upon from where the decaying electron came. The $K\alpha$ line is the most intense and it is these x-rays that are used for diffraction experiments [18].

A Rigaku D/Max-B Diffractometer was used to carry out the XRD measurements in this work [21]. This diffractometer produced x-rays with a 1.8 kW x-ray tube with a Co anode. A monochromator removes all incident x-rays except the characteristic Co $K\alpha$ line, which has a wavelength of 1.789 Å. Diffraction data is output in ASCII format and was converted to a user-friendly format for analysis by the free-to-download PowDLL Software [22]. The Nebraska Center for Materials and Nanoscience facility has a site license and software to access the ICDD database for peak identification.

2.7 Magneto-Optic Kerr Effect

When polarized light is incident upon a magnetized medium, the polarization and ellipticity of the light may change [23]. For the transmitted portion of the incident light, this change is called the Faraday effect, while for the reflected portion, it is called the Kerr effect. The magnetic material studied in this work is metallic with a significant reflectivity. Therefore, the Kerr effect was used to measure the magnetic properties of samples discussed here. When employed in laboratory setting, magneto-optic Kerr effect measurements are colloquially referred to as MOKE measurements, or simply MOKE.

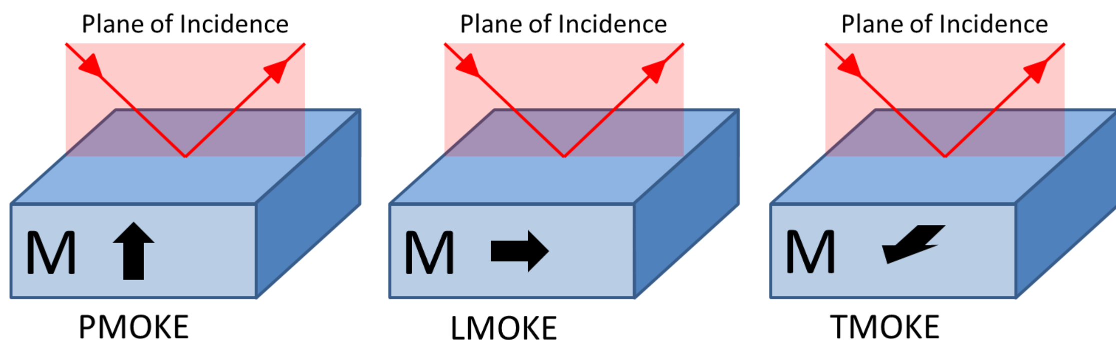

Figure 2.8: Three common MOKE configurations: polar, longitudinal, and transverse MOKE. The black and red arrows represent the magnetization direction of the sample and the propagation direction of the incident light, respectively.

MOKE measurements are used to acquire magnetic hysteresis loops. The Kerr effect is proportional to the component of magnetization along the propagation direction of the light [24]. This directional dependence means that the relative orientation of the magnetization, external magnetic field, and incident light need to be carefully considered

when performing a MOKE measurement. In general, there are three MOKE configurations used to measure the magnetic properties of a sample. The relative orientation between the magnetization of the sample and incident light are shown in figure 2.8. These three configurations are called polar MOKE (PMOKE), longitudinal MOKE (LMOKE), and transverse MOKE (TMOKE) [25]. In this work, only PMOKE and LMOKE are used to characterize samples and are described below. TMOKE, which measures the component of magnetization perpendicular to the external field, was not used in this work, and so will not be discussed any further.

LMOKE is used to measure the component of magnetization parallel to the plane of the sample, or in-plane magnetization. As shown in figure 2.8, the measured magnetization is parallel to both the sample surface and plane of incidence. Because the measured magnetization is parallel to the propagation direction of the light, the angle of incidence should be as large as possible, so as to measure the largest component of the magnetization vector. PMOKE is used to measure the component of magnetization perpendicular to the plane of the sample, or out-of-plane magnetization. As shown in figure 2.8, the measured magnetization is parallel to the plane of incidence of the light, and perpendicular to the sample surface. When performing PMOKE measurements, it is important to ensure the angle of incidence is as close to normal as possible [25].

When polarized light is reflected from the surface, the polarization direction rotates (Kerr rotation, θ_k) and the phase between the polarization components parallel and perpendicular to the plane of incidence is changed, causing a change in ellipticity (Kerr ellipticity, ε_k). These changes are due to the off-diagonal components of the Fresnel reflection tensor describing the sample, which are proportional to the magnetization (a

more formal derivation follows below) [24]. By placing a sample in an electromagnet, and using a modulated beam and lock-in amplifier, one can measure these induced polarization and ellipticity changes as a function of external magnetic field, and thus magnetic hysteresis. Typical experimental setups for LMOKE and PMOKE measurements are shown in figure 2.9.

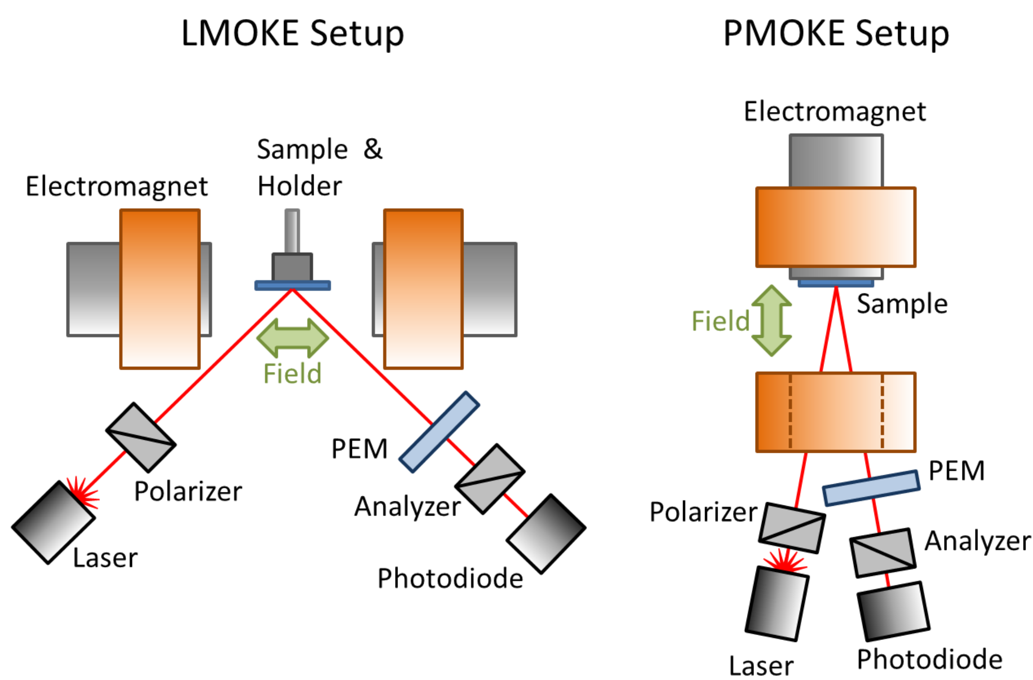

Figure 2.9: Illustrations of experimental setups for LMOKE and PMOKE measurements. Polarized light is reflected off a sample in a magnetic field. Changes in the polarization direction and ellipticity of the reflected beam (the Kerr effect) manifest as changes in intensity at the photodiode. A lock-in reads the signal detected by the photodiode at the reference frequency of the beam modulation.

Beam modulation, which allows for the use of a lock-in amplifier and thus improved signal-to-noise ratios, is usually accomplished with the use of a photoelastic modulator (PEM), which is briefly described here. The principle of operation for this device is based on the photoelastic effect. The photoelastic effect describes an induced birefringence, proportional to strain, demonstrated by some materials under mechanical stress. The optical component of the PEM used here is made of a fused silica bar attached to a quartz piezoelectric transducer. The fused silica bar vibrates at its natural resonant frequency of 50 kHz, as driven by the piezoelectric element. The optical component is therefore an oscillatory birefringent element, effectively modulating the polarization of transmitted light, allowing for the use of a lock-in amplifier referencing the frequency of oscillation [26]. Important user-defined settings on the PEM controller are discussed below.

During a MOKE experiment, the intensity of laser light reaching the photodiode (refer to figure 2.9) is the physical quantity being measured and recorded. As the polarization and ellipticity of the incident light changes upon reflection from the magnetized sample, the amount of light passing through the analyzer and reaching the photodiode changes. Since the change in polarization and ellipticity is directly proportional to the magnetization of the sample, the recorded intensity is also proportional to the magnetization of the sample. An expression for the intensity at the photodiode can be found using the Jones matrix formulism. Each optical component in the MOKE setup can be expressed by a Jones matrix [27]. If the transmission axes of the analyzer, $\boldsymbol{A}$, and polarizer, $\boldsymbol{P}$, are α and β, respectively, relative to the plane of incidence, then the matrices representing these optical components are:

$$\boldsymbol{P} = \begin{bmatrix} \cos^2\beta & \sin\beta\cos\beta \\ \sin\beta\cos\beta & \sin^2\beta \end{bmatrix} \tag{2.11a}$$

$$\boldsymbol{A} = \begin{bmatrix} \cos^2\alpha & \sin\alpha\cos\alpha \\ \sin\alpha\cos\alpha & \sin^2\alpha \end{bmatrix} \tag{2.11b}$$

The matrix used to describe the sample is a Fresnel reflection matrix. The diagonal components are the usual Fresnel reflection coefficients, while only the off-diagonal components depend on the magnetization of the sample and account for the Kerr effect. The sample matrix, $\boldsymbol{S}$, is given by [24, 27]:

$$\boldsymbol{S} = \begin{bmatrix} \tilde{r}_p & \tilde{r}_{ps} \\ \tilde{r}_{sp} & \tilde{r}_s \end{bmatrix} \tag{2.12}$$

The matrix representing the PEM, $\boldsymbol{O}$, is given by:

$$\boldsymbol{O} = \begin{bmatrix} e^{i\varphi/2} & 0 \\ 0 & e^{-i\varphi/2} \end{bmatrix} \tag{2.13}$$

Then, the amplitude of the electric field components at the photodiode are:

$$\begin{bmatrix} E_p \\ E_s \end{bmatrix}^r = \boldsymbol{AOSP} \begin{bmatrix} E_p \\ E_s \end{bmatrix}^i \tag{2.14}$$

where the superscripts *i* and *r* denote the incident and reflected beams, respectively, while the subscripts *s* and *p* denote the *s* (electric field vector perpendicular to the plane of

incidence) and p (electric field vector parallel to the plane of incidence) components of light, respectively. The intensity at the photodiode is then:

$$I \propto |E^r|^2 \tag{2.15}$$

The function of the PEM, as described above, is to modulate the polarization of the incident light, or periodic retardation of a specific component of the polarization. This time dependent retardation is characterized by $\varphi = \varphi_0 \sin \omega t$. With this expression for φ substituted into equation 2.13, along with Euler's formula, the subsequent $\sin \varphi(t)$ and $\cos \varphi(t)$ terms require Fourier decomposition and the introduction of Bessel functions. Equations 2.14 and 2.15 give the intensity at the photodiode. This analysis has been meticulously and exhaustively carried out by Polisetty et al. [27] for various angles β and α. In terms of the Kerr rotation and ellipticity, the general expression for the intensity at the photodiode is given by [25]:

$$I(t) = I_0[1 + 2\theta_k J_0(\varphi_0) - 4\varepsilon_k J_1(\varphi_0) \sin \omega t + 4\theta_k J_2(\varphi_0) \cos 2\omega t + \cdots] \tag{2.16}$$

where I_0 is the average intensity, ω is the angular frequency of the PEM, $2\pi f$, where f = 50 kHz, φ_0 is the amplitude of retardation, and J_n are the Bessel functions. Careful choice of retardation amplitude, which is a user-defined setting on the PEM controller, can extinguish or maximize the various terms in equation 2.16. These specific retardation amplitude values are shown in table 2.1 below.

	PEM Retardation Amplitude, φ_0, in radians		
	J_0	J_1	J_2
Extinguish J_n	2.405	3.872	5.136
Maximize J_n	0	1.885	3.067

Table 2.1: Important specific PEM retardation amplitudes, $\boldsymbol{\varphi_0}$, in radians. This value is a user-defined setting on the PEM controller.

The first harmonic term in equation 2.16 gives the ellipticity and the second harmonic term gives the rotation. Reading the voltage output from the photodiode from these contributions allows for a measurement of θ_k and ε_k, given by [25]:

$$\theta_k = \frac{\sqrt{2}}{4J_2}\frac{V_{2f}}{V_{DC}} \tag{2.17a}$$

$$\varepsilon_k = \frac{\sqrt{2}}{4J_1}\frac{V_{1f}}{V_{DC}} \tag{2.17b}$$

where the above expressions are the ratios of the AC and DC terms. The factor of $\sqrt{2}$ arises since the lock-in reads the rms voltage.

MOKE has several advantages over other magnetometry techniques. It is a very surface sensitive [24, 28] technique, with little background contribution from the substrate, making MOKE particularly well-suited for thin film measurements. MOKE is also capable of measuring both the in-plane and out-of-plane components of magnetization, something of which not all magnetometry techniques are capable. MOKE

is a room temperature, table top method not requiring any especially exotic hardware. Alternating gradient force magnetometry (AGFM) and superconducting quantum interference device (SQUID) magnetometry both require very specialized (i.e. expensive) equipment, and in the latter case, cryogenic refrigeration. The primary disadvantage of MOKE, is that it does not measure an absolute value of magnetization, but rather relative changes in magnetization. It is common to express MOKE data as M/M_s, magnetization normalized to the saturation magnetization.

The laser used for the MOKE measurements in this work was a Thorlabs TCLDM9 Diode Laser, with an accompanying LDC 205 B Diode Controller and TED 200 Temperature Controller. The laser power and wavelength were 1 mW and 658 nm, respectively. Newport Optics RSP-1T linear polarizers were used as the polarizer and analyzer (see figure 2.9), with $\beta = 0°$ and $\alpha = 90°$. A GMW Model 3470 Electromagnet was used to produce magnetic fields of up to 1 T. The electromagnet was powered by a Kepco BOP 50-8M Bipolar Power Supply. A Hinds Instruments PEM-90 and accompanying controller was used to modulate the laser. The photodiode was a Hinds Instruments Det-90. The photodiode signal was recorded at the PEM modulation frequency by a Stanford Research Systems SRS 830 DSP lock-in amplifier. A custom written LabVIEW program was used to record the lock-in signal as a function of supplied current to the electromagnet. A Lake Shore Cryotronics 460 Gaussmeter was used to find the linear relationship between the supplied current and magnetic field, thus calibrating the generated magnetic field.

2.8 Pyroelectric Current Measurements

Ferroelectric characterization of VDF oligomer thin films was primarily done via pyroelectric current measurements. The pyroelectric effect describes the transient charge generated by some crystalline materials upon heating or cooling [29]. This effect was first observed in certain gemstones by Theophrastus in 315 BC and has been used in technological applications since the 1960s. The pyroelectric effect differs from the thermoelectric effect as the entire crystal is subjected to the change in temperature resulting in voltage across the crystal. In contrast, the thermoelectric effect describes a permanent voltage across a material so long as a temperature gradient is held across the material.

The pyroelectric effect appears in materials with a polar point of symmetry. Of the 32 crystalline classes, 20 do not have a point of symmetry (non-centrosymmetric) and are piezoelectric. Of these 20 piezoelectric classes, 10 possess a polar point of symmetry, or are referred to as simply polar. These materials have a spontaneous polarization, P_s, with a permanent electric dipole arising from the unit cell conformation, and exhibit the pyroelectric effect. Furthermore, if the dipole can be reversed by an externally applied electric field, then the material is ferroelectric, i.e. all ferroelectrics exhibit the pyroelectric effect [29-31].

In this work, the samples in which the pyroelectric effect was measured had top and bottom metallic electrodes sandwiching the VDF oligomer (ferroelectric), that is, a parallel plate capacitor structure. Figure 2.10 demonstrates the pyroelectric effect in such a sample structure. When held at constant temperature, free charges in the metallic electrodes compensate the surface charge due to the spontaneous polarization and no

current is detected. However, when the material is heated (cooled), P_s decreases (increases) along with the bound charge. The redistribution of free charge to compensate for the change in bound charge generates a current, called the pyroelectric current. It is this current that is detected and recorded during a pyroelectric measurement [30].

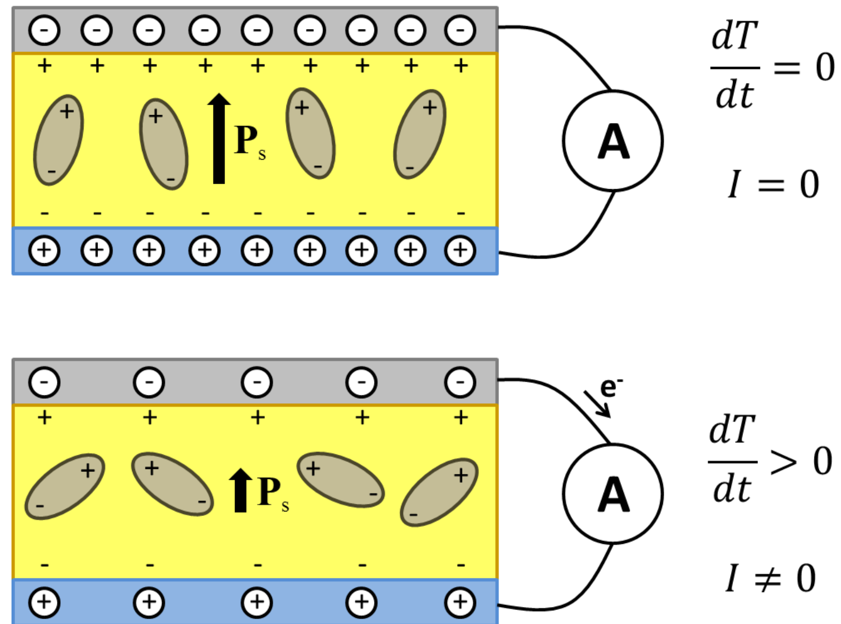

Figure 2.10: Illustration of the pyroelectric effect. When the temperature of the sample is held constant, no current is detected (top). While the temperature is changing, a pyroelectric current is generated (bottom). Figure adapted from reference 30.

The pyroelectric coefficient is defined as [31]:

$$p = \left(\frac{\partial P_S}{\partial T}\right)_{\sigma,E} \tag{2.18}$$

where (σ, E) specify constant stress and electric field. As described above, pyroelectric measurements are performed by heating/cooling the sample and recording the pyroelectric current. This current is described by:

$$I = A p_{eff} \frac{\partial T}{\partial t} \tag{2.19}$$

where, *A* is the area of the cross section of the top and bottom electrodes, or capacitor area and p_{eff} is the effective pyroelectric coefficient. Because these materials are also piezoelectric, the measured current consists of a primary contribution (pyroelectric effect) and secondary contribution (piezoelectric effect). The effective pyroelectric coefficient is given by [32]:

$$p_{3,eff} = \left(\frac{\partial P_S}{\partial T}\right)_S + \frac{d_{33}^T \alpha_3^S}{s_{33}^S} = \left(\frac{I}{A}\right)\left(\frac{\partial T}{\partial t}\right)^{-1} \tag{2.20}$$

where d_{33}^T is the stress-free piezoelectric coefficient, s_{33}^S is the elastic compliance coefficient, and α_3^S is the thermal expansion (the sample can only expand/contract in the direction perpendicular to the surface, hence the indices $_{33}$). Bune et al. showed that the pyroelectric response is directly proportional to the spontaneous polarization of the sample [32, 33]. Therefore, measuring the pyroelectric current is a suitable approach to measure the relative polarization, and more importantly the polarization hysteresis of the sample.

A. G. Chynoweth developed a useful approach to dynamically measure the pyroelectric current [34], which allows one to use a lock-in amplifier and increase the

signal-to-noise ratio. A modulated laser is used to rapidly induce small temperature changes in the sample. Chynoweth showed that although ΔT will be small using such an approach, a significant pyroelectric current can still be measured, as the current depends on the *rate of change* of T, not ΔT itself. A voltage is held across the sample for several minutes, after which the pyroelectric current is immediately recorded, which is directly proportional to the polarization. Thus, when the current saturates, the sample is completely polarized. Polarization hysteresis loops can then be produced for each electrode-enclosed area. The experimental setup, heretofore referred to as the Chynoweth method, is shown in figure 2.11. In this approach, the generated pyroelectric current is on the order of 10^{-12} A [34].

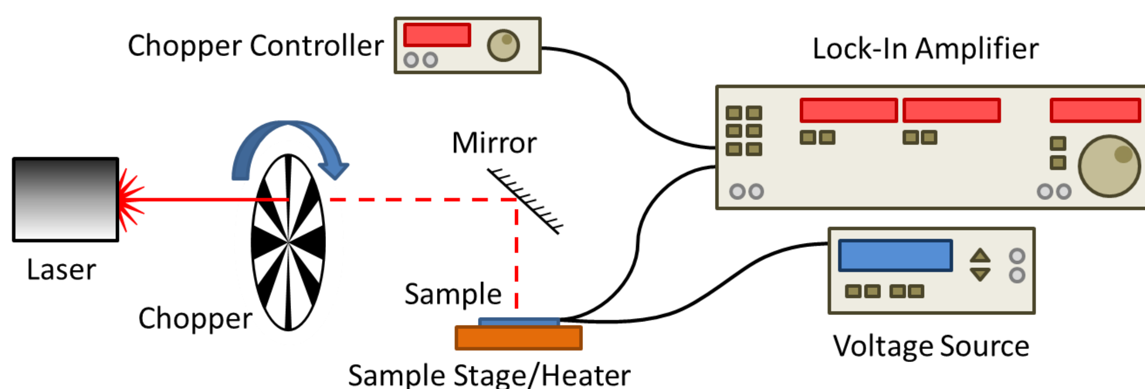

Figure 2.11: Illustration of the pyroelectric current measurement setup. Laser light is directed through an optical chopper and shown onto the sample. The resulting pyroelectric current is measured by a lock-in amplifier at the chopper frequency.

The laser used for the pyroelectric measurements in this work was a Thorlabs TCLDM9 Diode Laser, with an accompanying LDC 205 B Diode Controller and TED

200 Temperature Controller. The laser power and wavelength were 1 mW and 658 nm, respectively. A Stanford Research Systems SR540 Chopper Controller and SR541 Chopper were used to modulate the laser at a frequency of 2 kHz. The pyroelectric current was read with a Stanford Research Systems SRS 830 DSP lock-in amplifier referencing the chopper frequency. A LabVIEW controlled Keithley 2400 SourceMeter was used to supply the voltage needed to polarize the VDF oligomer. The samples were placed on a Newport Optics 462 Series XY Translation Stage for precision alignment of the electrode cross sections and the laser. A Custom Thermoelectric 12711-5L31-03CL thermoelectric heater powered by a Jameco DC 301911 Power Supply was used to optionally hold the substrate at a constant elevated temperature during the measurements (discussed further in Chapter 4). When the heater was in use, an Omega HH12 Thermocouple digital thermometer was used to monitor the temperature.

2.9 X-ray Photoelectron Spectroscopy

Also known as x-ray photoemission spectroscopy, XPS is a surface sensitive technique used to measure the elemental composition and oxidation state of the sample. Photoemission is the process in which an electron is ejected from a material upon absorption of a photon. The energy of the ejected electron is related to the state it occupied.

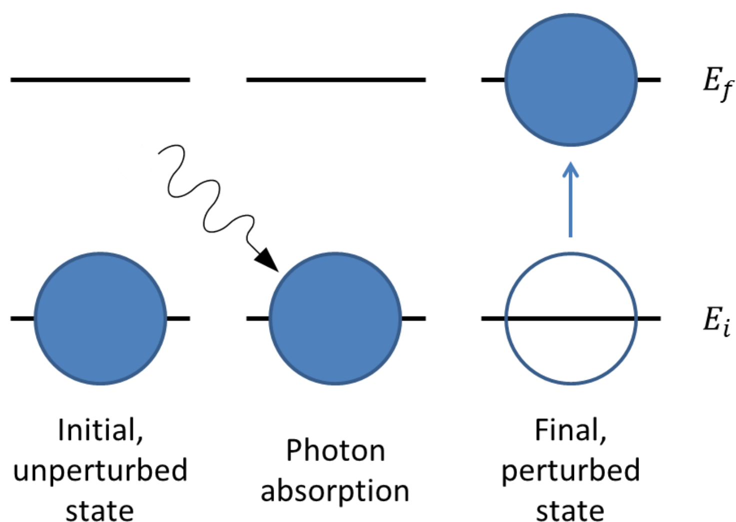

Figure 2.12: Simple illustration of the effect of photon absorption on electron energy levels. Upon atomic adsorption of a photon, an electron is excited to higher energy level. If the energy of the photon is known and the energy of the electron in the excited is measured, conservation of energy can used to calculate the energy of the electron in the initial state.

The essence of XPS is demonstrated in the energy level diagram shown in figure 2.12. An electron is initially in some unperturbed state with energy E_i, but should the atom absorb a photon (of energy $h\nu$) the electron is excited to some final state with energy E_f. From conservation of energy, the difference between the initial and final energy states should equal the energy absorbed, giving the following equation:

$$h\nu = E_f - E_i \tag{2.21}$$

If the energy of the incident photon is sufficient, the electron will be ejected from the material with some kinetic energy. It is customary to describe the degenerate final state of the electron as an expansion of its energy eigenstates:

$$\Psi_f = \sum_n c_n \Psi_n \tag{2.22}$$

where Ψ_f is the wavefunction describing the final state of the electron, the modulus square of c_n is the probability of finding the electron in the nth eigenstate, and Ψ_n is the wavefunction describing the specific final eigenstate of the electron. The reason for introducing this description is that it allows for one to write the final degenerate energy in terms of its kinetic energy, a key facet to XPS measurements [35]. The energy of the final state can now be written as:

$$E_f = E_n + E_k \tag{2.23}$$

where E_n is the energy of the electron in the nth state, and E_k is the kinetic energy of the electron. If the energy of the incident photon is sufficient to overcome the work function of the material, Φ (the energy needed to remove a delocalized electron from the surface of a material), the electron is ejected from the solid with some kinetic energy. This is described by:

$$h\nu = E_B + E_k + \Phi \tag{2.24}$$

where equation 2.23 has been substituted into equation 2.21 and $E_B = E_n - E_i$ is the binding energy of the electron. Equation 2.24 is the quintessential photoemission equation. Experimentally, one knows the energy of the incident photon and the work function, and measures the kinetic energy, thus allowing for the calculation of its binding energy.

There are difficulties, however, with attempting to directly implement equation 2.24 in a laboratory setting. First, it is not possible to directly measure E_k, and second, one would need to know the work function of each sample beforehand [35]. These problems can be resolved by considering the energy level diagrams of the sample and the spectrometer used to measure the energy of the ejected electrons, and making appropriate modifications to equation 2.24. Figure 2.13 shows such diagrams.

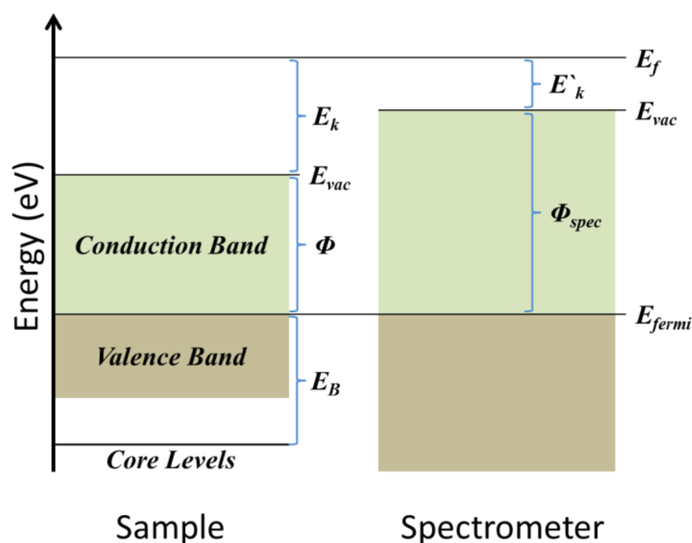

Figure 2.13: Illustration of energy level diagrams of a sample (left) and the spectrometer (right) in electrical contact. Alignment of the Fermi levels allows one to relate the binding energy of the detected electron to the measured quantity. Figure adapted from reference 35.

Here, the work function of the sample and spectrometer/analyzer is defined as the difference between the vacuum level and the Fermi level, Φ and Φ_{spec}, respectively, and the energy of the ejected electron is E_f. The analyzer measures $E`_k$, not E_k [35], making it difficult to directly implement equation 2.24. However, the sample and spectrometer are electrically connected via a common ground, and so their Fermi levels align. Therefore, from the diagram, it is clear that:

$$E_k + \Phi = E`_k + \Phi_{spec} \quad (2.25)$$

Then, equation 2.24 can be rewritten as:

$$h\nu = E`_k + E_B + \Phi_{spec} \quad (2.26)$$

Here, $E`_k$ is measured by the spectrometer and Φ_{spec} is an instrument specific constant and will not change from sample to sample. From equation 2.26, one can calculate the binding energy, E_B, of the ejected electron.

The core level electrons in different elements are subjected to different binding energies. Therefore, XPS measurements are able to distinguish one element from another by the location of the binding energy in the collected spectra. However, XPS can also distinguish between chemical compounds. When a compound is formed, the elemental atomic configuration is altered. This change in the chemical environment from which electrons are ejected is manifested as changes in the binding energy of the electrons. The

change in binding energy is called a chemical shift, and is observed in XPS spectra, making XPS a popular technique to analyze the chemical state of a specimen [35].

The successful acquisition of XPS spectra relies on the ability of the photoemitted electrons to reach the detector. Therefore, these measurements are performed in a high vacuum, as scattering events between the sample and detector are less likely to occur in such an environment. Emitted electrons must also reach the surface of the sample unimpeded, making XPS is surface sensitive technique: the probability that an ejected electron will reach the surface of the sample greatly depends on the mean free path, l, of the electrons through the sample. Beer's Law, which describes the attenuation of light propagating through a material, can be adapted to describe this behavior as well [35]:

$$I = I_0 e^{-d/l \cos\theta} \tag{2.27}$$

where I is the intensity of electrons reaching the detector from sample depth d, and θ is the angle of incidence of the x-rays (indicating that the penetration depth of the photons is also a factor). If one considers the optimal case of normal incidence ($\theta = 0°$), equation 2.27 indicates that 63% of the electrons emitted from a depth l or less will be detected without energy loss. That number falls to 23% at a depth of $2l$ and 9% at $3l$, and so 95% of the signal during an XPS experiment comes from within 3 attenuation lengths of the surface. Usually, any electron coming from a depth greater than $3l$ is considered only to contribute to noise in the spectrum [35]. A typical value for l is ~1 nm, so in general XPS probes the top ~3 nm of the sample.

XPS measurements were performed in vacuum at a pressure of 1×10^{-10} Torr to limit scattering events. Samples used for XPS measurements were deposited on Si substrates and were grounded during measurements to prevent the accumulation of charge on the sample which can cause artificial shifts in measured binding energy. The requisite x-rays are generated in much the same way as described in section 2.6, except for these measurements, the anode was Mg producing Mg Kα radiation at 1253.6 eV (energetic enough to eject core level electrons). The x-ray source was a SPECS XR50 with an accompanying XRC 1000 Source Controller. A VG Microtech VDF100AX hemispherical electron detector was used to measure the kinetic energy of the photoemitted electrons with a resolution of 2.5 eV (FWHM of F(1s) peak). Since XPS is a surface sensitive technique, samples were periodically sputter etched with Ar+ at a pressure of 1×10^{-5} Torr with a Perkin Elmer Model 04-161 2 kV Sputter Ion Gun. Spectra 8 software was used to interface with the detection equipment and collect the XPS spectra.

2.10 Scanning Transmission Electron Microscopy

Scanning transmission electron microscopy (STEM) is a type of transmission electron microscopy in which electrons pass through a sufficiently thin sample to generate very high resolution images. In 1925, De Broglie theorized the wave-like properties of particles, with the particle wavelength, or de Broglie wavelength, described by $\lambda = h/p$. The de Broglie wavelength for the electrons used in STEM measurements is far smaller than that of visible light, allowing STEM to image objects at scales far below the diffraction limit of light. In fact, STEM can collect images with atomic resolution.

STEM differs from regular transmission electron microscopy by focusing the electrons into a narrow beam and rastering the beam across the sample.

The uses of STEM extend beyond high resolution imaging. In this work, STEM was primarily used to acquire elemental maps of cross sections of the metal/organic heterostructures, and across the interface in particular. High angle, incoherently scattered electrons are very sensitive to the atomic number (Z) of the atom from which they are scattered. Therefore, the contrast in the images from these electrons is directly proportional to Z, and elemental maps can be formed as the beam is scanned across the sample. The electrons are scattered annularly and the direct (unscattered) beam is blocked from the detector, i.e. this is a dark-field method. Collectively, this technique is known as high-angle annular dark-field imaging (HAADF) [36]. Energy-dispersive x-ray spectroscopy (EDS) is often done in parallel to HAADF. This technique is used for elemental analysis via the collection of x-rays emitted from the sample. Instead of being scattered, incident electrons may also excite and eject electrons from the inner shell of an atom in the sample. When another electron decays into the vacancy, an x-ray is emitted. This process is similar to the production of x-rays discussed in section 2.6 above. The energies of the x-rays produced are characteristic of the element from which they are emitted. These energies are measured by an energy-dispersive spectrometer, from which elemental composition can be deduced [37]. When performed in parallel, HAADF and EDS can together produce quantitative elemental maps with excellent resolution.

Samples were prepared for STEM measurements in an FEI Helios NanoLab 660. Samples were first covered in a 2 μm thick C layer for protection during the milling process. A focused ion beam milling process was used to lift out slivers of the

heterostructured samples sufficiently thin enough for STEM measurements. The actual STEM measurements were performed in a 200 kV FEI Tecnai Osiris S/TEM using a single tilt sample holder [38]. Elemental maps were collected in STEM mode and quantified using tools in the Esprit software package.

2.11 Spectroscopic Ellipsometry

Spectroscopic ellipsometry, or simply ellipsometry, is an optical technique used to measure various extrinsic and intrinsic properties of thin films including but not limited to: film thickness, refractive index, surface roughness, film composition, crystallinity, anisotropy, and uniformity [39-41].

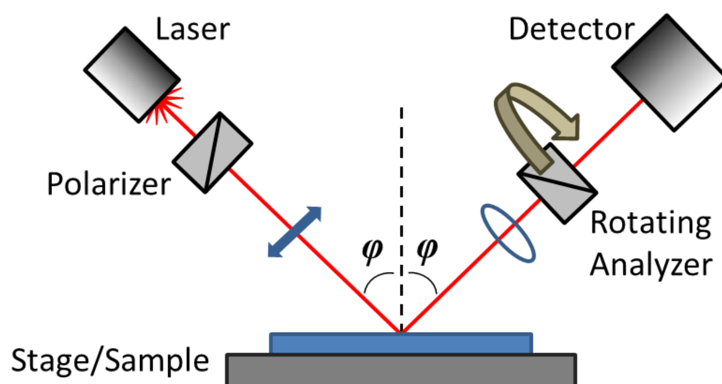

Figure 2.14: Illustration of a simple ellipsometry setup. Polarized light is reflected off a sample, and the changes in polarization state of the light are recorded and can be used to calculate various sample properties.

Most ellipsometry measurements are performed using a specular reflection setup with which one measures the change in polarization of light upon reflection from a

specimen. In some ways this technique is similar to MOKE, however standard ellipsometry measurements are related to the diagonal components of the Fresnel reflection tensor describing the sample, not the off-diagonal components. A simple ellipsometry setup is shown in figure 2.14, though many variations of that setup can be used depending upon the properties one wishes to measure. In essence, polarized light is incident upon a sample, and upon reflection the light is no longer in the same linear polarization state, but rather in some elliptical polarization state. By convention, the change in polarization is quantified by the amplitude ratio of the *s* and *p* components of the light, denoted as Ψ, and the phase difference of these components, denoted as Δ [41, 42]. By comparing the output signal of the detector against the known original polarization state, Ψ and Δ can be measured.

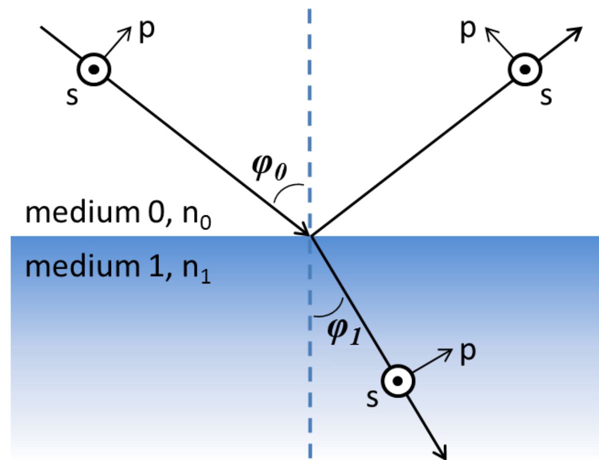

Figure 2.15: Illustration of reflection and transmission of a plane wave at a planar interface between two media.

Following conventions set at the 1968 International Conference on Ellipsometry held at the University of Nebraska-Lincoln, a brief derivation of the ellipsometry equation follows [42-44] for the simple case of a planar interface between two isotropic media, shown in figure 2.15. Snell's Law gives:

$$n_0 \sin \varphi_0 = n_1 \sin \varphi_1 \tag{2.28}$$

where $n_{0,1}$ are the indices of refraction and φ_0 and φ_1 are the angles of incidence and refraction, respectively. The Fresnel reflection coefficients are the ratios of the complex amplitudes of the incident and reflected *s* and *p* components of the electric field vectors [45]. By matching the tangential components of the ***E*** and ***H*** fields across the interface, these coefficients can be expressed as:

$$r_p \equiv \frac{E_{rp}}{E_{ip}} = \frac{n_1 \cos \varphi_0 - n_0 \cos \varphi_1}{n_1 \cos \varphi_0 + n_0 \cos \varphi_1} \tag{2.29a}$$

$$r_s \equiv \frac{E_{rs}}{E_{is}} = \frac{n_0 \cos \varphi_0 - n_1 \cos \varphi_1}{n_0 \cos \varphi_0 + n_1 \cos \varphi_1} \tag{2.29b}$$

With Snell's Law, equations 2.29a and 2.29b can be rewritten in a form that only depends on the angles of incidence and refraction:

$$r_p = \frac{\tan(\varphi_0 - \varphi_1)}{\tan(\varphi_0 + \varphi_1)} \tag{2.30a}$$

$$r_s = \frac{-\sin(\varphi_0 - \varphi_1)}{\sin(\varphi_0 + \varphi_1)} \tag{2.30b}$$

As mentioned above, ellipsometry measures the changes in amplitude and phase of the reflected wave, and so it is conventional to rewrite equations 2.30a and 2.30b as [43]:

$$r_p = |r_p| e^{i\delta_{rp}} \tag{2.31a}$$

$$r_s = |r_s| e^{i\delta_{rs}} \tag{2.31b}$$

where the amplitudes and phases have been separated. Ellipsometry measures the state of polarization of the reflected beam compared to that of the incident beam. The convention is to express the measured quantity, ρ, as the *ratio* of the Fresnel reflection coefficients of the *p* and *s* components of the reflected beam:

$$\rho = \frac{r_p}{r_s} \tag{2.32}$$

However, it is convenient to express equation 2.32 in terms of the quantities Ψ and Δ defined above:

$$\rho = \tan \Psi \, e^{i\Delta} \tag{2.33}$$

where $\tan \Psi = \frac{|r_p|}{|r_s|}$ and $\Delta = \delta_{rp} - \delta_{rs}$. Thus, Ψ and Δ determine the differential changes in the amplitude and the phase of the incident wave upon reflection. Equation 2.33 is referred to as simply the Ellipsometry Equation.

In this work, ellipsometry was used to measure the index of refraction of the VDF oligomer film. Substituting equations 2.29a and 2.29b into equation 2.32 and rearranging, yields:

$$n_1 = n_0 \sin\varphi_0 \left[1 + \left(\frac{1-\rho}{1+\rho}\right)^2 \tan^2\varphi_0\right]^{1/2} \tag{2.34}$$

which expresses the index of refraction of the sample in terms of known (n_0 and φ_0) and measured (ρ) quantities. For thin film systems, there are multiple interfaces each with their own Fresnel reflection coefficients, and so the derivation of equation 2.33 becomes vastly more complicated, as the beam reaching the detector is made of the initially reflected beam and an infinite series of beams which are reflected from the substrate then transmitted out of the thin film [42]. Reference 42 provides the derivation of ρ for a single thin film and a substrate (two interfaces). Reflections from multiple interfaces cause phase shifts in the reflected beam (analogous to the discussion on XRD in section 2.6). The phase shift information is carried in Δ, from which the thickness of the film can be extracted [42-44].

Ellipsometry can be used to measure many different sample properties, as mentioned above. Another advantage of ellipsometry is that it is a non-contact technique, which is important for measuring soft organic materials such as the VDF oligomer studied in this work. Perhaps the most significant disadvantage of ellipsometry, however, is the rather sophisticated fitting routines and software needed to extract Ψ and Δ from the measured data.

The ellipsometer used to carry out the measurements in this work was a J. A. Woollam M-2000 DI Spectroscopic Rotating Compensator Ellipsometer. The spectral range was 300-1700 nm. CompleteEASE software, available from the J.A. Woollam Co., was used to fit and analyze the data and extract information about the samples.

2.12 Differential Scanning Calorimetry

Differential scanning calorimetry (DSC) measures the heat flow to a sample during heating, making this technique well suited for detecting phase changes of a sample as a function of temperature. In a typical DSC measurement, computer controlled heaters supply heat to both a sample and a reference material (usually some inert material such as alumina), as shown in figure 2.16 below [46].

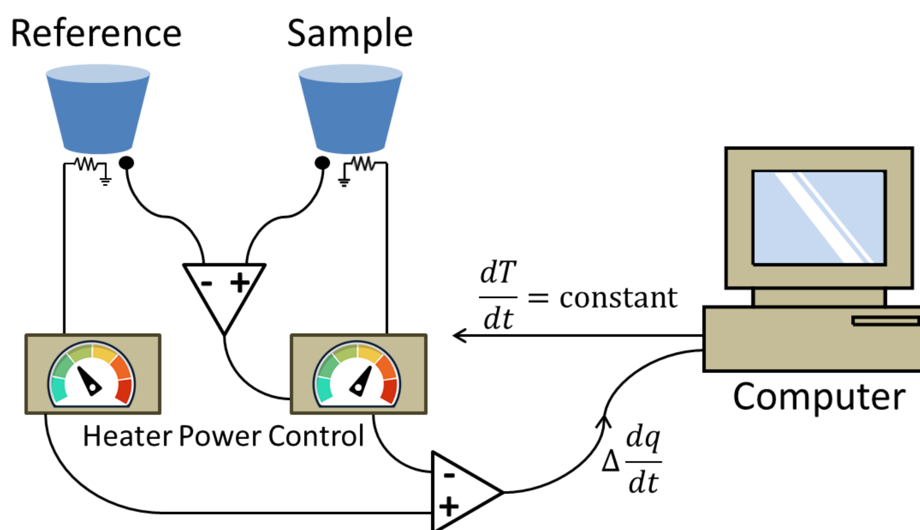

Figure 2.16: Schematic of a typical DSC setup. The temperatures of both a sample and reference pan are raised simultaneously at the same rate, as the sample undergoes phase transitions, the requisite power supplied to the

heat source needed to keep the rate of change in temperature constant changes. This change in supplied power is related to the heat adsorbed/released by the sample during a phase transition.

The temperatures of the sample and reference material are raised simultaneously at a constant rate. If the sample undergoes an endothermic phase transition, for example, it will need to absorb more heat in order to keep the rate of temperature increase constant, requiring an increase in power output of the sample heater. The difference in supplied power gives the difference in heat flow [47]:

$$\Delta P = \frac{\Delta Q}{\Delta t} \tag{2.35}$$

As mentioned above, during an endothermic process such as a phase transition, the sample will absorb more heat, and so the difference in heat flow between the sample and the reference, $(dQ/dt)_s - (dQ/dt)_r$, will be positive. Alternatively, if the sample undergoes an exothermic reaction, such as recrystallization (upon cooling), the sample will absorb less heat and the difference in heat flow will be exothermic. Figure 2.17 illustrates these differences in heat flow and shows ideal DSC data.

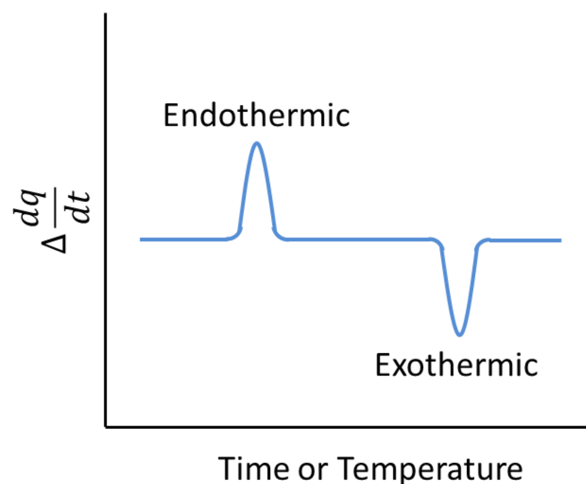

Figure 2.17: Illustration of hypothetical DSC data demonstrating a sample undergoing endothermic and exothermic reactions. In this case, the difference in heat flow is defined as sample minus reference.

In this work, DSC was used to find the temperatures of the ferroelectric phase transitions of bulk VDF oligomer. When the ferroelectric is cooled (heated) through the transition temperature and enters the ordered (disordered) phase, there is a release (absorption) of latent heat which, as described above, is manifested as peaks in heat flow vs. time/temperature curve.

A NETZSCH Model 204 F1 Phoenix Calorimeter was used to perform the DSC measurements in this work. The sample and reference pans were both alumina, with the sample pan loaded with about 10 mg of VDF oligomer powder. The DSC chamber was purged with Ar prior to each measurement. The heating/cooling rate was 2 °C/minute.

2.13 References

1. G. K. Wehner and G. S. Anderson, *Handbook of Thin Film Technology*, edited by L. I. Maissel and R. Glang (McGraw-Hill, New York, 1970), pg. 3-1
2. J. Vossen and W. Kerr, *Thin Film Processes* (Academic Press, New York, 1978), pg. 11
3. AJA International Inc., Sputtering Tutorial, http://www.ajaint.com/what-is-sputtering.html
4. Kurt J. Lesker Co., Ramp Procedure for Ceramic Target Conditioning, http://www.lesker.com/newweb/deposition_materials/rampprocedure_ceramictarget_materials.cfm?pgid=0
5. Inficon XTM/2 Deposition Monitor Operating Manual, http://products.inficon.com/GetAttachment.axd?attaName=b9bd8067-fbd1-43da-9ba9-1a016d559b04
6. R. Glang, *Handbook of Thin Film Technology*, edited by L. I. Maissel and R. Glang (McGraw-Hill, New York, 1970), pg. 1-40
7. AJA International Inc., Thermal Evaporation Tutorial, http://www.ajaint.com/what-is-thermal-evaporation.html
8. M. Bai and S. Ducharme, Appl. Phys. Lett. **85**, 3528 (2004)
9. G. Binnig, C. F. Quate, and C. Gerber, Phys. Rev. Lett. **56**, 930 (1986)
10. G. Meyer and N. M. Amer, Appl. Phys. Lett. **53**, 1045 (1988)
11. Nebraska Center for Materials and Nanoscience (NCMN) Surface and Materials Characterization Facility, http://ncmn.unl.edu/smcf/dimension-3100-spm
12. P. Güthner and K. Dransfeld, Appl. Phys. Lett. **61**, 1137 (1992)

13. E. Soergel, J. Phys. D: Appl. Phys. **44**, 464003 (2011)

14. W. G. Cady, *Piezoelectricity: An Introduction to Theory and Applications of Electromechanical Phenomenon in Crystals* (Dover Publications, New York, 1964), pg. 256

15. A. F. Devonshire, Philos. Mag. **42**, 1065 (1951)

16. Nebraska Center for Materials and Nanoscience (NCMN) Surface and Materials Characterization Facility, http://ncmn.unl.edu/smcf/bruker-icon-spm

17. N. W. Ashcroft and N. D. Mermin, *Solid State Physics* (Holt, Rinehart and Winston, New York, 1976), pg. 96

18. B. D. Cullity and S. R. Stock, *Elements of X-ray Diffraction: Third Edition*, (Prentice Hall, New Jersey, 2001), pg. 90

19. International Center for Diffraction Data, http://www.icdd.com/

20. P. Scherrer, Gött. Nachr. **2**, 98 (1918)

21. Nebraska Center for Materials and Nanoscience (NCMN) X-ray Structural Characterization Facility, http://ncmn.unl.edu/xray/rigaku

22. Available at http://users.uoi.gr/nkourkou/powdll/

23. J. Kerr, Philos. Mag. **3**, 321 (1877)

24. Z. Q. Qiu and S. D. Bader, Rev. Sci. Instrum. **71**, 1243 (2000)

25. T. C. Oakberg, Hinds Instruments PEM Application Note, available at http://www.hindsinstruments.com/wp-content/uploads/Magneto-Optic-Kerr-Effect.pdf

26. PEM-90 Photoelastic Modulator Systems User Manual, Hinds Instruments, Inc., 1998, pg. 6-1 Theory of Operation

27. S. Polisetty, J. Scheffler, S. Sahoo, Y. Wang, T. Mukherjee, X. He, and C. Binek, Rev. Sci. Instrum. **79**, 055107 (2008)

28. A. Berger and H. Hopster, Phys. Rev. Lett. **76**, 519 (1996)

29. R. W. Whatmore, Rep. Prog. Phys. **49**, 1335 (1986)

30. S. B. Lang, Physics Today, **58**, 31 (2005)

31. A. Cuadras, M. Gasulla, and V. Ferrari, Sensor. Actuat. A: Phys. **158**, 132 (2010)

32. A. V. Bune, C. Zhu, S. Ducharme, L. M. Blinov, V. M. Fridkin, S. P. Palto, N. G. Petukhova, and S. G. Yudin, J. Appl. Phys. **85**, 7869 (1999)

33. M. E. Lines and A. M. Glass, *Principles and Applications of Ferroelectrics and Related Materials* (Oxford University Press, Oxford, 1977)

34. A. G. Chynoweth, J. Appl. Phys. **27**, 78 (1956)

35. J. A. Cólon Santana, *Quantitative Core Level Photoelectron Spectroscopy: A Primer* (IOP Concise Physics, Morgan & Claypool, San Rafael, CA, 2015)

36. D. E. Jesson and S. J. Pennycook, Proc. R. Soc. Lond. A, **449**, 273 (1995)

37. J. Goldstein, D. Newbury, D. Joy, C. Lyman, P. Echlin, E. Lifshin, L. Sawyer, and J. Michael, *Scanning Electron Microscopy and X-ray Microanalysis: Third Edition* (Springer Science, New York, 2003), pg. 297

38. Nebraska Center for Materials and Nanoscience (NCMN) Electron Nanoscopy Instrumentation Facility, http://ncmn.unl.edu/enif/fei-tecnai-osiris-stem

39. J. A. Woollam, B. Johs, C. M. Herzinger, J. Hilfiker, R. Synowicki, and C. L. Bungay, Proc. SPIE **3**, CR27 (1999)

40. J. A. Woollam, B. Johs, C. M. Herzinger, J. Hilfiker, R. Synowicki, and C. L. Bungay, Proc. SPIE **29**, CR27 (1999)

41. J. A. Woollam, Co., *Ellipsometry Tutorial*, available at https://www.jawoollam.com/resources/ellipsometry-tutorial/what-is-ellipsometry

42. H. G. Tompkins and W. A. McGahan, *Spectroscopic Ellipsometry and Reflectometry* (John Wiley & Sons, New York, 1999), pg. 20

43. R. M. A. Azzam and N. M. Bashara, *Ellipsometry and Polarized Light* (North-Holland Publishing, New York, 1977), pg. 283

44. H. G. Tompkins and E. A. Irene, *Handbook of Ellipsometry* (William Andrew Publishing, New York, 2005), pg. 73

45. J. D. Jackson, *Classical Electrodynamics: Third Edition* (John Wiley & Sons, New York, 1999), pg. 305

46. G. W. H. Höhne, W. F. Hemminger, H.-J. Flammersheim, *Differential Scanning Calorimetry, Second Edition* (Springer Science, New York, 2003)

47. *Investigation of Polymers with Differential Scanning Calorimetry*, Humboldt Universität zu Berlin, available at http://polymerscience.physik.hu-berlin.de/docs/manuals/DSC.pdf

CHAPTER 3

ORGANIC FERROELECTRIC EVAPORATOR WITH SUBSTRATE COOLING AND *IN SITU* TRANSPORT CAPABILITIES

This chapter is based on the published paper: *Organic Ferroelectric Evaporator with Substrate Cooling and in situ Transport Capabilities*, K. Foreman, C. Labedz, M. Shearer, and S. Adenwalla, Rev. Sci. Instrum. **85**, 043902 (2014). Reprinted with the permission of AIP Publishing.

3.1 Introduction

The ability to fabricate heterostructured thin films of organic/non-organic layers is essential for both the understanding of fundamental physical phenomena at the interface between the layers and the development of devices. An example of a fundamental interfacial phenomenon that occurs at organic/inorganic interfaces (and the driving force behind the evaporator described in this chapter) is the magnetoelectric coupling between an organic ferroelectric thin film and a metallic ferromagnet which results in a pronounced effect on the magnetic anisotropy of the ferromagnetic film [1]. The low stiffness coefficient [1] of the polymer ensures there is little to no strain coupling between these two layers, thus enabling the investigation of the effect of electric fields on magnetism in the absence of strain coupling. Magnetic tunnel junctions [2, 3] (MTJs) and ferroelectric tunnel junctions [4] (FTJs) that utilize organic tunnel barriers have displayed distinctive behavior that is tied to the properties of the organic barrier. Devices based on organic thin films include high efficiency solar cells [5-7], field-effect transistors (FETs)

[8], flexible organic light-emitting diodes (OLEDs) [9], antireflection coatings [10], and even magnetic field sensors [11], all of which require conducting electrodes in intimate contact with organic thin films. In all cases, a clean, well-characterized interface between the organic thin film and the adjoining layer(s) is desirable, necessitating *in situ* vacuum deposition processes for the entire heterostructure. Although other organic thin film deposition techniques, such as spin coating and Langmuir-Blodgett deposition, produce excellent thin films that are crystalline, defect free, and fully functional [4, 12], these techniques are not compatible with metal deposition and are detrimental to the formation of a clean interface between the organic thin film and adjacent metallic layers.

Developing a deposition system capable of making a heterostructured organic/inorganic device, such as an MTJ, can be quite difficult for several reasons. First, it is unlikely that a single deposition technique can be used for both the inorganic and the organic thin films, requiring the deposition system to be capable of effusion (for the organic) and another technique for metallic layers (e.g. sputtering). Additionally, many organic materials have more than one crystalline phase. The oligomer vinylidene difluoride (VDF), for example, has several crystalline phases, only one of which is ferroelectric. Successful thin film growth of this crystalline form necessitates low substrate temperatures during deposition [13, 14]; hence the second requirement for many organic deposition systems is the ability to control the substrate temperature during deposition. Lastly, in order to prevent contamination, separate, connected chambers are necessary for the deposition of the organic layer and the inorganic layer(s). Therefore, a heterostructured sample deposition system must be capable of *in situ* sample transport. While sample transport from one chamber to another is easily accommodated by a

transfer arm and a gate valve, a deposition system capable of sample transport *and* substrate cooling can be quite difficult to construct.

This chapter describes the design, construction, and performance of an organic thin film evaporator that can be easily integrated into an existing deposition system (in this case a dc/rf magnetron sputtering/e-beam evaporation system) and also meets all of the above requirements. Given that these design constraints must be accounted for concurrently, it is clear that other homemade organic evaporators [15-17] or commercial systems, such as a self-contained Knudsen Effusion Cell [18, 19], will not meet the needs of many researchers. The deposition system presented here is capable of evaporating up to four distinct materials onto a substrate and, more importantly, is capable of both substrate cooling to temperatures below 130 K and *in situ* sample transport.

3.2 Design and Construction

The design of the evaporation chamber was dictated by an existing commercial AJA International, Inc. ATC-2000 [20] four gun sputtering/e-beam evaporation system used for metal deposition, which is briefly described below. The cylindrical sputtering/e-beam chamber (shown in figure 3.1) is connected to a load lock chamber and a sample transfer arm (Transfer Arm 1). The load lock chamber contains a substrate cassette elevator with a six cassette capacity. Substrates and masks are attached to a ring/disc system of cassettes (3.75 inch diameter discs, 0.0625 inch thick, set within a stainless steel ring) which can be loaded into the substrate cassette elevator in the load lock. A mask changer in the load lock enables the deposition of multiple layers with different mask patterns without breaking vacuum. A cassette carrier on the end of Transfer Arm 1

is able to transfer the substrate cassettes into and out of the sputtering/e-beam chamber's cassette holder. The cassette holder and transfer arm of the organic deposition chamber (Transfer Arm 2) are designed to be compatible with this system.

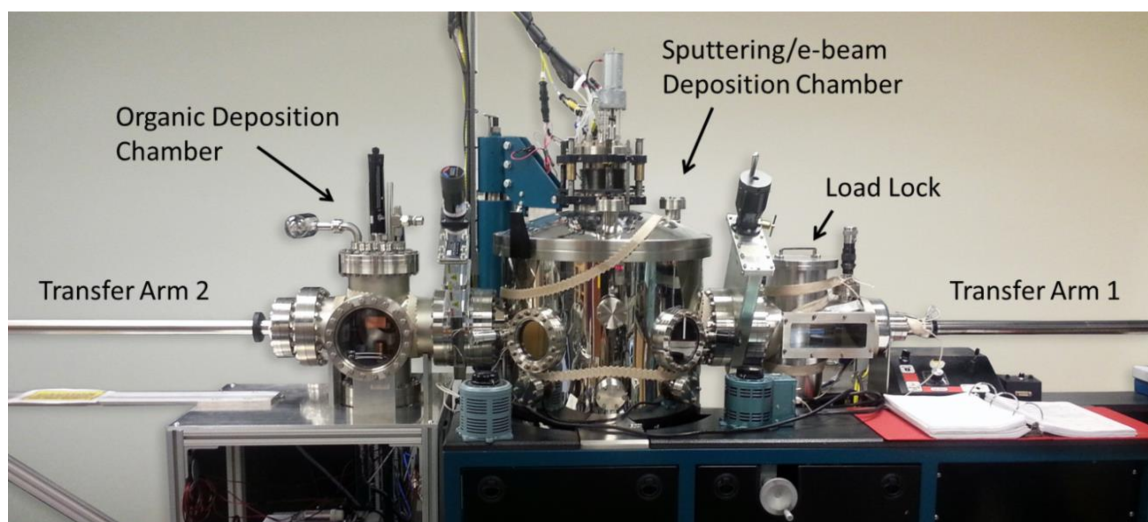

Figure 3.1: Photograph of the organic evaporator (left)/sputtering and e-beam chamber (middle)/load lock (right) system. Gate valves separate each of the three chambers. The organic evaporation chamber and Transfer Arm 2 were connected to an existing eight inch port on the sputtering/e-beam deposition system.

The main body of the organic deposition chamber consists of a six-way cross with standard eight inch ConFlat (CF) flange ports, as shown in figure 3.1 and illustrated in figure 3.2. Defining the glass window as the front, the sputtering/e-beam chamber is connected to the right port via an eight inch gate valve [21], Transfer Arm 2 is connected to the left, a quartz crystal deposition monitor and the vacuum pumps are mounted on the

back, the effusion cell is connected to the bottom, and finally the sample mount and cooling system are connected to the top port.

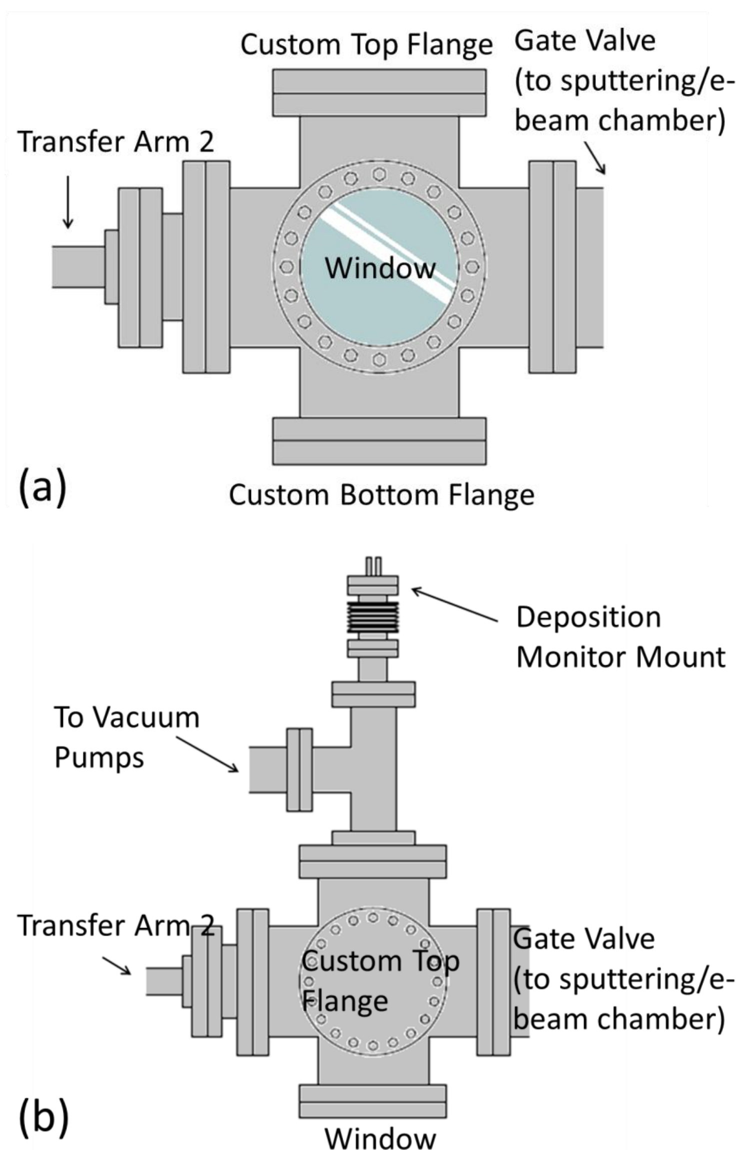

Figure 3.2: External side view (a) and top view (b) of the organic thin film deposition chamber. The customized flanges attached to the top and bottom of the chamber are described below.

The manually controlled gate valve separating the organic thin film deposition chamber from the sputtering/e-beam chamber prevents cross-contamination during the deposition process. The 36 inch long Transfer Arm 2 is connected to the organic deposition chamber via an eight to six inch reducer flange and moves cassettes between the sputtering/e-beam chamber and the organic deposition chamber. The four inch bore of this reducer flange allows for the end of the transfer arm to be fully retracted out of the six-way cross. The 4.5 inch T flange mounted on the back of the cross serves as the connection for both the vacuum pumps and the quartz crystal deposition monitor. The deposition monitor is mounted on a horizontal bellows with 100 mm of travel, allowing the deposition monitor to be fully retracted during sample deposition.

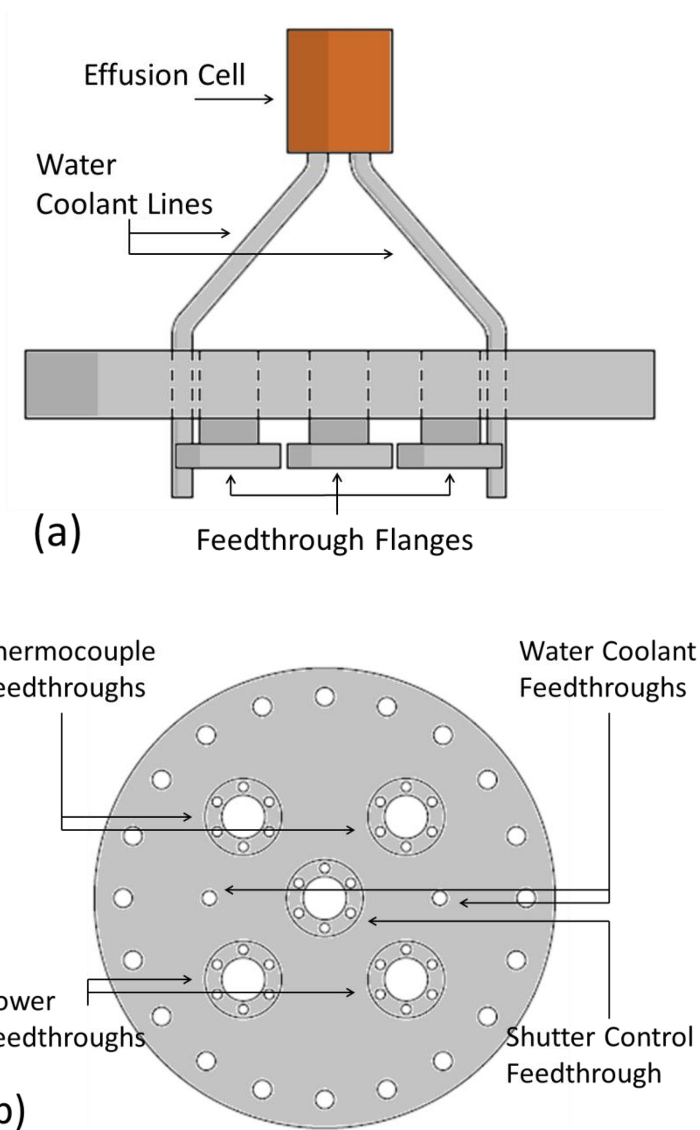

Figure 3.3: Side view (a) and bottom view (b) of the custom eight inch flange mounted on the bottom of the six-way cross.

The customized flange mounted on the bottom of the cross, shown in figure 3.3, contains the effusion cells (figure 3.4), which are based on a commonly used Knudsen Cell design [18, 19, 22, 23]. Five 1.33 inch half-nipple flanges were welded to holes bored out of a standard eight inch blank CF flange. Two of these half-nipple flanges serve

as ports for power feedthroughs to provide current to filaments in the effusion cells and two serve as ports for thermocouple feedthroughs to monitor effusion cell temperature. The fifth 1.33 inch half-nipple in the center of the eight inch custom flange serves as a port for a rotary motion actuator [24] that controls a three-quarter circle shaped shutter (visible in the inset of figure 3.6b) above the effusion cells that selects a single cell for deposition. Stainless steel tubing, 0.25 inch in diameter, was welded into two additional smaller holes to serve as both structural support and water coolant lines for the effusion cells. Because the effusion cells are so close together, it is necessary to cool the platform on which the cells are mounted (labeled in figure 3.4) in order to prevent heat transfer between cells and the consequent evaporation of material from other cells. A four-way sheet metal cross between the effusion cells further limits cross-contamination.

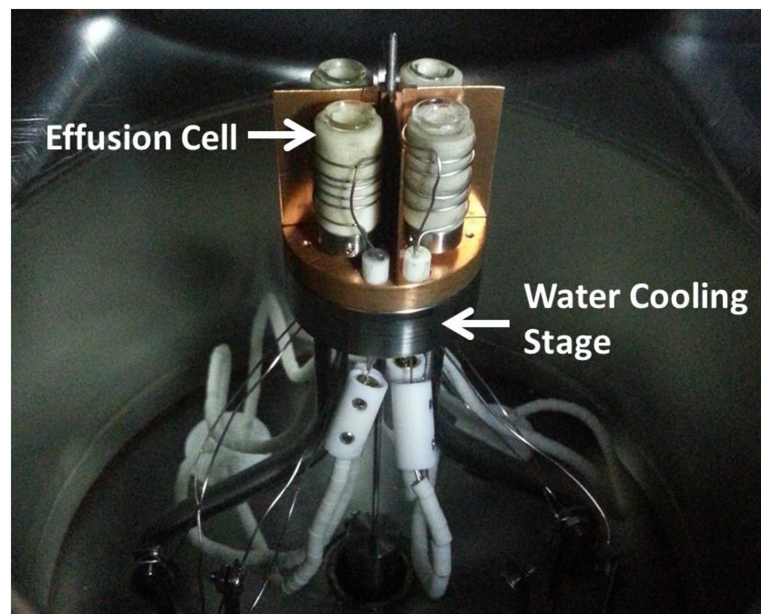

Figure 3.4: Photograph of the effusion cells atop the water cooled mount. The effusion cell housing is removed in the photograph.

The top flange consists of a standard, blank eight inch CF flange with seven holes bored into it (as shown in figure 3.5). 1.33 inch half-nipple flanges were welded into five of these holes. Two of these half-nipples were closed off with blank 1.33 inch flanges for use during future experiments, another leads to an ion gauge [25], and a fourth to a nitrogen gas line used to vent the chamber. A linear motion actuator [26] is connected to the central half-nipple flange and is attached to the cassette holder (shown in figure 3.6). Two open-ended 0.75 inch diameter stainless steel tubes are welded into the last two holes. The ends of the tubes that extend into the volume of the deposition chamber are welded to a 100 cm^3 rectangular stainless steel liquid nitrogen reservoir with an oxygen-free, high thermal conductivity (OFHC) copper bottom that is silver brazed to the stainless steel reservoir, forming a leak-free seal. The reservoir and tubes are open to the atmosphere and sealed off from the chamber vacuum. The reservoir itself is within the volume of the six-way cross to minimize the distance between it and the substrate, since it is the liquid nitrogen within the reservoir that cools the substrate.

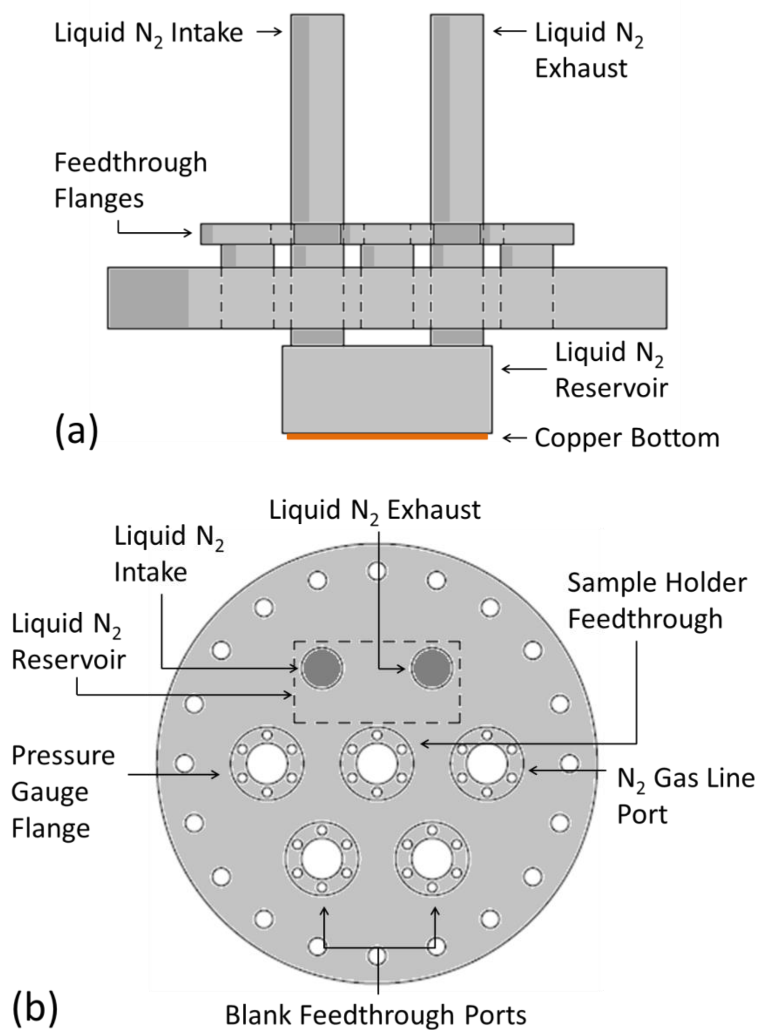

Figure 3.5: Side view (a) and top view (b) of the custom eight inch flange mounted on the top of the six-way cross.

The organic deposition system's cassette holding stage and transfer arm have been made to match the specifications of the cassette transfer system of the sputtering/e-beam deposition system. The cassette holder, made of OFHC copper to maximize thermal conduction, is attached to the end of the linear motion actuator as shown in figure 3.6. The linear motion actuator allows for the height of the cassette holder to be adjusted as

needed, allowing for the cassette to be placed onto and removed from the transfer arm, and also allowing for the distance between the sample and effusion cells to be changed *in situ*, controlling the deposition rate and the uniformity of the deposited film. As shown in figure 3.6, the copper bottom of the liquid nitrogen reservoir is connected to the cassette holder via eight sheets of OFHC copper, each 0.004 inch thick, three inches wide, and nine inches long. The sheets are attached to the OFHC copper bottom of the liquid nitrogen reservoir and the top of the cassette sample holder along their width. The thermal conductivity of these copper sheets at liquid nitrogen temperatures is approximately 580 W/m·K [27]. Many deposition systems that require substrate cooling rely on a rigid cold finger [28, 29] which does not allow for *in situ* motion, unlike the copper sheets, which are flexible enough to allow for vertical motion of the sample holder.

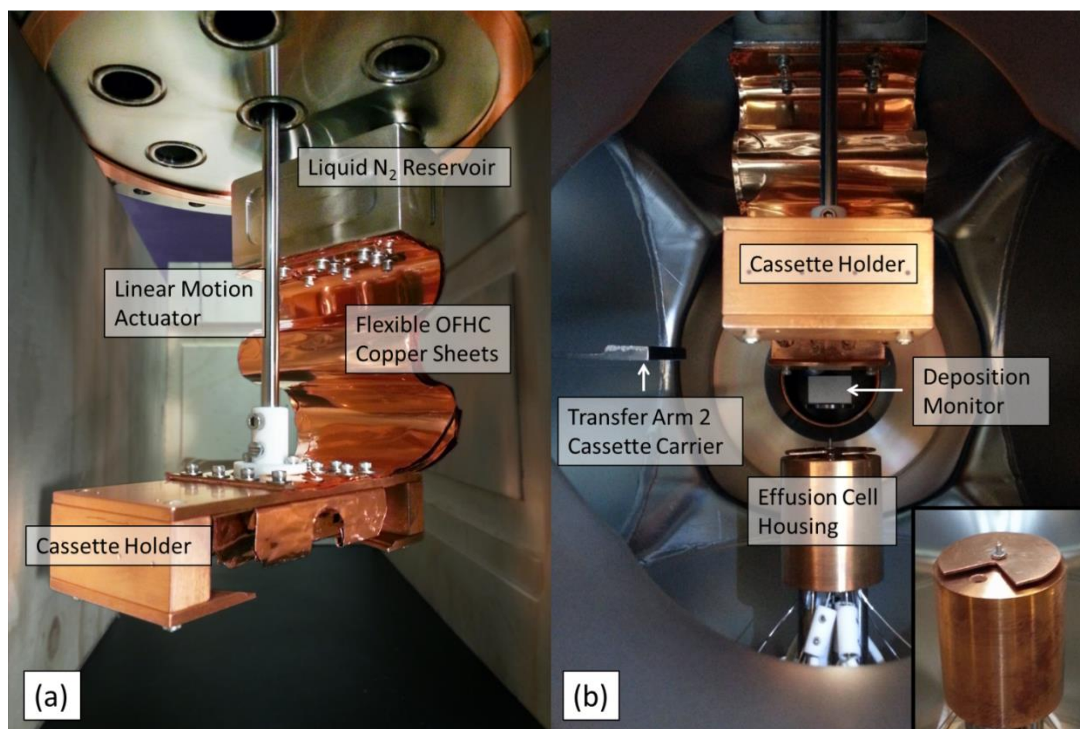

Figure 3.6: (a) Photograph of the substrate cooling system. OFHC copper sheets allow for vertical motion of the cassette holder while providing a thermal link between the liquid nitrogen reservoir and the cassette holder. (b) Photograph of the assembled organic deposition system as viewed through the front window, showing the need for vertical motion. The transfer arm (just visible on the left) brings a cassette into the chamber while the linear motion actuator allows the sample to be lifted off the transfer arm and put into position above the effusion cells. Also visible in this picture is the deposition monitor in its fully retracted position (center). The inset of (b) provides a view of the shutter above the effusion cell housing.

As discussed above, samples are loaded onto cassettes and transferred from the sputtering/e-beam system to the organic deposition system via Transfer Arm 2 (see figure 3.1). These cassettes (described above) are OFHC copper discs mounted on stainless steel rings. This disc/ring configuration is essential to the *in situ* mask exchange process performed in the load lock, and therefore the design of these cassettes cannot be changed. Because the only thermal contact with the copper disc is via the lip of the stainless steel ring, which in turn sits on the lip of the copper cassette holder, additional thermal contact is provided by the arrangement shown in figure 3.7a, which consists of four sets of hangers constructed from 0.007 inch thick beryllium copper (BeCu) foil cut to resemble a comb. These hangers, fastened onto the cassette holder, are stiff enough to maintain contact to the cassette disc, but flexible enough to be pushed upwards by the motion of the transfer arm when a cassette is being removed or inserted into the cassette holder. Four sheets of OFHC copper foil are attached under the BeCu hangers. These copper foils wrap around the BeCu hangers and extend over the width of the cassette holder (three inches) to maximize the thermal conduction area. The combination of the stiff BeCu comb-like hangers and the more flexible OFHC copper allows for both good thermal contact as well as the ability to move substrates in and out of the chamber. Figure 3.7b shows how this hanger system works during cassette loading, and figure 3.7c shows a cassette in position for a deposition in the cassette holder (during an actual deposition, a substrate would be affixed to this cassette). To remove the cassette from the cassette holder after the deposition, the linear motion actuator lowers the cassette onto Transfer Arm 2. The cassette is then removed from the cassette holder by moving the transfer arm to the left (refer to figure 3.7b), ensuring that the hangers bend in the same direction for

both cassette loading and unloading. This customized top flange, along with the sample cooling system discussed above, allows for both sufficient substrate cooling and *in situ* detachment from the cooling stage.

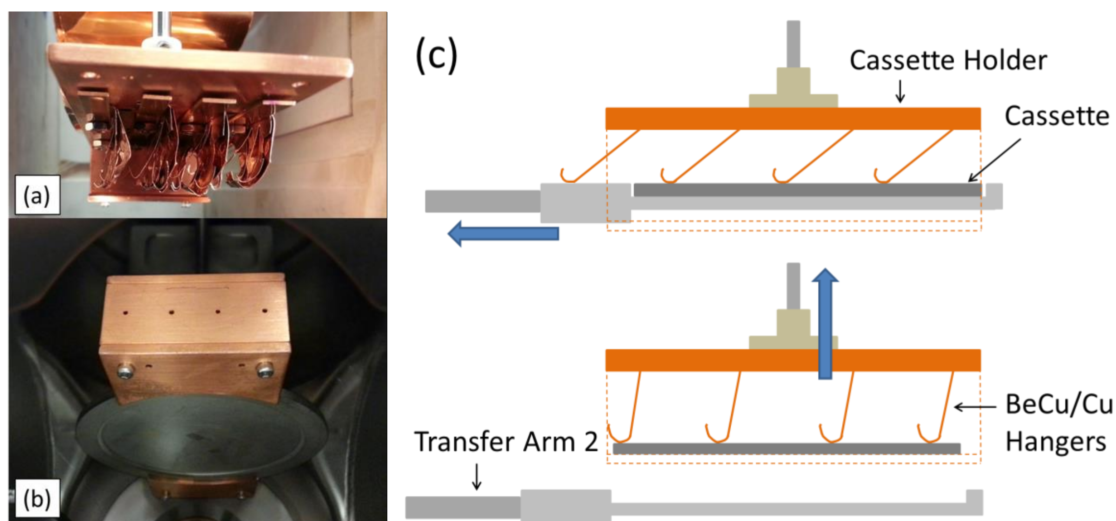

Figure 3.7: (a) Photograph of the partially disassembled cassette holder showing the BeCu/Cu hangers. (b) A cassette in position within the cassette holder (as viewed from below). (c) Simple diagram showing the how the hangers perform during cassette loading. As the transfer arm moves the cassette into position, the hangers bend out of the way (top). When the cassette is in position relative to the cassette holder, the cassette holder is moved upwards via the linear motion actuator and lifts the cassette off of the transfer arm. As the cassette is being lifted, the hangers relax back to their natural position so that they are always in contact with the cassette itself (bottom). This configuration allows for samples to be moved in situ, and remain in good thermal contact with the cassette holder during deposition.

3.3 Operation and Performance

The substrate cooling performance of this system was repeatedly measured using a Si thermocouple wafer loaded on a cassette in the substrate position. Liquid nitrogen is transferred to the reservoir from a standard 230 L liquid nitrogen dewar under a pressure of 22 psi via insulated copper tubing. The flow is adjusted so that the reservoir stays full with little overflow. Reproducible cooling curves are shown in figure 3.8. A substrate temperature of 132 K is achieved after 100 minutes of cooling, with an ultimate temperature of 128 K after another 55 minutes (black line). The temperature stability is approximately one degree over a period of 35 minutes, more than enough time for a typical thin film deposition. Clearly, these data show that the flexible BeCu/Cu hanger system provides sufficient thermal conductivity while still allowing for sample transport.

Several other hanger designs were tested before this BeCu/Cu hanger system. Previous iterations were either incapable of reaching the desired temperature of 130 K or incapable of reaching it in a timely fashion. The results of these previous configurations are also shown in figure 3.8 and described briefly below. The blue line corresponds to hangers made of uncut BeCu sheets. These uncut sheets of BeCu were too stiff to bend out of the way of the cassette during loading (figure 3.7b) and therefore not a viable option. The green line corresponds to hangers made of uncut sheets of Cu foil, which were not stiff enough to maintain sufficient contact with the cassette once in position. The pink line corresponds to a hanger system of cut (comb-like) BeCu wrapped in full sheets of Cu identical to the hanger system described in the previous section. However, in an attempt to minimize the strain on the linear motion actuator, there were only four sheets of Cu connecting the liquid nitrogen reservoir and the cassette holder during this

test. This last iteration of the cooling system could reach an ultimate temperature close to that of the final design, but took much longer to do so.

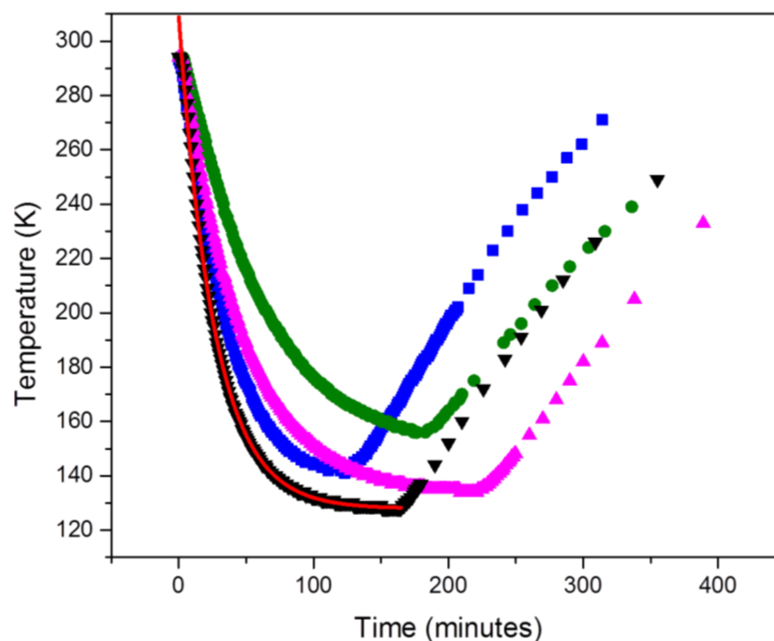

Figure 3.8: Substrate temperature versus time for both cooling and warming cycles. The black line corresponds to hanger design described in detail above (exponential fit in red). After about 160 minutes, the liquid nitrogen reservoir was allowed to empty and the sample warmed back up to room temperature in a linear fashion. Other hanger configurations were also tested, but were found to be inadequate. The blue, green and pink lines correspond to failed hanger designs also described above.

To perform a test deposition of the ferroelectric oligomer vinylidene difluoride (CF_3-$(CH_2CF_2)_n$-I, n = 15±2), the 100 μL volume crucibles in the effusion cells are loaded. Earlier work has shown that evaporation of this oligomer results in a ferroelectric

phase with polarization perpendicular to the plane of the substrate *only* under stringent growth conditions of low substrate temperatures and low deposition rates [13, 14]. A glass substrate is mounted on a cassette and inserted into the load lock, with a base pressure of 9×10^{-8} Torr. The cassette is then moved to the sputtering/e-beam chamber (with a base pressure of 1×10^{-8} Torr), where a bottom metallic layer (in this case Pt/Co) is deposited using the desired mask. The cassette, with the substrate and mask, can then be moved back to the load lock, where the mask used for the bottom electrodes may be changed or removed. Using a two stage process and both transfer arms, the cassette is moved into the organic deposition chamber, with a base pressure of 8×10^{-8} Torr, via the sputtering/e-beam chamber. Transfer Arm 2 moves the cassettes from the sputtering/e-beam chamber's cassette holder to the position in the organic deposition chamber shown in the upper portion of figure 3.7b. The linear motion actuator is then used to raise the cassette holder, lifting the cassette off the transfer arm. The transfer arm is then fully retracted in the evaporation chamber, and the reservoir is filled with liquid nitrogen. The effusion cell is heated using an applied current of about 0.45 A. Deposition rates were measured using the quartz crystal monitor. The deposition versus time curve shown in figure 3.9 indicates that the deposition rate is almost constant once the temperature of the crucible stabilizes at 57-58 °C, which occurs ~40 minutes after the application of current. For the deposition rate test shown in figure 3.9, the shutter on top of the effusion cell housing was left open the entire time.

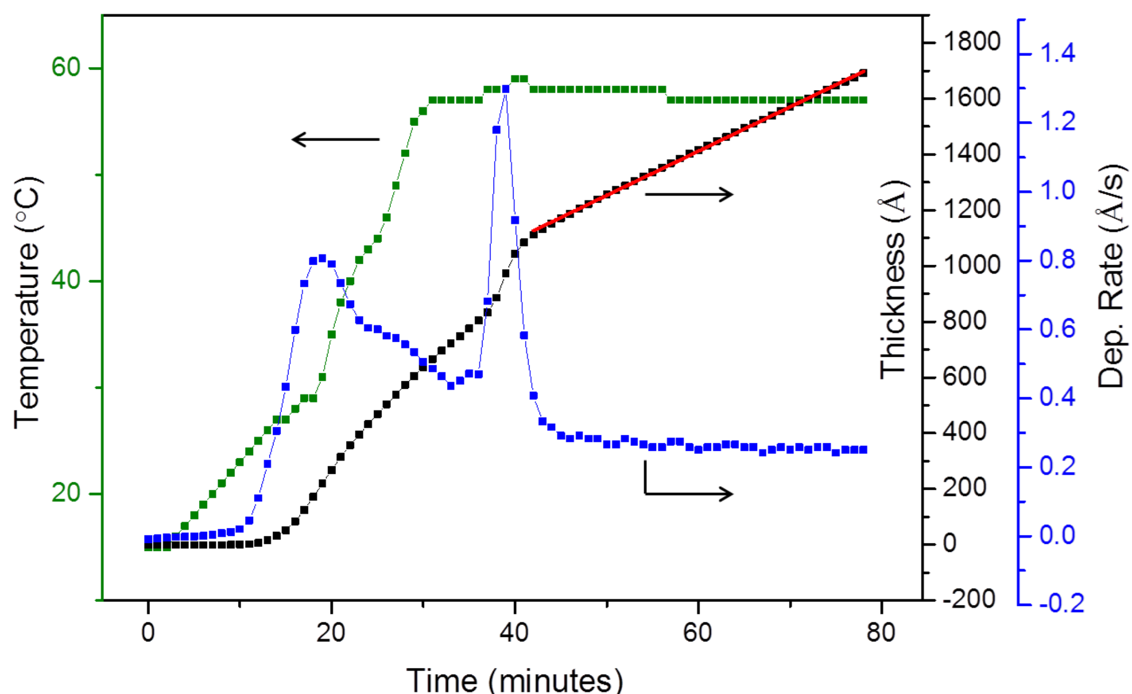

Figure 3.9: Deposition rate (blue), total thickness (black), and crucible temperature (green) as functions of time. Opening the shutter on the effusion cell at the appropriate time exposes the sample to only the linear portion of the thickness versus time curve (linear fit in red).

The test sample, created using the combined techniques of sputtering and organic thin film deposition, consisted of glass/Pt (50nm)/Co (1.5 nm)/VDF (200nm)/Al (20nm). The shutter over the effusion cell was opened 40 minutes into the application of a 0.45 A current to the effusion cell (at a point corresponding to the "start" label in figure 3.9) to ensure a uniform deposition rate of 0.25 Å/s. Using the Chynoweth Method [30], a pyroelectric hysteresis loop of the VDF oligomer was measured (figure 3.10). The pyroelectric current is directly proportional to the out-of-plane ferroelectric polarization

of the oligomer. This loop clearly demonstrates polarization switching behavior, a hallmark of ferroelectricity. Hence, a thin film of the ferroelectric crystalline phase of VDF oligomer with out-of-plane polarization has been successfully fabricated.

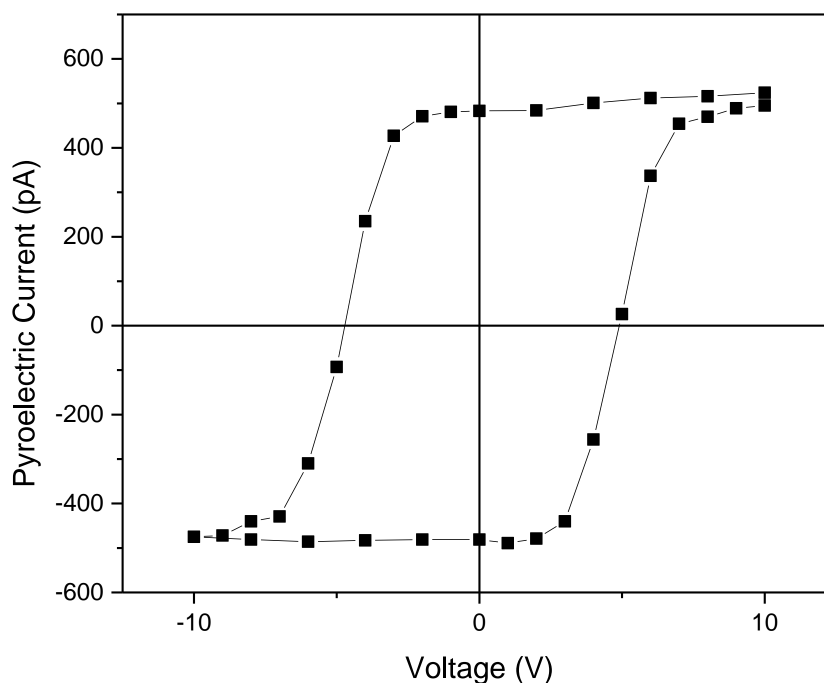

Figure 3.10: Pyroelectric hysteresis loop collected from a VDF oligomer thin film grown in the deposition system described here. This loop shows switching between the two ferroelectric polarization states and demonstrates that the chamber is capable of both stable deposition and substrate cooling, both of which are simultaneously necessary to obtain the ferroelectric crystalline phase with polarization pointing out-of-plane.

3.4 Conclusions

Described in this chapter is the design, construction, operation, and performance of an evaporative chamber capable of substrate cooling and *in situ* sample transfer

between deposition chambers. This design includes a quartz crystal deposition monitor for thickness calibration. The unique comb-like hanger system is capable of cooling the substrates to a temperature of 128 K, while still allowing samples to be moved without breaking vacuum. Although this system is connected to a commercial sputtering/e-beam deposition chamber, the design presented here could be easily adapted and used as a stand-alone system. The ability to adjust the vertical position of the sample, used to remove the cassettes from the transfer arm, is also useful for regulating the uniformity of the deposited film.

Depositing the VDF oligomer in its ferroelectric crystalline phase in direct contact with a metallic layer demands simultaneous control of a very specific set of deposition parameters. This chamber design successfully satisfies these demands, as evidenced by the characteristic ferroelectric hysteresis loop clearly indicating that the VDF oligomer thin film grows in its ferroelectric crystalline phase with polarization pointing out-of-plane, with a clean interface at the underlying metallic layer. This deposition system opens a new channel for the exploration of physical phenomena associated with organic thin film heterostructures.

3.5 Acknowledgements

Financial support is provided by the National Science Foundation (Grant No. ECCS-1101256) and by the NSF through the Nebraska Materials Research Science and Engineering Center (MRSEC) (DMR-0820521).

3.6 References

1. A. Mardana, S. Ducharme, and S. Adenwalla, Nano Lett. **11**, 3862 (2011)
2. J. M. Lopez-Encarnacion, J. D. Burton, E. Y. Tsymbal, and J .P. Velev, Nano Lett. **11**, 599 (2011)
3. J. P. Velev, J. M. Lopez-Encarnacion, J. D. Burton, and E. Y. Tsymbal, Phys. Rev. B **85**, 125103 (2012)
4. D. Y. Kusuma and P. S. Lee, Adv. Mater. **24**, 4163 (2012)
5. A. K. Ghosh and T. Feng, J. Appl. Phys. **44**, 2781 (1973)
6. A. K. Ghosh, D. L. Morel, T. Feng, R. F. Shaw, and C. A. Rowe, Jr., J. Appl. Phys. **45**, 230 (1974)
7. A. K. Ghosh and T. Feng, J. Appl. Phys. **49**, 12 (1978)
8. C. P. Jarrett, R. H. Friend, A. R. Brown, and D. M. de Leeuw, J. Appl. Phys. **77**, 6289 (1995)
9. S. W. Seo, H. Chae, S. J. Seo, H. K. Chung, and S. M. Cho, Appl. Phys. Lett. **102**, 161908 (2013)
10. D. Z. Garbuzov, S. R. Forrest, A. G. Tsekoun, P. E. Burrows, V. Bulovic, and M. E. Thompson, J. Appl. Phys. **80**, 4644 (1996)
11. A. Mardana, M. Bai, A. Baruth, S. Ducharme, and S. Adenwalla, Appl. Phys. Lett. **97**, 112904 (2010)
12. J. C. Tai, J. C. Huang, Y. M. Chang, K. S. Li, J. Y. Hong, S. S. Wong, W. C. Chiang, and M. T. Lin, Appl. Phys. Lett. **96**, 262502 (2010)
13. K. Noda, K. Ishida, T. Horiuchi, K. Matsushige, and A. Kubono, J. Appl. Phys. **86**, 3688 (1999)

14. A. Takeno, N. Okui, T. Kitoh, M. Muraoka, S. Umemoto, and T. Sakai, Thin Solid Films **202**, 205 (1991)

15. J. Yoshinobu, K. Mukai, and T. Katayama, Rev. Sci. Instrum. **79**, 076107 (2008)

16. M. T. Greiner, M. G. Helander, Z. B. Wang, and Z. H. Lu, Rev. Sci. Instrum. **80**, 125101 (2009)

17. R. Gutzler, W. M. Heckl, and M. Lackinger, Rev. Sci. Instrum. **81**, 015108 (2010)

18. High Temperature Knudsen Cell, Comstock Inc., Oak Ridge, TN, USA, see http://www.comstockinc.com/kcell.htm for product specifications

19. Molecular Effusion Source, Topac Inc., Cohasset, MA, USA, see http://www.topac.com/kcel.html for product specifications

20. dc Magnetron Sputtering/e-beam Deposition System, AJA International, Inc., North Scituate, MA, USA, see http://www.ajaint.com/systems_atc.htm for product specifications

21. Manual Bellows Sealed Gate Valve, Kurt J. Lesker Co., Jefferson Hills, PA, USA, see http://www.lesker.com/newweb/valves/Gate_KJLC_manual.cfm?pgid=cf for product specifications

22. ORMA Series Evaporators, Manits Deposition, Oxfordshire, United Kingdom, see http://www.mantisdeposition.com/uhv-components/view/product/info/orma-series.html for product specifications

23. 4x OMBE Source, Dodecon Nanotechnology, Waldenbuch, Germany, see http://dodecon.de/4xOMBE.html for product specifications

24. Rotary Motion Feedthrough, MDC Vacuum Products LLC, Hayward, CA, USA, see http://www.mdcvacuum.com/DisplayPart.aspx?d=MDC&p=670000 for product specifications

25. Ion Pressure Gauge, MDC Vacuum Products LLC, Hayward, CA, USA, see http://www.mdcvacuum.com/DisplayPart.aspx?d=MDC&p=432023 for product specifications

26. Linear Motion Feedthrough, MDC Vacuum Products LLC, Hayward, CA, USA, see http://www.mdcvacuum.com/DisplayPart.aspx?d=MDC&p=660008 for product specifications

27. E. D. Marquardt, J. P. Le, and R. Radebaugh, Cyrogenic Material Properties Database, NIST, Presented at the 11th International Cryocooler Conference (2000)

28. N. Weiss, U. Drechsler, M. Despont, and S. Parkin, Rev. Sci. Instrum. **79**, 123902 (2008)

29. S. A. FitzGerald, H. O. H. Churchill, P. M. Korngut, C. B. Simmons, and Y. E. Strangas, Rev. Sci. Instrum. **77**, 093110 (2006)

30. A. G. Chynoweth, J. Appl. Phys. **27**, 78 (1956)

CHAPTER 4

FERROELECTRIC CHARACTERIZATION AND GROWTH OPTIMIZATION OF THERMALLY EVAPORATED VINYLIDENE FLUORIDE THIN FILMS

This chapter is based on the published paper: *Ferroelectric Characterization and Growth Optimization of Thermally Evaporated Vinylidene Fluoride Thin Films*, K. Foreman, N. Hong, C. Labedz, M. Shearer, S. Ducharme, and S. Adenwalla, J. Phys. D: Appl. Phys. **49**, 015301 (2016). Reprinted with the permission of IOP Publishing.

4.1 Introduction

Organic thin films form an integral part of technologically important devices, including field-effect transistors [1], organic light emitting diodes [2], solar cells [3-5], antireflection coatings [6], and magnetic field sensors [7]. Organic thin films also offer advantages in the investigation of fundamental scientific phenomena, including spin transport [8] in magnetic tunnel junctions [9, 10] and ferroelectric tunnel junctions [11]. Organic ferroelectric thin films have proved useful in the investigation of electric-field control of magnetism, an effect that is of major interest [12-14], because of both the fundamental physics behind magnetoelectric effects and the technological implications of such control. The latter includes the advancement of spintronic devices, magnetic field sensors, and non-volatile magnetic memory storage devices. Electric-field control of magnetic properties has been observed in a wide variety of materials [15-20], with the mechanism highly dependent on the choice of materials. Magnetoelectric coupling in layered ferroelectric/ferromagnetic thin film heterostructures typically arises from

volumetric effects, coupling magnetic and electrical order via strain [21-23]. Other subtle interfacial effects, such as the spin dependent screening potential [24, 25] that arises from electric field penetration, can change the magnetic anisotropy and/or magnetization of the ferromagnetic layer, but are typically overshadowed by volumetric effects. Theoretical modeling of the magnetoelectric coupling between organic ferroelectric thin films of poly(vinylidene fluoride) (PVDF) and metallic ferromagnetic thin films predict large changes in the magnetic anisotropy of the ferromagnetic film [26], an effect that was clearly seen in experiments on heterostructures of the copolymer poly(vinylidene fluoride-trifluoroethylene) (P(VDF-TrFE) with a 70:30 ratio of VDF to TrFE) and a ferromagnetic Co thin film [15]. In these heterostructures, volumetric effects play a minor role at best because of the large mismatch in stiffness coefficients.

Ferroelectric VDF oligomer is particularly well suited for experiments on the electric-field control of magnetism because of its low stiffness coefficient (~100 times softer than a typical metal [15]) and its high remanent polarization of 0.13 C/m^2 [27] (as compared to 0.06 C/m^2 for PVDF [28]). The large surface charge density results in a large effective electric field at the ferroelectric/ferromagnetic interface and the low stiffness ensures that changes in magnetic behavior are due to the electric field and not to strain coupling, essentially minimizing the volumetric effects present in other ferroelectric/ferromagnetic systems. In addition, the shorter, well-defined chain lengths of the oligomer, as compared to the polymer PVDF, will lead to better crystallinity and easier nanoscale processing.

If VDF oligomer is to be used in a ferroelectric/ferromagnetic heterostructure, such as the magnetic tunnel junctions described in references 9 and 10, ferroelectric

tunnel junctions like those described in reference 11, or in other nanostructured devices, a clean, well-characterized contact between the organic layer and any adjacent layers is imperative. This requirement eliminates Langmuir-Blodgett deposition or solvent spin coating as possible deposition techniques since these processes expose the sample to the atmosphere during the deposition and compromise the cleanliness of the electrode/oligomer interface. An all-vacuum deposition of the heterostructure, in particular thermal evaporation of the VDF oligomer layer, will result in clean, abrupt, and well-defined interfaces. Unfortunately, thermal evaporation of VDF oligomer in the requisite ferroelectric β-phase and with the appropriate crystalline orientation can be difficult due to a demanding set of deposition parameters [29]. Previous reports on the growth of ferroelectric thin films of VDF oligomer by vacuum evaporation indicate a range of deposition rates and define the optimal substrate temperatures for growing films of the appropriate phase and orientation but provide few other insights on how to grow high quality films [27, 30-33]. Furthermore, although some physical and ferroelectric properties of VDF oligomer thin films, such as the remanent polarization [27], pyroelectric coefficient [31], and structure of epitaxially grown films [34, 35] have been reported, many other properties remain unreported. To that end, the objectives of this chapter are twofold: first, this chapter provides a comprehensive study of the thermal evaporation of VDF oligomer thin films that offers insight into parameter control for the successful growth of the films, and second, it reports on several properties of the resulting VDF oligomer thin films.

4.2 Sample Preparation and Experimental Techniques

VDF oligomer thin films can be categorized and differentiated by their chain conformations, with the most common forms being β-phase (form I), α-phase (form II), or γ-phase (form III) [36]. The conformations result in different crystallographic structures that can be identified by x-ray diffraction (XRD). Both α-phase and γ-phase crystals have no net polarization due to the antiparallel configuration of neighboring dipole moments, making their presence undesirable for most purposes. The all-trans conformation of the β-phase, shown in figure 4.1, results in a net dipole moment perpendicular to the molecular *c* axis along the (020) direction and is ferroelectric. The direction of the polarization is also important for device application. Any device using a stacked electrode structure similar to that shown in figure 4.1 requires at least some component of the polarization perpendicular to the plane of the electrodes. Noda et al. have studied the structure of VDF oligomer films as a function of substrate temperature during deposition in some detail [34, 35]. Using grazing-incidence XRD, Fourier-transform infrared spectroscopy, and atomic force microscopy (AFM), they found that the crystalline phase is highly dependent on substrate temperature, and grows epitaxially on substrates such as KCl (001). Ultimately, it was found that β-phase crystals dominate the thin film when deposited on any substrate, regardless of crystalline order, at low deposition temperatures close to 130 K. This insight informs the present work – all the thin films described here were deposited at a fixed substrate temperature of 128 K.

The thin films of VDF oligomer [CF_3-$(CH_2CF_2)_n$-I] (shown in figure 4.1) were deposited in a thermal evaporation chamber connected via a gate valve to a sputtering/e-beam evaporation chamber [29]. VDF oligomer powders from two separate

manufacturers, Kunshan Hisense Electronic Co., Ltd. and Daikin Industries, Ltd., were used with no apparent difference in film quality. The Kunshan Hisense oligomer had a chain length of $n = 15 \pm 2$, as measured by nuclear magnetic resonance spectroscopy, while the Daikin Industries oligomer has a chain length of $n = 14 \pm 1$, as measured by mass spectrometry. Metallic electrodes were deposited in the adjacent sputtering/e-beam chamber, allowing the samples to be made without removing them from vacuum, resulting in clean oligomer/metal interfaces. Most samples consist of glass (1 mm)/Pt (50 nm)/Co (1.2 nm)/VDF (t nm)/Al (20 nm), with t ranging from 50 nm to 2500 nm. Figure 4.1 shows a typical sample structure with the Pt/Co and Al electrodes enclosing a device area of 0.04 mm^2. Here, the Pt/Co layer merely serves as a metallic electrode; the ferromagnetic properties of the Co are not relevant because the work in this chapter is primarily focused on the optimal growth and characterization of the VDF oligomer. The base pressures of the sputtering/e-beam chamber and the organic thermal evaporation chamber were 1×10^{-8} Torr and 8×10^{-8} Torr respectively. The metallic electrodes were deposited at a rate of 0.2-0.5 Å/s, and the VDF oligomer was grown at deposition rates varying between 1.14 Å/s and 11.7 Å/s, as determined by spectroscopic ellipsometry measurements. The deposition rate of the VDF oligomer was controlled by varying the current through the filament in the evaporator's effusion cells [29], which were equipped with thermocouples to monitor the temperature of the VDF oligomer crucible during the deposition. The crucible temperature was shown to be an important parameter in obtaining switchable, ferroelectric films (discussed below). The VDF oligomer begins to evaporate, albeit at a low rate, at a crucible temperature of 30 °C [29]. Because optimizing the yield of switchable, ferroelectric films is of particular interest, a total of 87

VDF oligomer thin film samples, each with multiple metallic electrodes similar to that shown in figure 4.1, were made and measured. Multiple electrode areas on the same sample differed only in VDF oligomer film thickness (detailed in figure 4.6), allowing for control of all other variables. In addition to the samples on glass substrates, 22 VDF oligomer thin film samples were grown on polished Si wafers using the same deposition conditions as samples on glass substrates outlined above. These Si/VDF oligomer samples were used exclusively for XRD and spectroscopic ellipsometry measurements, the details of which are outlined below.

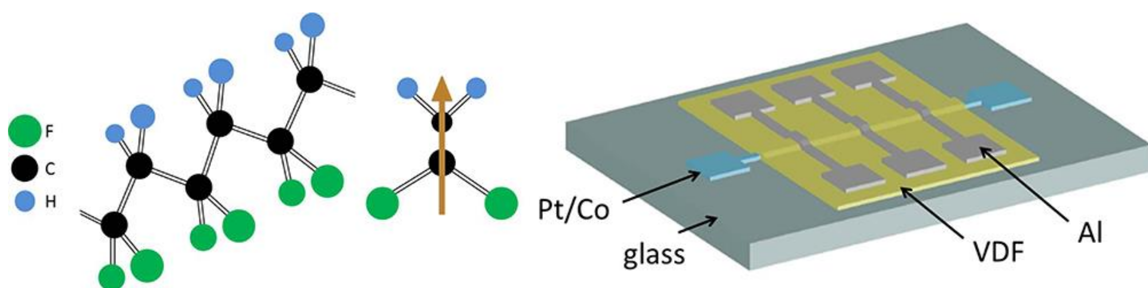

Figure 4.1: (Left) VDF oligomer structure. The β-phase chain conformation shown results in ferroelectric ordering. (Center) An electric dipole moment forms across the carbon chain, directed from the highly electronegative F atoms to the H atoms. (Right) Sample structure: glass (1 mm)/Pt (50 nm)/Co (1.2 nm)/VDF (t nm)/Al (20 nm). The Al and Pt/Co layers serve as top and bottom electrodes respectively.

XRD measurements on all 22 Si/VDF oligomer thin films samples were made in θ-2θ mode using a Rigaku D/Max-B Diffractometer with Co Kα radiation of wavelength 1.789 Å. AFM measurements were made on 27 of the thin film samples on glass substrates using a Digital Instruments Nanoscope IIIa Dimension 3100 SPM system in

tapping mode at a frequency of 138 kHz. Pyroelectric measurements were made on all 245 electrodes of the 87 thin film samples on glass substrates using the Chynoweth method [37] with a 1 mW, 658 nm wavelength diode laser modulated at 2 kHz. The film thickness and optical properties of 5 Si/VDF oligomer thin films samples were determined by ellipsometry measurements [38, 39] using a J.A. Woollam M-2000 DI spectroscopic rotating compensator ellipsometer. The dependence of the refractive index on wavelength was modeled by a Cauchy dispersion equation in the spectral range of 300 to 1700 nm using CompleteEASE® software available through the J.A. Woollam Company. Maps of film thickness and refractive index were recorded using spectroscopic ellipsometry with a beam diameter of 300 μm by measuring 81 points in a sample area measuring 1.5 cm by 1.5 cm.

4.3 Results and Discussion

Following the work of Noda et al. and Takeno et al. [40], the films discussed here were deposited on liquid-nitrogen-cooled substrates, at a temperature of 128 K, resulting in a large fraction of β-phase VDF oligomer. This crystallographic orientation is apparent from the XRD data, shown in figure 4.2, for the as-grown thin film. A two-peak fit to the data results in peaks at $2\theta = 23.1°$ and 23.8°, which correspond to the (110) peak of the α-phase and the (020) peak of the β-phase, respectively [41, 42]. Figure 4.2 shows that the as-grown VDF oligomer thin films are predominantly in the (020) β-phase, the optimal orientation for maximum out-of-plane polarization. Annealing results in a larger proportion of (110) β-phase, but does not result in a significant improvement in the crystallinity (discussed below). It should be noted that the longer wavelength radiation

from the Co Kα source used here (as compared to the more common Cu Kα radiation with wavelength 1.54 Å), allows for a clear separation between these closely spaced diffraction peaks. Hence, one can clearly distinguish between (110) and (020) β-phase peaks, whereas previous measurements could not [32], allowing for the definitive conclusion that the as-grown films are oriented along the (020) direction.

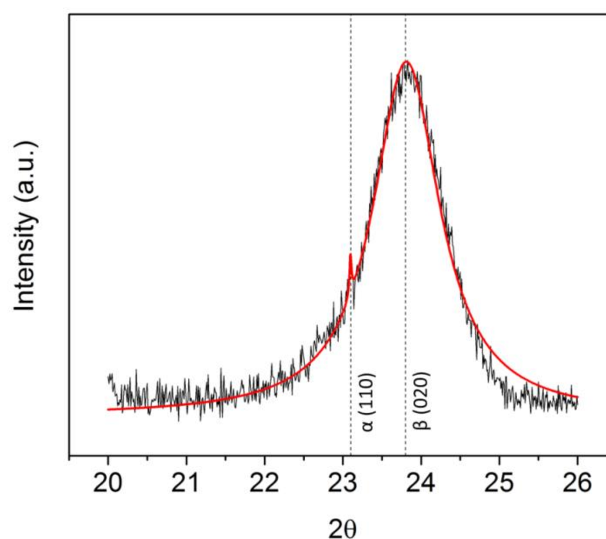

Figure 4.2: XRD data for the as-grown VDF oligomer thin film. No significant changes are observed in the XRD data as deposition parameters were varied, indicating that as long as the substrate is cooled during deposition, the as-grown film is predominantly in the (020) β-phase. A two-peak fit is shown in red.

XRD measurements were performed on samples grown under various sets of deposition parameters. Using the Scherrer equation:

$$\tau = {}^{k\,\lambda}/_{\beta\ \cos\theta} \tag{4.1}$$

where k is the shape factor, widely accepted as 0.9, λ is the wavelength of the radiation, β is the full width at half maximum value of the Bragg peak, and θ is the location of the Bragg peak, τ, the average particle size of the VDF oligomer thin films, can be calculated. Calculated Scherrer particle sizes of the majority (020) β-phase varied little, ranging from 10.1 nm to 12.2 nm, and show no correlation with deposition rate, crucible temperature, or film thickness.

Although all films showed diffraction peaks similar to that in figure 4.2 and possessed a measureable pyroelectric current, indicating the presence of β-phase VDF oligomer, it was found that merely keeping the substrate cooled during deposition is not sufficient for successful growth of ferroelectric, switchable VDF oligomer thin films. Successful VDF oligomer growth, defined by the ability to saturate the ferroelectric polarization and switch its direction, i.e., collect a complete pyroelectric hysteresis loop, was found to be highly dependent on the surface roughness of the thin film. The surface roughness is governed by the deposition rate, which in turn is controlled by the crucible temperature. Initial attempts, in which the crucible temperature was allowed to rise as high as 80 °C, resulted in a poor yield of less than 25%, though minor polarization hysteresis loops were often obtained. Although nearly every sample showed a strong pyroelectric current (even at low applied voltage) less than 25% of the samples could withstand a voltage large enough to saturate and/or switch the sample. In an effort to increase the yield of switchable, ferroelectric films, the surface roughness of the VDF

oligomer thin film is first investigated, with the data on the role of roughness summarized in figures 4.3-4.5.

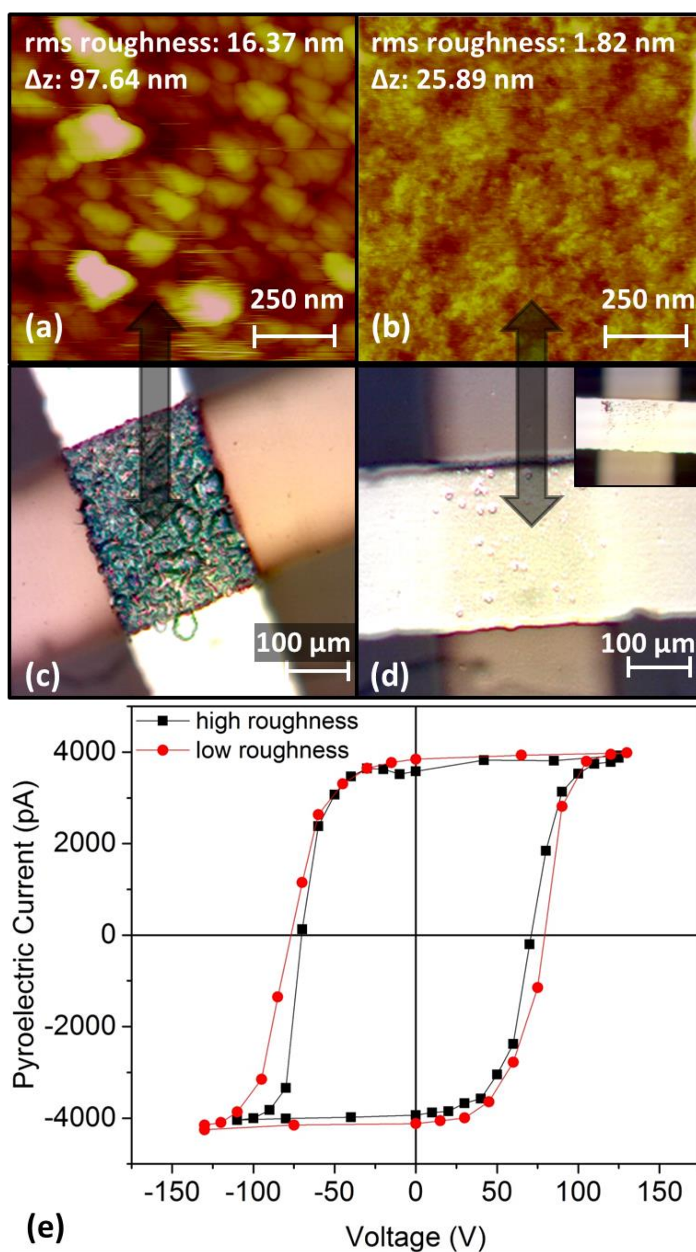

Figure 4.3: AFM measurements, photographs, and pyroelectric hysteresis loops from rough and smooth samples. The data in the left column along with the black hysteresis loop corresponds to rough samples, grown at high deposition rates (11.7 Å/s). The data in the right column along with

the red hysteresis loop corresponds to smooth samples, grown at low deposition rates (1.14 Å/s). (a) and (b) AFM measurements, showing a dramatic increase in surface roughness as deposition rate is increased. (c) Photograph of irreversible damage suffered by a rough sample after the application of voltage. (d) Photograph of a smooth sample after 15 polarization reversals showing no damage. The inset shows a smooth sample driven to failure via the application of large voltage. (e) Pyroelectric hysteresis loops of otherwise identical rough and smooth samples.

Figure 4.3 shows AFM and optical images of evaporated VDF oligomer thin films. Each column corresponds to distinct samples grown under identical growth conditions. The data in the left column, figures 4.3a and 4.3c, along with the black pyroelectric hysteresis loop in figure 4.3e, were taken on samples grown at high crucible temperatures (75 °C) corresponding to high deposition rates (11.7 Å/s). In contrast, the data in the right column, figures 4.3b and 4.3d, along with the red hysteresis loop in figure 4.3e were taken on samples grown at low crucible temperatures (48 °C) corresponding to low deposition rates (1.14 Å/s). The AFM images in figures 4.3a and 4.3b were recorded on the VDF oligomer thin films prior to the deposition of a top electrode and show that the films grown at high deposition rates have a higher root-mean-square (rms) roughness (20 nm versus less than 5 nm) and a larger maximum topographical peak-to-valley distance, Δz, than those grown at low deposition rates. Samples grown at a high deposition rate suffer electrical breakdown after only a few

(usually no more than two) polarization switches. In contrast, samples grown at a lower deposition rate survive the application of poling voltage and repeated polarization switching. Figure 4.3c is a true color photograph of a rough, high deposition rate sample taken through an optical microscope that shows irreversible damage appearing on the surface of the electrode after the first application of voltage. Figure 4.3d is a photograph of a smooth, low deposition rate sample that shows no significant damage, even after 15 polarization reversals. These differences only appear subsequent to voltage application. Although both rough and smooth films can be made to fail, the inset of figure 4.3d shows a smooth sample that was intentionally destroyed by applying high voltage (>100 V), much higher than that necessary to saturate the sample. Clearly, the electric field induced damage at the surface of the smooth sample is different than that suffered by the rough sample, indicating that the failure modes for rough and smooth samples are different.

Pyroelectric measurements on the few rough samples that do survive the application of voltage show that surface roughness does not correlate with the ferroelectric properties of VDF oligomer thin films, as demonstrated in figure 4.3e. This figure shows nearly identical pyroelectric hysteresis loops from two samples with identical thicknesses and areas even though one (black data) was much rougher than the other (red data). Rather, the role of roughness manifests itself in whether or not the sample can survive the application of voltage. The Al top electrode conforms to the topography of the VDF oligomer layer below it, so a rough VDF oligomer layer will cause large electric field variations across the electrode area at constant voltage, resulting in damage to the VDF oligomer and subsequent failure. This is illustrated in figure 4.4. When a constant voltage is held across a rough VDF oligomer thin film, thinner regions

of the film will be subjected to higher electric fields, given by $E = V/d$, where d is the thickness of the VDF oligomer film. If the film is sufficiently thin, the electric field in that region may greatly exceed the coercive field of the oligomer, resulting in damage to the film.

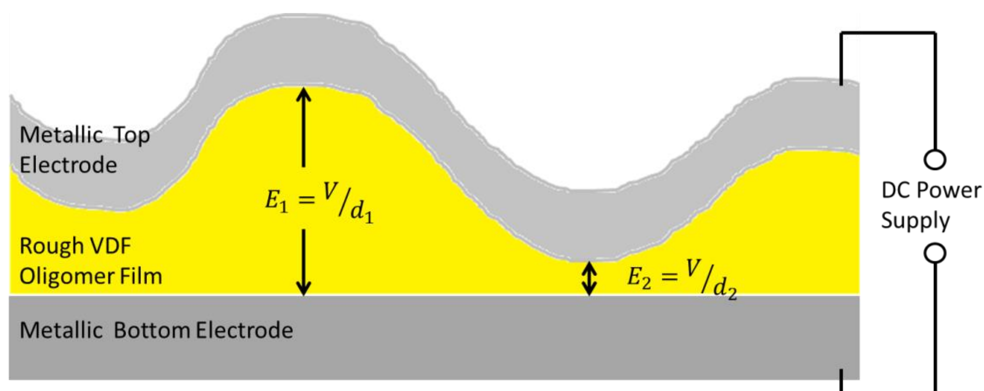

Figure 4.4: Illustration of roughness induced sample failure. Here, d_1 is much greater than d_2. When a constant voltage is held across the film, E_2 will be much greater than E_1, and may even exceed the coercive field of the VDF oligomer, causing damage and subsequent failure.

The role of roughness in the successful growth of ferroelectric, switchable VDF oligomer films is summarized in figures 4.5a and 4.5b. The histogram in figure 4.5a quantifies the role of maximum peak-to-valley distance, Δz, in successful sample yield for the subset of samples on which both AFM and pyroelectric measurements were made. The bins span 10 nm in Δz, with the last bin representing all Δz values greater than 100 nm. Each count represents one electrode from these samples, with red representing an electrode area on which a complete pyroelectric hysteresis loop was successfully obtained and black representing a failed electrode. As Δz approaches 70 nm, the yield rate falls significantly. Figure 4.5b, in turn, relates crucible temperature to Δz for this

same subset of samples showing that a crucible temperature between 50 °C and 60 °C is ideal. Depositions at very low crucible temperatures (40 °C or lower) were also attempted, but no pyroelectric current was measured on these samples regardless of surface roughness. Trace amounts of highly fragmented VDF oligomer chains were detected by mass spectrometry, and it is thought that at these low temperatures, only light fragments are deposited on the substrate.

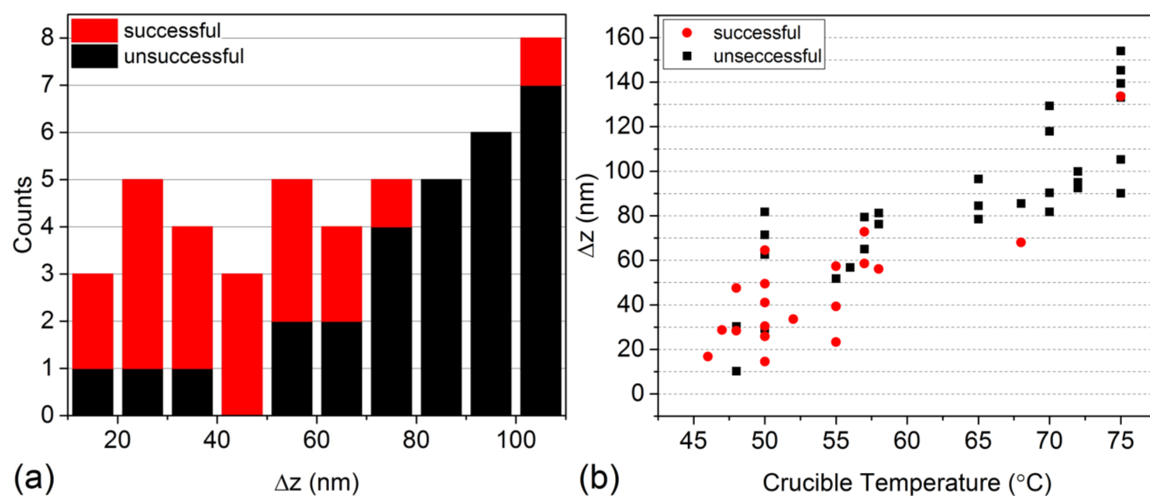

Figure 4.5: (a) Histogram showing the numbers of successful and unsuccessful samples as a function of maximum peak-to-valley distance, Δz. The last bin represents all Δz values greater than 100 nm. (b) Δz as a function of crucible temperature during deposition. Figures 4.5(a) and 4.5(b) together reveal the optimal deposition conditions to maximize yield.

With this newly refined parameter space for the growth of high quality ferroelectric thin films of VDF oligomer, thin film production can be restricted to these smooth (low deposition rate), switchable, robust films in order to probe the physical properties of these VDF oligomer films. Given the growing general interest in using

organic thin films in optical devices [2-6], the refractive index of VDF oligomer thin films is first reported. Using a spectroscopic ellipsometer, a technique that has already been used to successfully probe the optical properties of P(VDF-TrFE) films [43, 44], the large-scale topographical and optical properties of VDF oligomer thin films are investigated, with typical results shown in figure 4.6. The VDF oligomer films show uniaxial anisotropy, where the optical axis is perpendicular to the film surface. Figure 4.6a shows the ordinary (in-plane) index of refraction of a VDF oligomer thin film on Si over a sample area measuring 1.5 cm by 1.5 cm. The value of the refractive index at 632.8 nm wavelength is 1.42 with a small variation of ±0.012 (and a standard deviation of 0.004) across the full sample area. The relatively small variation in the index of refraction indicates a uniform film density. Furthermore, this value changes little as film deposition parameters are changed. Though the values for the refractive index for VDF oligomer thin films is not found in the literature, the refractive index for PVDF polymer films ranges from 1.42 to 1.52 [45-47]. The consistency of the index of refraction for VDF oligomer films measured from several samples indicates that regardless of deposition conditions, the density of the VDF oligomer film remains largely uniform, at least over the length scales of the measurement (300 μm). Spectroscopic ellipsometry also allows for the calculation of film thickness along with the index of refraction. Figure 4.6b shows a thickness map across the same sample area. Here, 0 nm on the vertical axis corresponds to the Co/VDF interface. The film thickness follows the expected $1/r^2$ dependence [48], where r is the distance between the sample and the source during deposition, as shown by the fit in the inset. In-depth detail on the modeling of the ellipsometry data can be found in references 38, 39, 43, and 44.

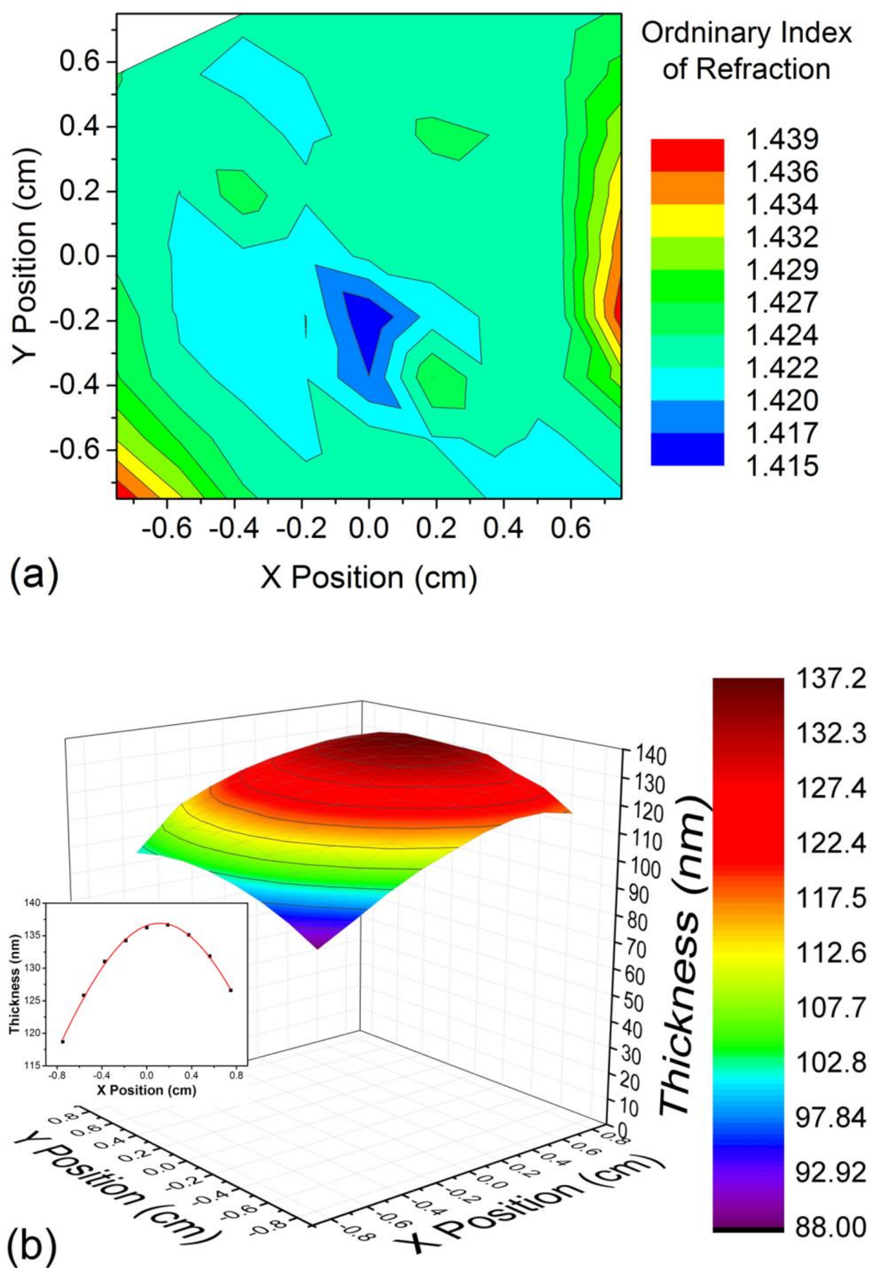

Figure 4.6: (a) Map of the ordinary component of the index of refraction over a large area for a VDF oligomer thin film measured using ellipsometry. The top left corner corresponds to the edge of the sample. (b) VDF oligomer film thickness map across the same area. The inset is a cross section of this map with a $1/r^2$ fit in red.

Although the VDF oligomer thickness is not uniform across large areas, over small electrode areas the thickness will be approximately uniform. For example, for the sample shown in figure 4.6b, the VDF oligomer thickness would change by only 1 nm across a typical 0.2-mm-wide electrode. Therefore, this $1/r^2$ change in film thickness can be dismissed for samples with sufficiently narrow electrodes, such as the archetypal sample structure shown in figure 4.7a. However, should one desire to perform an experiment that requires a large area electrode (figure 4.7b), such as Polarized Neutron Reflectometry (PNR), the change in VDF oligomer thickness across the electrode area becomes significant and plays a role similar to film roughness discussed above. For example, if the coercive field of the VDF oligomer is taken to be 95 MV/m (the determination of this value is discussed below), a sample with the electrode architecture shown in figure 4.7b and VDF oligomer thickness profile shown in figure 4.6b would require a voltage of 13.3 V held across the electrodes to fully polarize the VDF oligomer at the center (thickest region). However, that same 13.3 V would result in an electric field of 151 MV/m at the edges of the electrodes where the VDF oligomer is thinnest. This 151 MV/m electric field is more than 50% greater than the coercive field, and may result in damage to the VDF oligomer film. Indeed, many attempts were made to construct a sample with the architecture shown in figure 4.7b for PNR measurements, and in most cases damage could clearly be seen propagating inwards from the edges of the electrodes (thinnest VDF oligomer) to the center (thickest VDF electrodes) upon the application of incrementally increasing voltage. As a result, it is extremely difficult to saturate the polarization of a sample with this structure across its entire area.

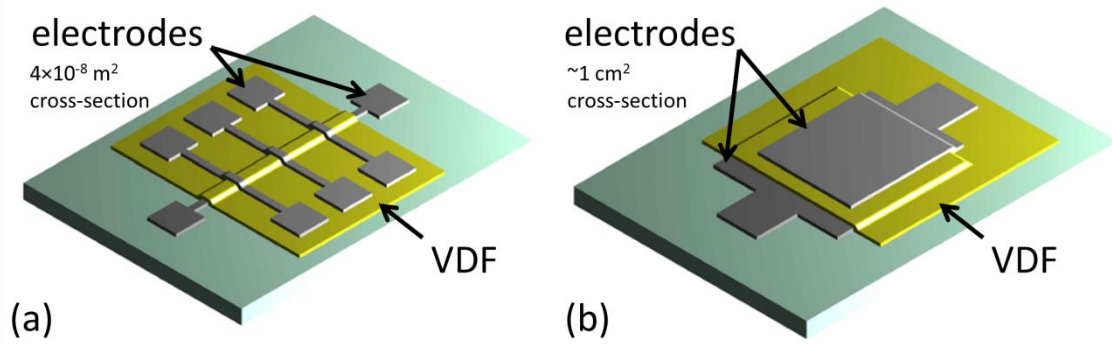

Figure 4.7: Two typical sample architectures with (a) small area and (b) large area electrode cross-sections. The use of small electrode cross-sections can mitigate problems caused by VDF oligomer thickness variations, but some measurements, such as PNR, require large area cross-sections.

Next, to determine the Curie temperature of these VDF oligomer thin films, the pyroelectric current is measured as a function of film temperature. The pyroelectric current, I_p, is given by [37]:

$$I_p = A\left(\frac{dP}{dT}\right)\left(\frac{dT}{dt}\right) \tag{4.2}$$

where, A is the area of the electrode, dP/dT is the change in spontaneous polarization with temperature, and dT/dt is the rate of change of temperature. Experiments by Noda et al. on VDF oligomer thin films show that the detected current is dominated by the pyroelectric current and that any non-pyroelectric, temperature-dependent generated current is small in comparison [31]. Using the Chynoweth method and following the discussion in reference 37, for a given light intensity the pyroelectric current is

proportional to the slope of the polarization curve with temperature, dP/dT. The slope of the P vs T curve for a ferroelectric increases close to the Curie temperature and is a maximum at that temperature. Because the ferroelectric transition is first order [49, 50], there exists a finite temperature range near the transition temperature in which both the ferro- and paraelectric phases coexist. In this coexistence regime, the pyroelectric electric current does not instantaneously drop to zero once the transition temperature has been reached. Rather, the current should increase as the transition temperature is approached and then decrease over a finite temperature range close to the transition temperature, which is exactly the temperature dependence observed in figure 4.8. This figure shows the measured pyroelectric current of a saturated 500 nm thick VDF oligomer thin film at zero applied voltage as a function of temperature. The temperature was raised from 19 °C to 90 °C at a rate of 3 °C/minute. (This method has been previously used to determine the transition temperature, 88 °C, in Langmuir-Blodgett deposited P(VDF-TrFE 70:30) thin films [51].) For the sample shown in figure 4.8, the magnitude of the pyroelectric current at room temperature, subsequent to this heating cycle, is only 14% of its original value prior to heating. Saturating the sample, with the application of 60 V across the VDF oligomer thin film, increases the magnitude of the pyroelectric current to 40% of its original value. From these data, it is concluded that the Curie temperature for these films is 61 °C, and that the film partially depolarized and suffered damage upon further heating to 90 °C.

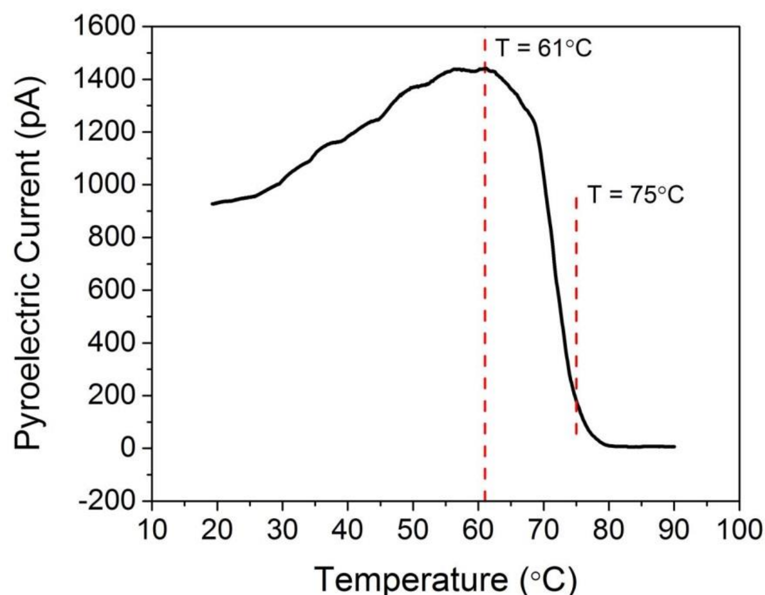

Figure 4.8: Pyroelectric current as a function of temperature. The pyroelectric current rises with temperature until the film reaches 61 °C. With increasing temperature, the current decreases as the film transitions from the ferro- to paraelectric phase, going to zero at 80 °C.

To investigate the film damage mechanism at temperatures above the transition temperature, an optical microscope movie, digital video 4.1, was made of the effects of temperature on VDF oligomer thin films, showing a dramatic change in the film at a temperature close to 75 °C (second dotted line in figure 4.8). Still frames from digital video 4.1 are shown in figure 4.9. From the movie, it is determined that the film begins to melt at 75 °C. The bubbles in the film shown in figure 4.9 remain even when cooled to room temperature, which, along with the decrease in pyroelectric current at saturation, indicates that permanent structural damage occurs in the film upon melting. Earlier differential scanning calorimetry measurements [52] on VDF oligomer powders with the same end groups as those used here indicate a melting temperature of 95 °C for chain

length n = 14. This difference may be attributable to thin film growth, as earlier results on vapor deposited thin films [53] of VDF oligomer (albeit with different end groups) showed a substantially lower melting temperature of thin films as compared to powders, with a difference that is highly dependent on crucible temperature.

Digital Video 4.1: A movie of a VDF oligomer thin film heated from room temperature to 81 °C. The film clearly starts to melt starting at 75 °C. The movie can be viewed at https://www.youtube.com/watch?v=0OrAySUlU0I

Figure 4.9: Still frames from digital video 4.1, a movie of a VDF oligomer thin film on a Pt/Co electrode being heated. For reference, the movie is taken at the location where the thin strip (bottom of the still frame) meets the square pad (see figure 4.1) of the bottom electrode. The film undergoes a dramatic change around 75 °C. At 80 °C, the pyroelectric signal disappears and bubble-like features appear on the surface of the film and remain even after the film is cooled back down to room temperature.

The data in figure 4.8 and 4.9 indicate there is a narrow temperature range, above the ferroelectric transition and below the melting temperature [54], suitable for annealing. VDF oligomer films were annealed in air at 68 °C for 90 minutes, with ramp times of 90 minutes for both increasing and decreasing temperature. The effects of annealing were analyzed via XRD measurements and the results are shown in the top two panes of figure 4.10. Before annealing, the (020) β-phase VDF oligomer ($2\theta = 23.8°$) was dominant, with no (110) β-phase VDF oligomer ($2\theta = 24.4°$) detected. After annealing, however, the (110) β-phase is dominant, with a 20:1 ratio of (110) to (020) β-phase, while the total area under all peaks remained constant. Calculated Scherrer particle sizes, in this case for the majority (110) β-phase, are similar to those from the majority (020) β-phase before annealing, ranging from 11.1 nm to 12.6 nm. Repeated measurements on multiple

samples consistently showed this shift in crystalline orientation upon annealing. Similar to Langmuir-Blodgett deposited PVDF thin films, however, annealing these VDF oligomer thin films caused no appreciable change in the observed pyroelectric hysteresis loops. This behavior is not surprising, because the ferroelectric polarization is directed along the (020) direction. Polarization measurements along the (110) direction will result in only a 13.4% reduction in the out-of-plane component of polarization since the ferroelectric polarization is canted 30° away from the (110) direction. This data suggests that annealing is unnecessary, as it decreases the out-of-plane polarization and does not significantly improve the crystallinity of the VDF oligomer thin film. Nevertheless, more experiments regarding the usefulness of annealing were performed and are discussed later in this chapter.

Because the reduction in pyroelectric current upon heating described above may result from sample melting, phase changes, or perhaps even from evaporation of the film off the substrate, room temperature XRD measurements were taken on VDF oligomer thin film samples heated to different temperatures, with the results shown in the middle panes of figure 4.10. Heating to 75 °C, results in a substantial decrease (by a factor of 60) of the area under the peak corresponding to the (110) orientation of the β-phase. This peak disappears entirely upon heating to 98 °C, well past the melting temperature. However, the peaks for the non-ferroelectric (110) α-phase and the (020) β-phase, at 2θ = 23.1° and 23.8° respectively, are still present, albeit reduced in area. The reductions in the areas under these peaks are much less pronounced than that of the (110) β-phase peak: heating to 75 °C reduces the areas under the (110) α-phase and (020) β-phase peaks by a factor of 3, while heating to 98 °C results in a further reduction of 1.3. The total area

under all the peaks, a measure of crystallinity, decreases by a factor of 24 after heating to 75 °C, and by an additional factor of 2 when heating to 98 °C, indicating a loss of crystallinity. The insets in the middle panes of figure 4.10 show optical microscopy photographs of the samples corresponding to the XRD data after cooling back to room temperature. In addition to the (110) β-phase VDF oligomer peak completely disappearing after raising the film's temperature to 98 °C, the bubble-like features have completely disappeared as well. Films heated to this temperature show no pyroelectric current after cooling to room temperature. However, films heated to 90 °C still showed some pyroelectric current upon cooling and re-saturation (see discussion on figure 4.8 above), which can now be attributed to the small remaining fraction of (020) β-phase VDF oligomer. The persistence of the preferred (020) β-phase peak may be attributed to partial recrystallization upon cooling. Clearly the fraction of the material that recrystallizes in this fashion is small. It is possible, but unlikely, that the material recrystallizes into a higher index orientation on cooling. Another, more likely possibility is that the VDF oligomer evaporates away from the substrate when heated to these high temperatures. The exact details of the process remain an open question.

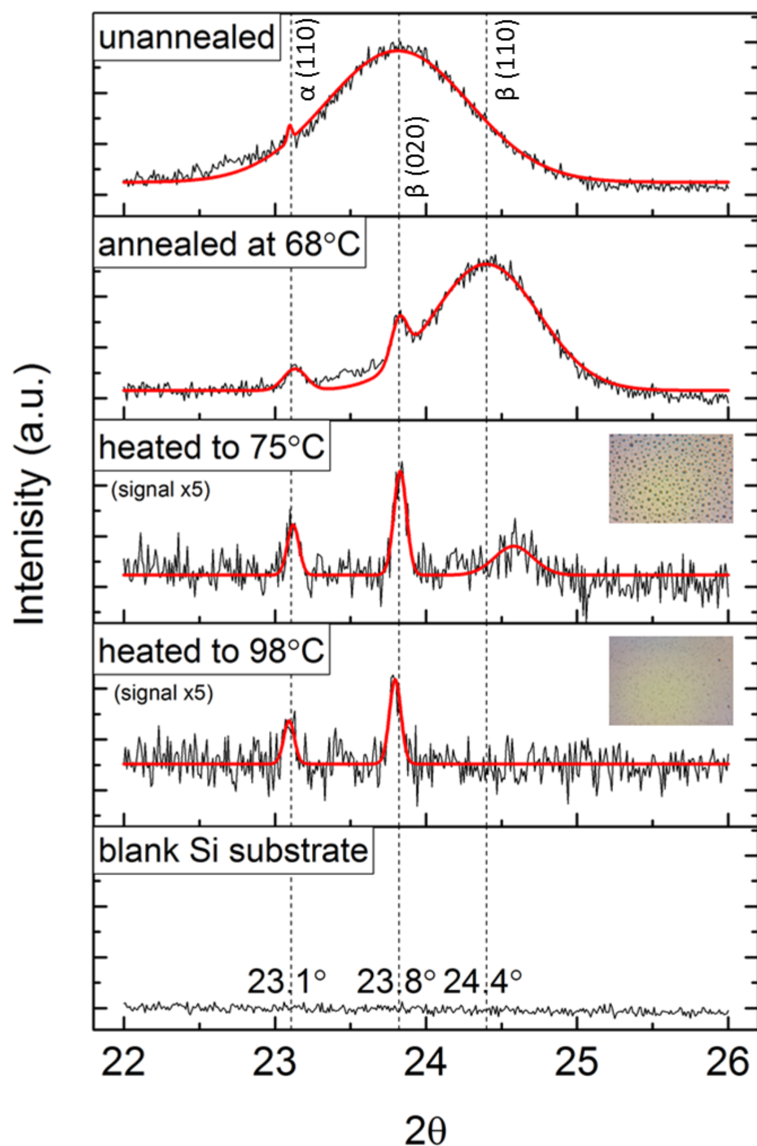

Figure 4.10: Room temperature XRD data (from top to bottom) for an as-grown, unannealed VDF oligomer thin film, after annealing at 68 °C for 90 minutes, after heating at 75 °C, after heating at 98 °C, and for a blank Si substrate for reference. Annealing clearly increases the proportion of (110) to (020) β-phase VDF oligomer in the film. The insets are photographs of the melted films after cooling. Note that the vertical axes in the third and fourth panes are multiplied by a factor of five.

As detailed above, the top two panels of figure 4.10 suggest that annealing is unnecessary. To determine conclusively whether these VDF oligomer thin films benefit, in any way, from thermal annealing, several more samples were grown and heat treated/annealed under similar conditions. The samples' structure consisted of VDF oligomer deposited on Si wafers. XRD and AFM measurements were performed on each sample before and after thermal annealing. The heat treating/annealing process itself was performed using a programmable oven. Each sample was heat treated/annealed using a trapezoidal temperature vs. time profile, starting and ending at room temperature. The rise, plateau, and fall times of each trapezoidal annealing profile were equal. The annealing conditions, rise/plateau/fall time and plateau temperature, and the resulting changes in Scherrer particle size (τ), surface roughness (roughness), and the maximum change in the peak-to-valley distance (Δz) are shown in table 4.1 below.

Annealing Conditions		Resulting Change		
Rise/Plateau/ Fall Time	**Plateau Temp.**	**τ (nm)**	**roughness (nm)**	**Δz (nm)**
1 hr.	50 °C	0.38 ± 0.39	2.53	-5.05
1 hr.	55 °C	1.78 ± 0.28	1.16	43.68
1 hr.	60 °C	2.09 ± 0.67	-1.35	-8.59
1 hr.	65 °C	2.67 ± 1.64	159.75	717.46
2 hr.	50 °C	2.17 ± 0.41	-3.11	-6.57
2 hr.	55 °C	2.06 ± 0.39	-0.62	46.31
2 hr.	60 °C	0.92 ± 1.67	74.52	724.22

Table 4.1: Tabulated results of the effects of heat treating/annealing as determined by XRD and AFM measurements. There was marginal improvement to the Scherrer particle size (τ) at the expense of roughness and maximum peak-to-valley distance.

From the table, it is clear that annealing improves the crystallinity of the VDF oligomer thin films. However, this small improvement comes at both the expense of preferred dipole orientation (recall the repeatedly observed shift in the β-phase peak from the (020) to the (110) orientation) and sample roughness. In some instances, annealing completely destroyed the film, as indicated by the enormous increase in Δz, and visible damage to the film similar to that shown in figure 4.9. Still, several additional samples

were grown to test the effects of annealing on the pyroelectric response of the VDF oligomer thin films. These samples had the same structure as that shown in figure 4.1, except after the deposition of the VDF oligomer thin film the samples were cut in half. One half was annealed while the other half was not, followed by the deposition of the Al top electrodes on both halves. Upon comparison of pyroelectric hysteresis measurements, there was no significant difference in the hysteresis loops between the annealed and unannealed samples as well as no improvement in sample lifetime, i.e. the number of times the ferroelectric polarization direction could be switched before sample failure. From the data in figure 4.10 and table 4.1, it is concluded that annealing is unnecessary and perhaps even slightly detrimental: Annealing slightly improves crystallinity, but decreases the out-of-plane polarization, increases roughness and maximum peak-to-valley distance, and does not improve the pyroelectric response of the VDF oligomer thin films.

Finally, the ferroelectric coercive field, E_c, of evaporated VDF oligomer thin films was measured as a function of film thickness and temperature. The switching field is an intrinsic material property and should not vary with deposition parameters such as thickness and deposition rate. The observed extrinsic field, however, often differs from the predicted intrinsic field due to domain nucleation. Previously reported values of E_c for VDF oligomer thin films range from 75 MV/m to 120 MV/m at room temperature [27, 31, 33] and in one case was as high as 300 MV/m [35]. Figure 4.11a shows the switching voltage for VDF oligomer thin films (both annealed and unannealed since there is no appreciable difference) as a function of film thickness, with error bars calculated from the known $1/r^2$ thickness variation (see above). The switching voltage increases

linearly with thickness in the submicron regime, but eventually saturates for films thicker than ~1 μm. This behavior is in line with expectations, where an increase in thickness results in a higher density of defects and increases the likelihood of domain nucleation. A linear fit to the data in the submicron regime indicates an average coercive field of 95 MV/m, in line with earlier measurements. The temperature variation of the hysteresis loops is shown in figure 4.11b on an annealed sample with a total thickness of 510 nm, and show a decrease in the switching voltage, V_c, as film temperature increases. Figure 4.11c shows the coercive field, E_c, calculated from V_c taken from the right side of each hysteresis loop in figure 4.11b. The coercive field decreases as film temperature increases, which is indeed the expected behavior and in good agreement with similar measurements taken on P(VDF-TrFE 70:30) thin films [55, 56]. These results can be compared to the intrinsic coercive field predicted by the Landau-Ginzburg (LG) mean-field theory, which is given by [56]:

$$E_c = E_{c0} f(t) \tag{4.3}$$

$$E_{c0} = \frac{6}{25}\sqrt{\frac{3}{5}}\frac{|\beta|^{5/2}}{\gamma^{3/2}} \tag{4.4}$$

$$f(t) = \left[\frac{1}{\sqrt{2}}\sqrt{1+\sqrt{1-\frac{5}{9}t}}\right]\left[\frac{1}{2}\left(1+\sqrt{1-\frac{5}{9}t}-\frac{5}{3}t\right)\right] \tag{4.5}$$

Here, $t = 4\alpha_0(T - T_0)\gamma/\beta^2$ is the reduced temperature, and $T_0 = T_c - 3\beta^2/16\alpha_0\gamma$. The LG free energy coefficients α_0, β, and γ are independent of temperature. For this cursory check, the values of α_0, β, and γ for P(VDF-TrFE) are used [56]: $\alpha_0 = 7.5 \times 10^7$ $JmC^{-2}K^{-1}$, $\beta = -1.9 \times 10^{12}$ Jm^5C^{-4}, and $\gamma = 1.9 \times 10^{14}$ Jm^9C^{-6}. Taking $T_c = 61$ °C and using the values

of the LG free energy coefficients above gives T_0 = 13.5 °C. The blue line in figure 4.11c is the calculated intrinsic coercive field using equation 4.3, and has a slope approximately four times higher than the linear fit of the measured extrinsic field. The discrepancy between the calculated values for the intrinsic field and the measured coercive fields may be reduced by using the as-yet unknown LG free energy coefficients for the VDF oligomer, but are unlikely to reduce it enough to match the measured field. This mismatch is not surprising because one is unlikely to measure the intrinsic field at this large thickness. However, LG mean-field theory does predict the monotonic decrease in coercive field with temperature that is measured here.

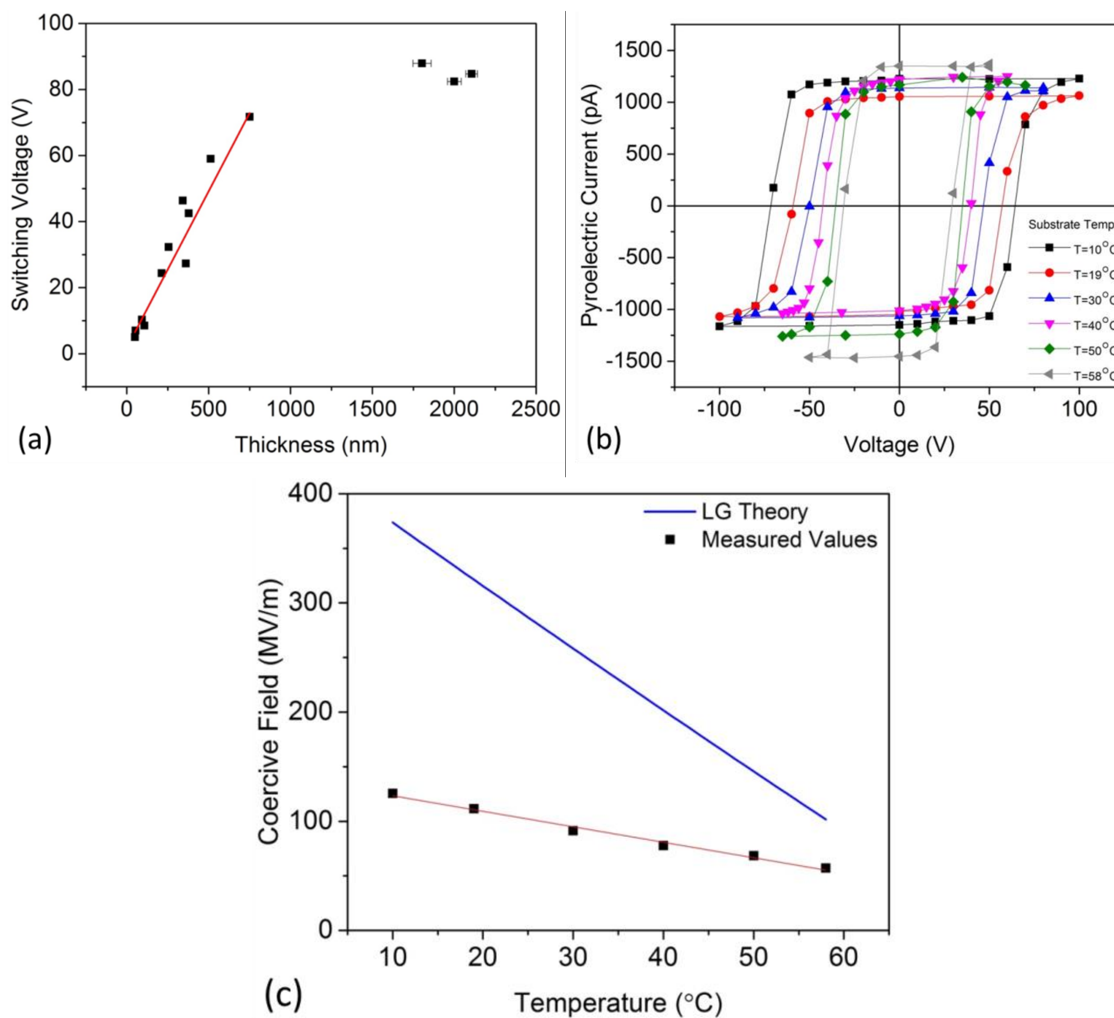

Figure 4.11: (a) VDF oligomer thin film switching voltage as a function of film thickness. The linear fit (red line) indicates a coercive field of 95MV/m. (b) VDF oligomer thin film pyroelectric hysteresis loops for various film temperatures. (c) Coercive field measurements as a function of temperature. The red line is a linear fit to the measured data, while the blue line is the calculated coercive field given by equation 4.3.

4.4 Conclusions

Ferroelectric organic oligomers such as VDF oligomer are attractive alternatives to both conventional oxide materials and ferroelectric polymers. The thermal evaporation of VDF oligomer thin films has been investigated and optimized, resulting in the ability to reliably and reproducibly grow organic ferroelectric thin films of the appropriate phase and orientation in a clean vacuum environment. This vacuum deposition is necessary for producing pristine and well-characterized interfaces.

Extensive XRD, AFM, ellipsometry, and pyroelectric measurements have allowed for the definition of parameters for successful VDF oligomer thin film deposition, maximizing the proportion of the ferroelectric β-phase with out-of-plane polarization. The highest yield of successful films is obtained for substrate temperatures at or below 130 K and crucible temperatures between 50 °C and 60 °C which correspond to a low deposition rate (below 2.0 Å/s) which in turn minimizes film roughness. The maximum peak-to-valley distance, as obtained from AFM measurements, must be below 70 nm. A post deposition anneal at 68 °C for at least 90 minutes results in a high proportion of the (110) to (020) β-phase without damaging the sample. It is concluded that post annealing is unnecessary, since the largest out-of-plane polarization occurs for the orientation of the as-grown films.

The growth of high quality films allowed for measurements of the properties of VDF oligomer thin films, many of which have not been previously reported. Among these properties are the ferroelectric Curie temperature of 61 °C and the index of refraction. Ellipsometry measurements show that the index of refraction at $\lambda = 632.8$ nm is $n = 1.42$ with very little variation, whether across a single film or between films grown

under very different deposition conditions. This value is comparable to, but more consistent than, the refractive index of PVDF films, which range between 1.42 and 1.52. Temperatures above 75 °C result in permanent structural damage due to melting with complete destruction occurring at 98 °C. Extensive pyroelectric hysteresis measurements reveal that the coercive field at room temperature for VDF oligomer films in the submicron regime is fairly constant at 95 MV/m. The temperature dependence of the coercive field follows the expected behavior (decreasing with increasing temperature) as predicted by LG mean-field theory.

In conclusion, this chapter has shown that the VDF oligomer is a strong candidate for use as a vacuum deposited ferroelectric thin film. The work presented in this chapter also maps the deposition parameter space for the VDF oligomer thin films, and reports on their physical properties, increasing the viability of VDF oligomer thin films as a channel to explore new physics and develop new devices based on organic electronics.

4.5 Acknowledgements

Financial support is provided by the National Science Foundation (NSF) (Grant No. ECCS-1101256) and by the NSF through the Nebraska Materials Research Science and Engineering Center (MRSEC) (Grant No. DMR-1420645). This research was performed in part in the Nebraska Nanoscale Facility: National Nanotechnology Coordinated Infrastructure and the Nebraska Center for Materials and Nanoscience (NCMN), which are supported by the NSF under Award ECCS-1542182, and the Nebraska Research Initiative.

4.6 References

1. C. P. Jarrett, R. H. Friend, A. R. Brown, and D. M. de Leeuw, J. Appl. Phys. **77**, 6289 (1995)
2. S. W. Seo, H. Chae, S. J. Seo, H. K. Chung, and S. M. Cho, Appl. Phys. Lett. **102**, 161908 (2013)
3. A. K. Ghosh and T. Feng, J. Appl. Phys. **44**, 2781 (1973)
4. A. K. Ghosh, D. L. Morel, T. Feng, R. F. Shaw, and C. A. Rowe, Jr., J. Appl. Phys. **45**, 230 (1974)
5. A. K. Ghosh and T. Feng, J. Appl. Phys. **49**, 12 (1978)
6. D. Z. Garbuzov, S. R. Forrest, A. G. Tsekoun, P. E. Burrows, V. Bulovic, and M. E. Thompson, J. Appl. Phys. **80**, 4644 (1996)
7. A. Mardana, M. Bai, A. Baruth, S. Ducharme, and S. Adenwalla, Appl. Phys. Lett. **97**, 112904 (2010)
8. T. S. Santos, J. S. Lee, P. Migdal, I. C. Lekshmi, B. Satpati, and J. S. Moodera, Phys. Rev. Lett. **98**, 016601 (2007)
9. J. M. Lopez-Encarnacion, J. D. Burton, E. Y. Tsymbal, and J .P. Velev, Nano Lett. **11**, 599 (2011)
10. J. P. Velev, J. M. Lopez-Encarnacion, J. D. Burton, and E. Y. Tsymbal, Phys. Rev. B **85**, 125103 (2012)
11. D. Y. Kusuma and P. S. Lee, Adv. Mater. **24**, 4163 (2012)
12. H. Ohno, D. Chiba, F. Matsukura, T. Omiya, E. Abe, T. Dietl, Y. Ohno, and K. Ohtani, Nature **408**, 944 (2000)

13. D. Chiba, M. Sawicki, Y. Nishitani, Y. Nakatani, F. Matsukura, and H. Ohno, Nature **455**, 515 (2008)

14. M. Bibes, and A. Barthélémy, Nature Mater. **7**, 425 (2008)

15. A. Mardana, S. Ducharme, and S. Adenwalla, Nano Lett. **11**, 3862 (2011)

16. M. Endo, S. Kanai, S. Ikeda, F. Matsukura, and H. Ohno, Appl. Phys. Lett. **96**, 212503 (2010)

17. W. G. Wang, M. Li, S. Hageman, and C. L. Chien, Nature Mater. **11**, 64 (2011)

18. T. Maruyama, Y. Shiota, T. Nozaki, K. Ohta, N. Toda, M. Mizuguchi, A. A. Tulapurkar, T. Shinjo, M. Shiraishi, S. Mizukami, Y. Ando, and Y. Suzuki, Nature Nanotech. **4**, 158 (2009)

19. D. Chiba, M. Yamanouchi, F. Matsukura, and H. Ohno, Science **301**, 943 (2003)

20. V. B. Naik, H. Meng, R. S. Liu, P. Luo, S. Yap, and G. C. Han, Appl. Phys. Lett. **104**, 232401 (2014)

21. M. Fiebig, J. Phys. D: Appl. Phys. **38**, R123 (2005)

22. J. Ma, J. Hu, Z. Li, and C. W. Nan, Adv. Mater. **23**, 1062 (2011)

23. N. X. Sun and G. Srinivasan, Spin **2**, 1240004 (2012)

24. S. Zhang, Phys. Rev. Lett. **83**, 640 (1999)

25. C. G. Duan, J. P. Velev, R. F. Sabirianov, Z. Zhu, J. Chu, S. S. Jaswal, and E. Y. Tsymbal, Phys. Rev. Lett. **101**, 137201 (2008)

26. P. V. Lukashev, T. R. Paudel, J. M. Lopez-Encarnacion, S. Adenwalla, E. Y. Tsymbal, and J. P. Velev, ACS Nano **6**, 9745 (2012)

27. K. Noda, K. Ishida, A. Kubono, T. Horiuchi, and H. Yamada, J. Appl. Phys. **93**, 2866 (2003)

28. T. Furukawa, M. Date, and E. Fukada, J. Appl. Phys. **51**, 1135 (1980)

29. K. Foreman, C. Labedz, M. Shearer, and S. Adenwalla, Rev. Sci. Instrum. **85**, 043902 (2014)

30. K. Noda, K. Ishida, A, Kubono, T. Horiuchi, H. Yamada, and K. Matsushige, Jpn. J. Appl. Phys. **40**, 4361 (2001)

31. K. Noda, K. Ishida, T. Horiuchi, H. Yamada, and K. Matsushige, Jpn. J. Appl. Phys. **42**, 1334 (2003)

32. S. Kuwajima, S. Horie, T. Horiuchi, H. Yamada, K. Matsushige, and K. Ishida, Macromolecules **42**, 3353 (2009)

33. H. Xu, G. Li, Y. Zhang, X. Zhang, Y. Gu, D. Shen, and X. Meng, J. Appl. Phys. **107**, 034101 (2010)

34. K. Noda, K. Ishida, T. Horiuchi, K. Matsushige, and A. Kubono, J. Appl. Phys. **86**, 3688 (1999)

35. K. Noda, K. Ishida, A. Kubono, T. Horiuchi, H. Yamada, and K. Matsushige, Jpn. J. Appl. Phys. **39**, 6358 (2000)

36. R. Hasegawa, M. Kobayashi, and H. Tadokoro, Polym. J. **3**, 591 (1972)

37. A. G. Chynoweth, J. Appl. Phys. **27**, 78 (1956)

38. J. A. Woollam, B. Johs, C. Herzinger, J. Hilfiker, R. Synowicki, and C. Bungay, SPIE Proceedings, CR27, **3** (1999)

39. J. A. Woollam, B. Johs, C. Herzinger, J. Hilfiker, R. Synowicki, and C. Bungay, SPIE Proceedings, CR27, **29** (1999)

40. A. Takeno, N. Okui, T. Kitoh, M. Muraoka, S. Umemoto, and T. Sakai, Thin Solid Films **202**, 205 (1991)

41. ICDD 2013 *International Center for Diffraction Data* Card No. 00-042-1649

42. ICDD 2013 *International Center for Diffraction Data* Card No. 00-042-1650

43. M. Bai, A. V. Sorokin, D. W. Thompson, M. Poulsen, S. Ducharme, C. M. Herzinger, S. Palto, V. M. Fridkin, S. G. Yudin, V. E. Savchenko, and L. K. Gribova, J. Appl. Phys. **95**, 3372 (2004)

44. Y. X. Li, L. Yan, R. P. Shrestha, D. Yang, Z. Ounaies, and E. A. Irene, Thin Solid Films **513**, 283 (2006)

45. C. G Duan, W. N. Mai, W. Yin, J. Liu, J. R. Hardy, M. Bai, and S. Ducharme, J. Phys. Condens. Matter **15**, 3805 (2003)

46. X. Yingxue, F. Huiqing, L. Weiguo, Y. Chen, and N. Xiaoling, Surface Rev. and Lett. **15**, 175 (2008)

47. D. Broussoux and F. Micheron, J. Appl. Phys. **51**, 2020 (1980)

48. R. Glang, *Handbook of Thin Film Technology*, edited by L. I. Maissel and R. Glang (McGraw-Hill, New York, 1970), pp. 1-56

49. K. Kimura and H. Ohigashi, Appl. Phys. Lett. **43**, 834 (1983)

50. T. Furukawa, Ferroelectrics **57**, 63 (1984)

51. A. V. Bune, C. Zhu, S. Ducharme, L. M. Blinov, V. M. Fridkin, S. P. Palto, N. G. Petukhova, and S. G. Yudin, J. Appl. Phys. **85**, 7869 (1999)

52. "Phase Transitions in Vinylidene Fluoride Oligomer," R. Korlacki, J. T. Johnston, J. Kim, K. L. Kraemer, S. Ducharme, Z. Ge, L. Kobryn, J. M. Takacs, and S. M. Nakhmanson, International Symposium on Ferroelectrics and Functionalities, Colorado Springs, 27 Sept. to 1 Oct. 2009. Poster presentation

53. Herman, S. Umemoto, T. Kikutani, and N. Okui, Polym. J. **30**, 659 (1998)

54. T. Furukawa, Phase Trans. **18**, 143 (1989)

55. X. Zhang, H. Xu, and Y. Zhang, J. Phys. D: Appl. Phys. **44**, 155501 (2011)

56. S. Ducharme, V. M. Fridkin, A. V. Bune, S. P. Palto, L. M. Blinov, N. N. Petukhova, and S. G. Yudin, Phys. Rev. Lett. **84**, 175 (2000)

CHAPTER 5

THE METAL/ORGANIC INTERFACE IN COBALT/VINYLIDENE FLUORIDE HETEROSTRUCTURES

This chapter is based on the published paper: *The Metal/Organic Interface in Cobalt/Vinylidene Fluoride Heterostructures*, K. Foreman, E. Echeverria, M. A. Koten, R. M. Lindsay, N. Hong, J. Shield, and S. Adenwalla, Mater. Res. Express **3**, 116403 (2016). Reprinted with the permission of IOP Publishing.

5.1 Introduction

The ease of processing, increased device functionality, and price of organic-based electronics has led to a rapid increase in their development and usage. Organic materials have applications in light emission [1-3], solar cells [4-8], and even flexible electronics [9-11]. Perhaps the largest driving force behind this rapid growth is the customizable nature of organic molecules which can be designed and constructed to suit specific applications. These "designer molecules" can be used, for example, to tune band gaps and induce gap states in organic/metallic junctions [12], in striking contrast to inorganics, that do not afford anywhere near this degree of customization. Predictions indicate that the value of the organic electronics market will more than double, to nearly $70 billion [13], by 2026.

The present work is driven by previous experiments on the electric-field control of magnetic anisotropy in organic ferroelectric/metallic ferromagnetic heterostructures. Theoretical modeling [14] and experiments [15] have shown that the easy axis of a

ferromagnetic Co thin film can be switched from in-plane to out-of-plane, or *vice versa*, by simply switching the polarization direction of a polymer ferroelectric poly(vinylidene fluoride) (PVDF) thin film deposited on the Co. Induced spin-dependent charge screening [16] in the ferromagnetic Co thin film, due to the electric field generated by the polarized ferroelectric film, changes the surface magnetocrystalline anisotropy of the Co by up to 50% upon polarization switching. This change is large enough to reorient the easy axis of thin Co films.

Crucial to all organic-based electronics is the interface between the organic material and the metallic electrodes. The interface plays a vital role in charge injection and transport in many devices [17], and in the example above, the quality of the metal/organic interface affects the magnitude of the magnetoelectric coupling. In the Co/PVDF heterostructures [15], the polymer ferroelectric was deposited using Langmuir-Blodgett (LB) deposition, exposing the Co surface to atmosphere, resulting in uncontrolled oxidation of the surface, as well as exposing the surface to water in the LB trough. The oxidation of high Curie temperature ferromagnets, such as Co, also causes challenges for other applications, such as spintronics, as this oxidation changes the spin polarization at the surface. The work described in Chapter 4 on the optimal conditions for successful vacuum thermal evaporation of ferroelectric vinylidene fluoride (VDF) oligomer films [18] allows for the investigation of the interface between Co and VDF oligomer, as the exposure time and conditions between the depositions of the two films can be controlled. The VDF oligomer is an organic ferroelectric with unique properties for device applications. While PVDF is already commonly used on an industrial scale,

the VDF oligomer features better crystallinity, a higher surface charge density, and most importantly, can be deposited under vacuum conditions [18].

The objectives of the work in this chapter are twofold: to investigate the efficacy of a VDF oligomer thin film as a capping layer for Co, an important high Curie temperature ferromagnetic material, and to characterize the interface between the VDF oligomer and Co thin films. Investigations into the former also clarify the time dependence of oxidation for Co thin films, a topic on which there are many contradictory reports. The work in this chapter could help guide both future magnetoelectric coupling experiments (an important research thrust in its own right) and more general experiments using organic and metal thin film heterostructures.

5.2 Sample Preparation and Experimental Methods

The metallic and organic thin films comprising the heterostructures were grown in a sputtering/e-beam evaporation chamber and a custom thermal evaporation chamber [19], respectively. The two chambers are connected via a gate valve so that the entire heterostructure can be made without breaking vacuum. Samples used for magnetic measurements were grown on 1 mm thick glass substrates, while those used for scanning transmission electron microscopy (STEM) and x-ray photoelectron spectroscopy (XPS) measurements were grown on Si substrates. In both cases the heterostructures consisted of Pt (50 nm)/Co (1.0-1.2 nm)/VDF (10-500 nm). The base pressures of the sputtering/e-beam and thermal evaporation chambers were 1×10^{-8} Torr and 8×10^{-8} Torr, respectively. Metallic thin films were deposited at rates of 0.2-0.5 Å/s, measured by a quartz crystal oscillator. VDF oligomer powder, CF_3-$(CH_2CF_2)_n$-I, was provided by Daikin Industries,

Ltd., with n = 14±1 as measured by mass spectroscopy. The VDF oligomer thin films were deposited at a rate of 1 Å/s, confirmed by external optical ellipsometry measurements. Recent advances in the thermal evaporation of VDF oligomer thin films allowed for the deposition of high quality ferroelectric films [18]. The reader is referred to Chapters 3 and 4 for further detail on the deposition of these VDF oligomer thin films.

Optical ellipsometry measurements were performed using a J.A. Woollam M-2000 DI spectroscopic rotating compensator ellipsometer. The map of film thickness across sample area (shown below) was recorded using a beam diameter of 300 μm by measuring 121 points in a sample area measuring 2 cm by 2 cm. The data were fit using CompleteEASE® software [20].

Magnetic hysteresis measurements of the Co thin films were performed in ambient, atmospheric conditions using the magneto-optic Kerr effect (MOKE) [21]. Potential magnetoelectric devices require that the VDF oligomer be in the ferroelectric β-phase chain conformation [22], as opposed to other non-ferroelectric chain conformations. To ensure that the interface between *ferroelectric* VDF oligomer and Co was being characterized, pyroelectric hysteresis measurements of the VDF oligomer films were performed on selected samples. These measurements were performed using the Chynoweth method [23] with a 1 mW, 658 nm wavelength diode laser modulated with an optical chopper at 2 kHz.

Two Pt/Co/VDF heterostructure cross-sectional STEM samples were prepared in an FEI Helios 660 dual-beam instrument. The bare VDF oligomer surface was first covered by a 2 μm thick amorphous C layer to protect the film from the ion beam during the milling process. The sample was mounted on a single-tilt holder inside a 200 kV FEI

Tecnai Osiris S/TEM equipped with a field emission gun. In STEM mode, elemental maps were collected for 15 minutes, and the results were quantified using the Esprit software tools [24]. Line scan data across the Co/VDF interface was then obtained from these maps.

XPS spectra were acquired with a dual anode x-ray lamp and a hemispherical angle resolved electron analyzer (detector). The resolution of the detector, measured by the full width at half maximum (FWHM) of the F(1s) peak, was 2.5 eV. Spectra were calibrated against the Pt(4f) peak. Measurements were performed inside an ultra-high vacuum chamber, at a pressure of 1×10^{-10} Torr, to prevent impurity scattering events. The x-ray source used an Mg anode to produce Mg Kα radiation at 1253.6 eV. The sample was grounded during measurements to prevent charging effects [25]. Since photoemission is a surface sensitive technique, the depth dependence of the characteristic photoemission lines were measured by sputter etching the surface of the sample using an ionized argon (Ar^+) beam, at a pressure of 1×10^{-5} Torr, with cycle times ranging from five minutes to one hour. To maximize the uniformity of the reduced surface layer, the samples were rotated by ±40° with respect to the ion beam during each sputtering cycle. Spectra were collected immediately after each sputtering cycle, thereby enabling depth dependence measurements.

5.3 Results and Discussion

Co thin films readily oxidize when exposed to atmosphere [26-29] and in some instances this naturally forming oxide can be useful since CoO is antiferromagnetic. For example, the naturally formed antiferromagnetic oxide was used to investigate

perpendicular exchange bias in Co/Pt multilayer heterostructures [28]. Another study ingeniously exploited O^{2-} ion mobility in interfacial CoO_x to demonstrate voltage controlled magnetism via voltage-induced oxidation [30].

In general, however, devices with Co thin films require an architecture that limits exposure and prevents oxidation, as oxidation can cause exchange bias [31] in the device and will lead to thinner Co films causing a reduction in magnetization. A brief literature search reveals that the reported thickness and time dependence of oxide formation in Co thin films varies wildly. While the time dependence of oxidation appears to depend on both the thickness [27] and the previous oxidation state of the film [32], earlier work often offers contradictory conclusions. The canonical description, based on SQUID magnetometry studies of 15 Å thick Co films, assumes a self-protective layer of CoO, about 10 Å thick [28], formed from the topmost 6 – 7 Å of Co. However, another study used x-ray diffraction, Auger electron spectroscopy (AES), and magnetometry measurements to report that Co films with an initial thickness less than 25 Å will oxidize completely, and no metallic Co will remain, though the process may take months [27]. Still, other studies used AES and XPS to report that 8 – 10 Å of $Co(OH)_2$ forms instantaneously upon exposure [26, 29], with little additional oxide forming even after 1000 hours of exposure provided the film temperature is kept below 100 °C.

To clarify the time dependence of oxidation in ambient conditions, a series of polar MOKE (PMOKE) magnetic hysteresis loops (figure 5.1a) are measured as a function of time on an exposed, uncapped Co (1.2 nm) thin film. Starting at five minutes after removal from the vacuum chamber, loops were measured at approximately 10 minute intervals, with the last loop in the series taken 124 minutes after removal from

vacuum. Note that all loops are normalized to the saturation magnetization and therefore the loop heights are not to scale. The loops indicate a monotonic increase in the remanent magnetization, M_r, a signature of increasing perpendicular anisotropy (the time dependence will be discussed below). This is consistent with oxidation of the Co layer – as the film oxidizes, the Co thickness decreases proceeding through the spin reorientation transition thickness as shown in the inset. Previous reports on the spin reorientation transition thickness of Co thin films give values ranging from 1 nm [28] to 2 nm [33, 34]; here, it was found to be about 1 nm.

Capping the Co with a VDF oligomer thin film halts the process. Figure 5.1b shows PMOKE measurements from a Co (1.2 nm) thin film that was exposed to atmosphere for approximately 40 hours at room temperature, before being reinserted into the vacuum chamber for deposition of a 200 nm thick VDF oligomer thin film. Magnetic hysteresis loops taken in atmospheric conditions 14 minutes and again at 40 hours (2418 minutes) after exposure, but prior to deposition of the VDF oligomer layer, show increasing loop squareness similar to the exposed Co film corresponding to the loops shown in figure 5.1a. However, deposition of the VDF oligomer layer essentially locks in the magnetic properties of the Co thin film as there are no subsequent changes to the magnetic hysteresis loops, even after several days (2418-9906 minutes).

When the entire Co/VDF heterostructure is made without breaking vacuum, the magnetic properties of the Co thin film are stable with time. This is indicated in figure 5.1c, which shows PMOKE measurements from a Co (1.0 nm)/VDF thin film taken immediately after removal from vacuum (black) and after 24 days of atmospheric exposure (red), with no significant difference between the loops. Figures 5.1a-c establish

that thin films of VDF oligomer act as an effective barrier for Co thin films, "locking in" the magnetic properties of the Co even over long exposure times.

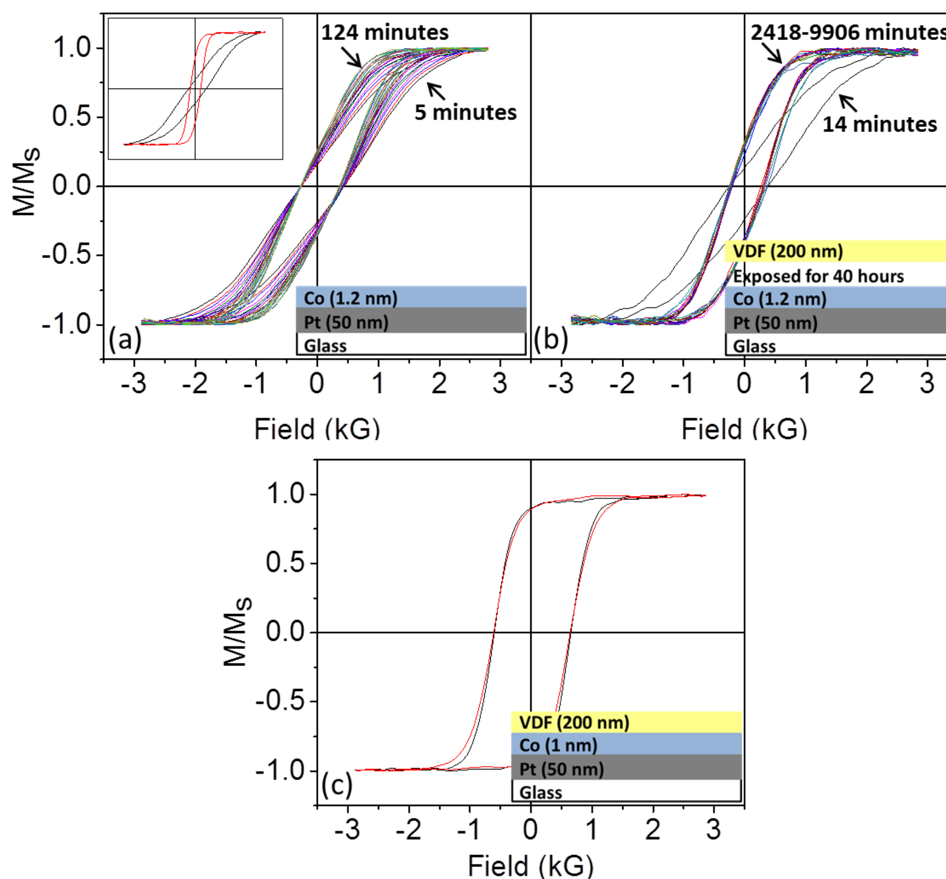

Figure 5.1: Time dependence of PMOKE magnetic hysteresis loops for the Co/VDF heterostructures shown in the insets. (a) 1.2 nm uncapped Co thin film, showing a continual change in the magnetic properties of the thin film from 5 minutes to 2 hours after removal from vacuum. Inset: Hysteresis loop after 5 minutes (black) and 5000 minutes (red) of exposure. (b) 1.2 nm Co thin film that was exposed to atmosphere for about 40 hours before being capped with VDF oligomer. The oligomer capping layer prevents further changes in the Co thin film, locking in its

magnetic properties. (c) Co/VDF heterostructure made without breaking vacuum, showing no significant differences between the first loop (black) and a loop taken 24 days later (red).

This data also sheds light on the time dependence of oxidation and subsequent anisotropy changes of Co thin films. Time dependent changes in the intensity of the Kerr signal ($\Delta I/I_{max}$) and the squareness (M_r/M_s) of the magnetic hysteresis loops for uncapped Co (1.2 nm) thin films and those with a VDF oligomer capping layer are plotted in figures 5.2a and 5.2b. Weighted exponential fits for the time dependence of the data corresponding to the uncapped Co thin films are shown in blue. The difference in Kerr signal intensity between up and down magnetic saturation for a given hysteresis loop (ΔI) normalized to the maximum intensity corresponding to a particular saturation state (I_{max}) is a measure of the quantity of ferromagnetic material [35]. Because MOKE does not measure the absolute magnetization, one cannot compare this quantity across samples. However, for a single sample, this is an acceptable measure of relative changes in the amount of ferromagnetic material. Both the decrease in Kerr signal and the increasing squareness of the uncapped film with time (figure 5.2b) are signatures of a decreasing thickness of ferromagnetic material [28, 33, 34].

Figures 5.2c and 5.2d show the weighted exponential fits from figures 5.2a and 5.2b on much longer time scales, with the fitting error represented by the red bands. A simple exponential function of the form $f(t) = a + be^{-t/\tau}$ produces the best fits, with both signatures saturating by ~10,000 minutes. From these fits, the time constants of the changes in magnetic hysteresis of uncapped Co thin films can be extracted: τ = 760

minutes for the decrease in $\Delta I/I_{max}$ (figure 5.2c), and τ = 910 minutes for the increase in M_r/M_s (figure 5.2d). However, PMOKE measurements performed on these same uncapped Co (1.2 nm) thin films taken a very long time after initial exposure show no ferromagnetic magnetic signature. Figure 5.2e shows such a measurement collected about 290,000 minutes (200 days) after initial exposure to atmosphere, at which time only the paramagnetic signature from the Pt seed layer is observed. Therefore, the applicability of the exponential fits to the time dependent changes of the magnetic hysteresis is carefully restricted to only the first several thousand minutes after initial exposure to atmosphere.

The difference in the time constants of $\Delta I/I_{max}$ and M_r/M_s can be explained by considering the relationship between the thickness of the film, d (which is proportional to $\Delta I/I_{max}$), and M_r/M_s. Under the assumption that irreversible magnetic domain losses are comparable for the in-plane and out-of-plane directions, the difference in area in the first quadrant of the in-plane and out-of-plane magnetic hysteresis curves gives the effective anisotropy energy, $K_{eff} = K_v + K_s/d$. This approach is commonly referred to as the "area method" [15, 36], and yields the equation for K_{eff} :

$$K_v + \frac{K_s}{d} = \frac{\mu_0}{2} M_s \left(H_c + \frac{M_r}{M_s} H_s \right) \tag{5.1}$$

where K_v and K_s are the volume and surface anisotropy energies, respectively, M_s and M_r are the saturation and remanent magnetizations, respectively, and H_c and H_s are the coercive and saturation fields, respectively. From equation 5.1, it is clear that d and M_r/M_s are not directly proportional, and so it is not expected that the time constants in figure 5.2 be identical. Rather, additional quantities on the right hand side of equation 5.1

may change with time, albeit very slowly. Figure 5.1a, for example, shows that H_c, though nearly constant, changes very slowly with time. The time dependence of additional quantities may reconcile the difference in time constants of $\Delta I/I_{max}$ and M_r/M_s.

From the data in figure 5.2, it is concluded that the oxidation process for these 1.2 nm thick exposed Co thin films occurs over the course of months, eventually leading to complete oxidation through the depth of the film. These results differ from those reported in references [26] and [28], but are in line with those reported in reference [27]. Moreover, these measurements definitively establish that a VDF oligomer thin film deposited on a Co thin film prevents oxidation, a crucial result with important implications for any future devices based on these ferroelectric/ferromagnetic heterostructures. It should also be noted that these slow changes in magnetic behavior could, for example, serve as a selector of magnetic properties, such as perpendicular anisotropy or remanence, by controlling the exposure time before capping with VDF oligomer as demonstrated in figure 5.1b.

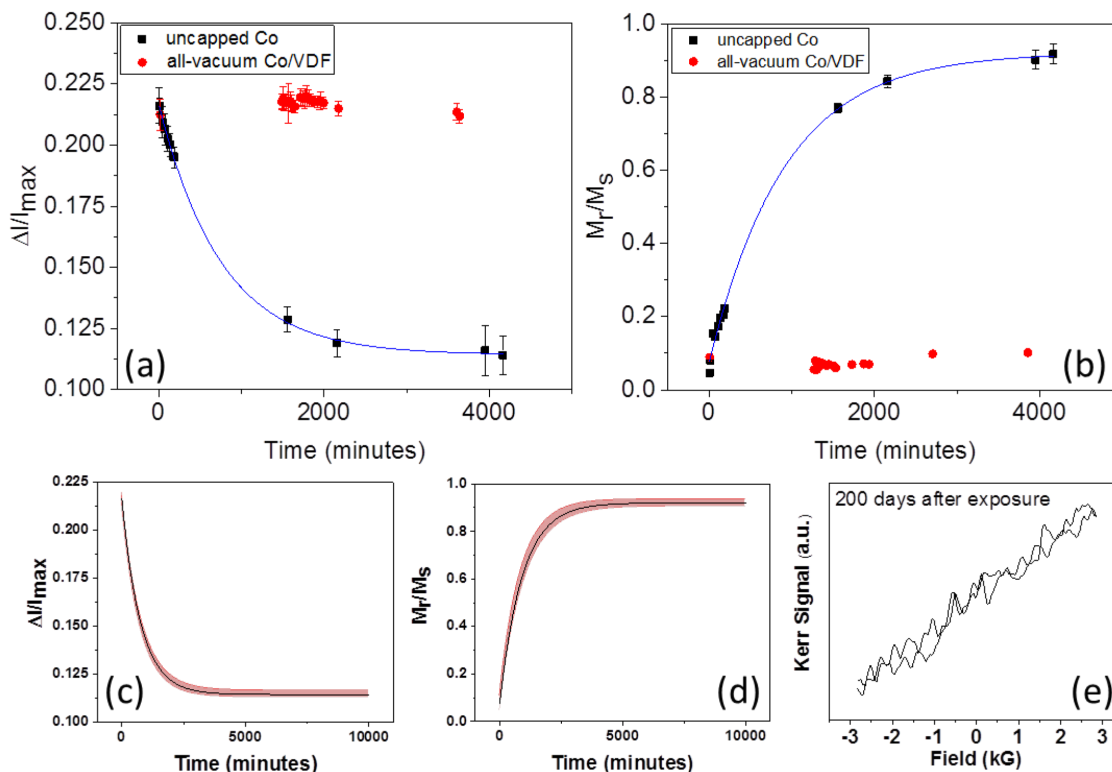

Figure 5.2: Magnetic signatures obtained from the hysteresis loops shown in figure 5.1. (a) Change in Kerr signal intensity ($\Delta I/I_{max}$) of magnetic hysteresis loops as a function of time for a 1.2 nm uncapped Co thin film (black) and an all-vacuum deposited Co/VDF heterostructure (red). (b) Squareness (M_r/M_s) of magnetic hysteresis loops as a function of time for a 1.2 nm uncapped Co thin film (black) and an all-vacuum deposited Co/VDF heterostructure (red). Weighted exponential fits are shown in blue. (c) and (d) show these fitted functions on much longer time scales, with the fit error represented by the red bands. (e) PMOKE measurements on the same 1.2 nm thick Co corresponding to the data in figure 5.1a after about 200 days exposure. These data clarify the time dependence of Co oxidation and clearly demonstrate the protective nature of the VDF

oligomer on Co thin films, which is extremely important for potential technological applications of these materials.

The thicknesses of these evaporated VDF oligomer thin films show the expected $1/r^2$ dependence [18] (where r is the distance from the source to the substrate), thus enabling an investigation of the thickness dependence of the VDF oligomer as a capping layer on a single large area sample. The contour map in figure 5.3 shows the thickness of a VDF oligomer thin film, measured with spectroscopic ellipsometry, across the full 4 cm^2 area of a Pt (50 nm)/Co (1.2 nm)/VDF heterostructure deposited without breaking vacuum. PMOKE measurements were taken in succession by cycling through the points labeled 1-5 on the contour map. One hysteresis loop was measured at each point during each cycle for a total of six cycles. Thus, a total of six hysteresis loops were collected periodically at each point during the first 500 minutes after the heterostructure was removed from vacuum. At all five locations, there is no change in the magnetic properties of the heterostructure during this time.

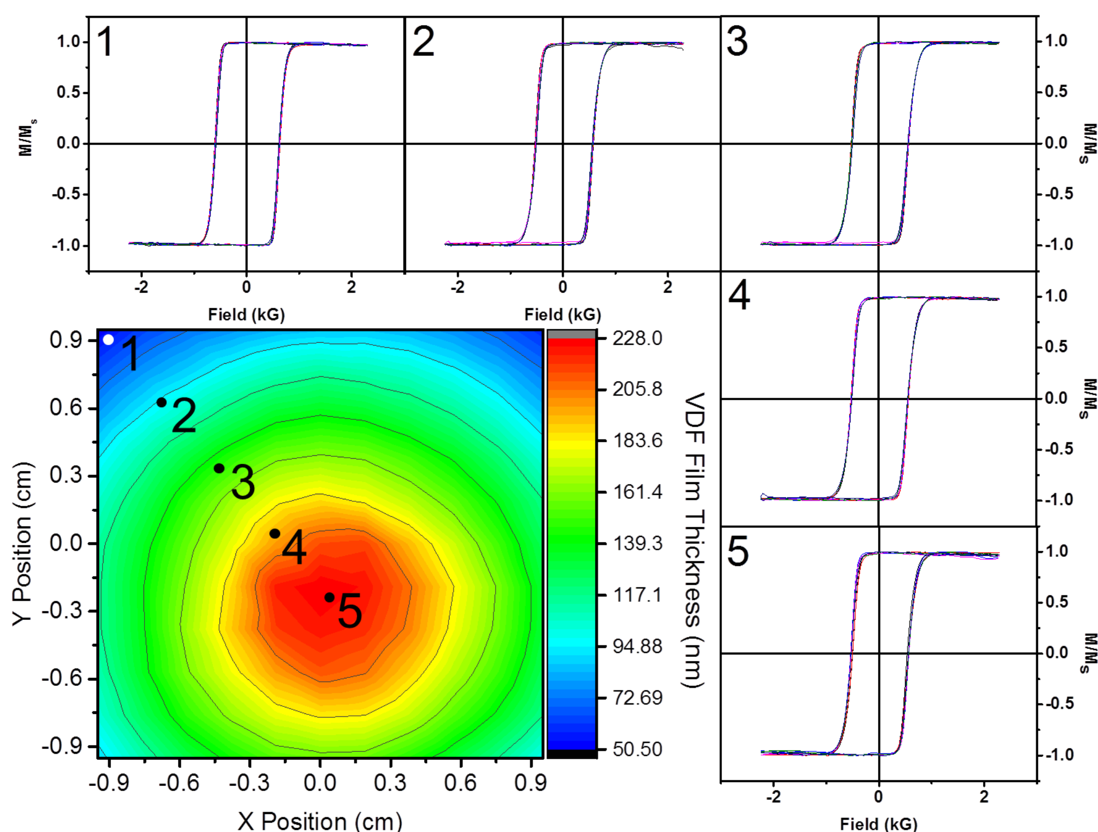

Figure 5.3: Thickness dependence of the VDF oligomer's ability to preserve the magnetic properties of a Co thin film. The magnetic hysteresis loops were collected in succession at the corresponding spots labeled on the thickness map. Each collection of hysteresis loops were taken over the first 500 minutes of exposure to atmosphere.

Similar MOKE and ellipsometry measurements across several separate Co/VDF heterostructures with progressively thinner VDF oligomer films indicate an oligomer film as thin as 15 nm is capable of preserving the magnetic properties of the Co thin film, as shown in figure 5.4. For VDF oligomer films with thicknesses less than 15 nm, the fitting of the ellipsometry data becomes unreliable, making it difficult to determine the actual

thickness of the film. Furthermore, the custom designed and built thermal evaporator lacks the precision of a commercial system, making it difficult to deposit ultrathin films. For these reasons, it is determined that at least 15-20 nm of VDF oligomer is needed to ensure reliable protection of the Co that can be reproduced from sample to sample. With advances in deposition techniques and sample characterization, however, the minimum VDF oligomer thickness to ensure the protection of Co may be found to be even lower.

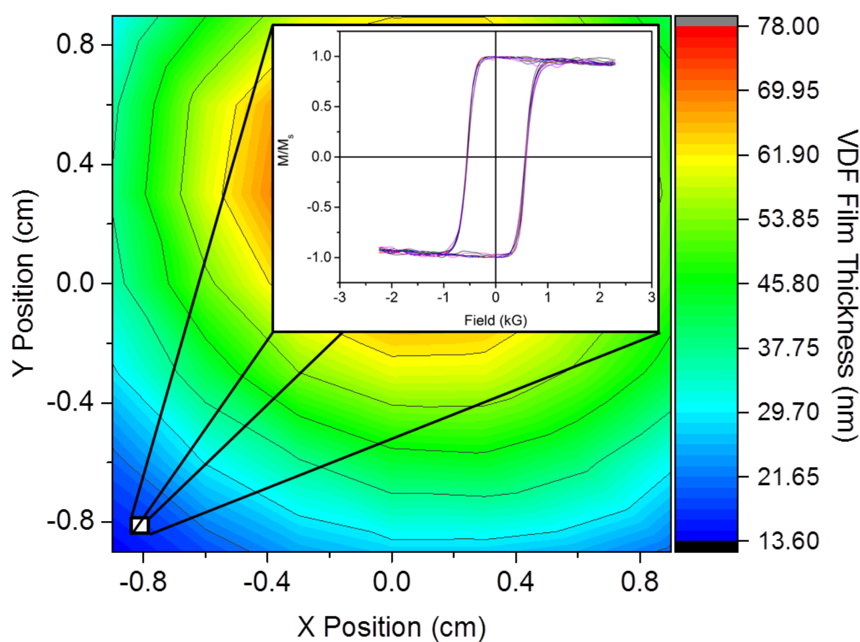

Figure 5.4: PMOKE as a function of time demonstrating that a VDF oligomer film as thin as 15 nm is capable of preserving the magnetic properties of the Co. The magnetic hysteresis loops were measured over a span of 500 minutes.

It is also important to consider the temperature dependence of the protective nature of the VDF oligomer thin films. Chapter 4 reported a detailed study on the

temperature dependence of VDF oligomer thin film properties and it was shown that the films begin to melt at 75 °C and are completely destroyed by 98 °C. X-ray diffraction measurements find only trace amounts of VDF oligomer remaining on the sample surface after heating to 98 °C, meaning that any Co underneath the VDF oligomer would no longer be protected from the atmosphere. It is important to note, however, that for device applications, heating to any temperature above the ferroelectric ordering temperature, which was found to be 61 °C, renders the VDF oligomer essentially useless, as it will be in the paraelectric phase. Thin VDF oligomer films remain structurally sound up to that temperature [18].

The magnetic hysteresis data shown in figures 5.1 and 5.2 clearly indicate changes in the Co thickness, but provide no information about the chemical or elemental nature of these changes. Scanning transmission electron microscopy (STEM) can be used to acquire high resolution images of the cross section of these heterostructures. However, STEM images alone show little detail of the Co/VDF interface (these images are shown in the insets of figure 5.5). Alternatively, STEM with energy dispersive spectroscopy (EDS) allows for the acquisition of elemental composition maps across the metal/organic interface. The line scan through a STEM map of a Pt (50 nm)/Co (1 nm)/VDF heterostructure prepared without breaking vacuum between the Co and VDF oligomer depositions (as in figure 5.1c) is shown in figure 5.5a. Only the elements of interest, Co and O, are shown in figure 5.5a. This line scan, across the Co/VDF interface, shows an abrupt and well-defined Co layer. Due to electron interactions with the sample, STEM mapping is known to exaggerate the thickness of thin film layers due to the interaction volume which increases with transmission depth [37]. Moreover, sample tilt within the

electron microscope can affect apparent film thickness. Therefore, although there appears to be a small region of overlap between Co and O at the top interface (gray band), this is likely due to their exaggerated thicknesses.

In contrast, figure 5.5b shows a line scan through a STEM map of a sample that was exposed to atmosphere for one week prior to the deposition of the VDF oligomer thin film. Here, even taking into account the exaggeration of the layer thicknesses, there is a region atop the Co layer with significant counts of both Co and O (yellow band). The increased total thickness of the Co film upon exposure to oxygen is consistent with previous reports [27]. These data, in conjunction with the magnetic hysteresis measurements, are consistent with oxide layer formation.

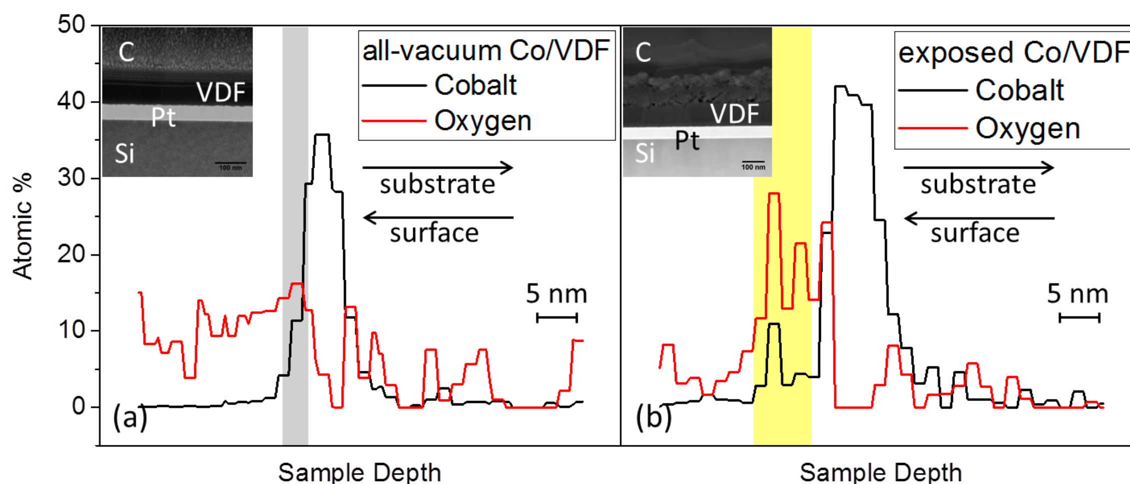

Figure 5.5: Line scans across the metal/organic interface from elemental composition maps of Co/VDF heterostructures acquired with STEM. (a) Co and O content at the Co layer in an all-vacuum deposited Co/VDF heterostructure. There is a region with overlapping Co and O counts due to volumetric interactions (gray band). (b) Co and O content at the Co layer

in a heterostructure that was exposed to atmosphere for one week prior to the deposition of a VDF oligomer capping layer. There is a region with significant counts of *both* Co and O (yellow band) atop the pure Co layer in (b) that is not present in (a), supporting the assumption that the changes in the magnetic properties of the Co thin films observed in figure 5.1 are due to the formation of native oxide. STEM maps are shown in the insets.

STEM measurements reveal the elemental composition at the metal/organic interface, but not the oxidation state. X-ray photoelectron spectroscopy (XPS) allows for a determination of the oxidation state by looking for changes in the binding energies of core electrons that occur due to chemical bonding. XPS spectra are acquired by irradiating a given sample with x-rays and measuring the kinetic energy of the resulting core level photoelectrons. Conservation of energy then gives the binding energy of the core level electrons while shifts in these binding energies indicate the formation of chemical bonds. Cross-referencing the XPS spectra collected from the metal/organic heterostructures with the online NIST database [38] identifies the element or compound corresponding to each observed photoelectron peak.

XPS measurements, together with periodic Ar^+ sputter etching of the sample surface, provide a depth profile of the chemical composition of Co/VDF heterostructures prepared with and without breaking vacuum during deposition. Figure 5.6a shows the XPS spectra in the region of the Co(2p) peak from a bare, uncapped Co thin film exposed to atmosphere for two weeks. At the surface of the film (black line), the peak positions correspond to oxide states of Co: the peak at 780 eV is attributed to CoO while the peak

at 796 eV could be attributed to CoO and/or Co_3O_4, as the binding energy of those compounds differ by only a few tenths of eV in this region. Deeper within the film (red line), the clear broadening of the peaks spanning 778 – 780 eV and 793 – 796 eV indicate the presence of both oxides and metallic Co. Pure metallic Co is only found near the Pt seed layer (blue line), as indicated by the narrower peaks at 778 eV and 793 eV. This is consistent with the PMOKE data shown in figure 5.2a, indicating a rapid decrease in magnetization of the uncapped Co thin film. The peaks at 786 eV and 802 eV in figure 5.6a are satellites caused by perturbations to the photo-emitted electrons due to the holes left in their place [25].

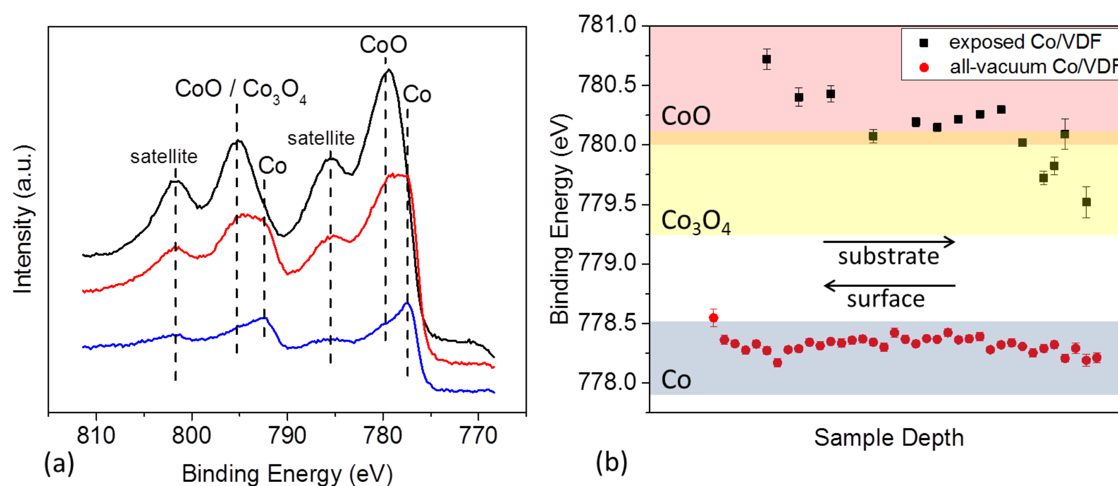

Figure 5.6: Co(2p) XPS spectra of Co/VDF heterostructures. (a) XPS spectra of a 1.2 nm uncapped Co thin film. At the surface (black line), the film is dominated by oxidized Co, while deeper in the film (red line), the broadening of the Co(2p) peaks indicate both oxidized Co and metallic Co. Only near the Pt seed layer (blue line), do the peaks correspond to metallic Co. (b) Depth profile of the XPS peak position for both exposed

Co/VDF and all-vacuum Co/VDF heterostructures, indicating that all-vacuum deposition prevents the Co from oxidizing. The colored bands indicate the positions of the peaks for CoO (pink), Co_3O_4 (yellow) and metallic Co (grey). Together, parts (a) and (b) show XPS spectra for all three samples types discussed: uncapped Co, exposed Co/VDF, and all-vacuum Co/VDF.

Figure 5.6b shows the location of the most prominent Co(2p3/2) peak, between 778 – 780 eV and determined via Gaussian peak fitting, for two samples, one a Co/VDF sample prepared entirely in vacuum and one that was exposed for several weeks prior to being capped with VDF oligomer. The left-most data points in figure 5.6b correspond to depths near the interface of the Co and VDF oligomer. Subsequent spectra collected after successive rounds of Ar^+ ion sputtering correspond to increased depths in the heterostructures and continued until the magnitude of the Pt peak stopped increasing, implying that the etch had reached the Co/Pt interface. Therefore, the data points on the right correspond to the bottom of the Co thin film. For the all-vacuum deposited sample, the location of the Co(2p) peaks stays constant throughout the depth of the sample, at about 778.3 eV, corresponding to pure metallic Co. However, for the sample that was exposed to atmosphere prior to capping with VDF oligomer, the location of the Co(2p) peak corresponds to that of oxidized Co, with the monoxide, CoO, dominating the bulk of the film, consistent with previous reports [26-29, 32]. Further details on the extraction of Co(2p) peak locations from the XPS spectra can be found in Appendix A. From figure

5.6b, it is clear that VDF oligomer preserves the Co thin film in its vacuum deposited state.

The bonding mechanism between the metal and organic thin films plays an important role in metal/organic heterostructures. For example, hybridization of the molecular orbitals at the interface is known to play a role in the energy level landscape, broadening and shifting the molecular energy levels at the interface [39, 40]. Furthermore, if the metal is ferromagnetic, this hybridization can be spin dependent [41], which has important implications for spintronic device applications utilizing metal/organic interfaces, as the interface plays an important role in spin lifetime and charge injection.

Because the metal/organic interface plays such an important role in any potential device, there have been many studies on the topic of metal/organic bonding [17, 42], with most falling into one of two categories: polymer on metal [43-45] or small molecule on metal [46-48] interfaces. Most studies on metal/organic interfaces employ either ultraviolet photoelectron spectroscopy (UPS) or XPS to probe binding energies at the interface. Small molecule films can be easily vacuum deposited on clean metal surfaces. Therefore, the metal/organic interface should be abrupt and well defined, with chemical bonding, if present, limited to the first molecular layer [17]. Polymer/metal interfaces present certain challenges when using the UPS/XPS technique, however, as defects along the polymer chain can affect photoemission: past studies have linked polymer morphology and photophysics by showing the chain length of certain conjugated polymers can affect exciton binding energy [17, 49, 50], whereas chain defects can

perturb forward scattered photoelectrons [51-53]. The reader is referred to reference [17] for an excellent review on polymer/metal and small molecule/metal interfaces.

Studies on oligomer/metal interfaces are less common than polymer/metal or small molecule/metal interfaces, and there are few, if any, UPS/XPS studies on Co/fluorinated oligomer interfaces to compare. Photoemission spectroscopy has, however, been used to probe the bonding mechanism at other metal/oligomer interfaces [54] and chemical bond formation at the interface of metallic Co and other organics, namely polybutadiene and polyimide, has been observed [44]. Hence, chemical bonds may form at the Co/VDF interface, and will be manifested as XPS peak shifts of either the Co(2p) and F(1s) peaks (or both), with the shift being characteristic of such metal/organic bonding [46]. For both types of heterostructures, those made entirely in vacuum and those that were exposed to atmosphere, there are no Co(2p) peaks at 782 – 783 eV, the binding energy corresponding to CoF compounds [38], at any depth in the heterostructures. Measurements of the F(1s) XPS peak location are shown in figure 5.7 as a function of VDF oligomer film depth for both all-vacuum and exposed Co/VDF heterostructures. The left-most data points correspond to spectra collected from the surface of the VDF oligomer thin film – the large shift in binding energy is attributed to surface contaminants – while the right-most data points correspond to the Co/VDF interface as inferred by the disappearance of the F(1s) peak (see Appendix A). Deeper in the film, the surface contaminants are no longer present, and the location of the F(1s) peak appears at 688.2 eV, the binding energy associated with the CH_2CF_2 monomer [38]. As the VDF is etched away, accessing deeper regions of the film, the peak shifts to slightly lower energies (by about 0.2 eV) at the interface between VDF and Co. Typical

metal fluoride peaks correspond to a much larger shift, occurring in the region of 684-685.5 eV, (i.e. shifts of 2.7-4.2 eV). This small shift may be due to bonding between the Co surface and other elements of the chain, resulting in a small shift in the F(1s) peak. For example, XPS measurements on Alq_3 on Mg show a 0.2-0.4eV shift in the Al line [46], which is attributed to Mg-C bonding [55].

Figure 5.7: F(1s) peak location as a function of VDF oligomer film depth for both exposed and all-vacuum deposited Co/VDF heterostructures. The large shift at the surface is attributed to surface contaminants. In both cases the location of the peak corresponds to the VDF monomer. Near the metallic Co substrate, the F(1s) peak shifts by 0.2 eV, which may suggest chemical bonding. The error bars represent the peak fitting error.

There is some evidence of chemical bonding at a metal interface (Al) in similar ferroelectric copolymers of VDF (70%) and trifluoroethylene (30%), P(VDF-TrFE) [56].

Like PVDF and its copolymers, the reversible ferroelectric polarization of the VDF oligomer film is associated with axial chain rotation, indicating that weak van der Waals forces dominate the bulk of the organic layer. In reference 56, Bune *et al* analyzed the static and dynamic conductance switching under DC bias of P(VDF-TrFE) films. The large contrast in conductance associated with the ferroelectric saturation states and a significant difference in the time needed to saturate to each conductance state, was modeled by assuming that the monolayer of P(VDF-TrFE) in direct contact with the metal electrode is pinned, unable to rotate and contribute to a saturated ferroelectric polarization state. The F(1s) XPS peak positions (figure 5.7) suggest that the VDF oligomer closest to the metal/organic interface is chemically bonded, providing experimental evidence corroborating the model proposed in reference 56.

The oligomer/metal interface is distinct from other organic/metal interface counterparts, namely small molecule/metal and polymer/metal interfaces. As mentioned above, polymer chain defects and local morphology can affect photoemission spectra. However, since the oligomer used in this study is made of short, well-defined chains, chain folding is unlikely and VDF oligomer thin films have improved crystallinity as compared to films made of the polymer (PVDF) [18]. Therefore, from the oligomeric nature of the chains, together with the size of the shift and the observation that the shift in binding energy only occurs near the metal interface, not throughout the bulk of the organic layer, it is concluded that this shift is not due to chain morphology, but may indeed be due to chemical bonding. Alternatively, it is possible that this small shift should be discounted, and that the Co/VDF interface bonding occurs purely via van der Waal forces.

5.4 Conclusions

In conclusion, the work in this chapter has characterized the interface between the organic ferroelectric VDF oligomer and metallic ferromagnetic Co. Using a combination of MOKE, electron microscopy and XPS, the time dependence of magnetization changes in exposed Co thin films has been definitively established and attributed to the formation of CoO. These changes occur over long periods of time, with time scales on the order of days and the naturally occurring CoO layer is not self-passivating. Thermally evaporated VDF oligomer films deposited on Co act as excellent protective barriers, even at thicknesses down to 15 nm, resulting in no changes in magnetic properties, little to no oxidation, and stability over a time period of at least a few weeks. XPS measurements of the F(1s) peak indicate the possibility of chemical bonding at the interface, but rule out CoF compounds. The ability of VDF thin films to "lock-in" magnetic properties could potentially serve as a mechanism for selecting desired magnetic properties, such as loop squareness, by simply timing Co exposure before depositing a capping layer.

Heterostructured Co/VDF devices are a promising candidate in the field of voltage controlled magnetism, making the characterization of the Co/VDF interface particularly important and the ability to maintain a pristine, controlled interface is imperative in understanding the magnetoelectric coupling in such a heterostructure. The work in this chapter demonstrates that the VDF oligomer is a viable candidate for use in organic-based electronics.

5.5 Acknowledgements

Financial support is provided by the National Science Foundation (NSF) through the Nebraska Materials Research Science and Engineering Center (MRSEC) Grant No. DMR-1420645 with additional support by NSF Grant No. ECCS-1101256. This research was performed in part in the Nebraska Nanoscale Facility: National Nanotechnology Coordinated Infrastructure and the Nebraska Center for Materials and Nanoscience (NCMN), which are supported by the NSF under Award ECCS-1542182, and the Nebraska Research Initiative.

5.6 References

1. C. W. Tang and S. A. Van Slyke, Appl. Phys. Lett. **51**, 913 (1987)
2. J. H. Burroughes, D. D. C. Bradley, A. R. Brown, R. N. Marks, K. Mackay, R. H. Friend, P. L. Burns, and A. B. Holmes, Nature **347**, 539 (1990)
3. N. Rehmann, D. Hertel, K. Meerholz, H. Becker, and S. Heun, Appl. Phys. Lett. **91**, 103507 (2007)
4. A. K. Ghosh and T. Feng, J. Appl. Phys. **44**, 2781 (1973)
5. A. K. Ghosh, D. L. Morel, T. Feng, R. F. Shaw, and C. A. Rowe, J. Appl. Phys. **45**, 230 (1974)
6. A. K. Ghosh and T. Feng, J. Appl. Phys. **49**, 5982 (1978)
7. R. F. Bailey-Salzman, B. P. Rand, and S. R. Forrest, Appl. Phys. Lett. **88**, 233502 (2006)
8. B. O'Connor, K. P. Pipe, and M. Shtein, Appl. Phys. Lett. **92**, 193306 (2008)

9. J. Song, H. Lu, K. Foreman, S. Li, L. Tan, S. Adenwalla, A. Gruverman and S. Ducharme, J. Mater. Chem. C, **4**, 5914 (2016)
10. I. Manunza, A. Sulis, and A. Bonfiglio, Appl. Phys. Lett. **89**, 143502 (2006)
11. M.-F. Chang, P.-T. Lee, S. P. McAllister, and A. Chin, Appl. Phys. Lett. **93**, 233302 (2008)
12. N. J. Watkins, G. P. Kushto, and A. J. Mäkinen, J. Appl. Phys. **104**, 013712 (2008)
13. R. Das and P. Harrop, *Printed, Organic & Flexible Electronics Forecasts, Players & Opportunities 2016-2026*, in: IDTechEx, 2015
14. P. V. Lukashev, T. R. Paudel, J. M. López-Encarnación, S. Adenwalla, E. Y. Tsymbal, and J. P. Velev, ACS Nano **6**, 9745 (2012)
15. A. Mardana, S. Ducharme, and S. Adenwalla, Nano Lett. **11**, 3862 (2011)
16. S. Zhang, Phys. Rev. Lett. **83**, 640 (1999)
17. J. Hwang, A. Wan, and A. Kahn, Mater. Sci. Eng. R-Rep. **64**, 1 (2009)
18. K. Foreman, N. Hong, C. Labedz, M. Shearer, S. Ducharme, and S. Adenwalla, J. Phys. D: Appl. Phys. **49**, 015301 (2016)
19. K. Foreman, C. Labedz, M. Shearer, and S. Adenwalla, Rev. Sci. Instrum. **85**, 043902 (2014)
20. Available through the J.A. Woollam Co., see https://www.jawoollam.com/ellipsometry-software/completeease for product details
21. S. Polisetty, J. Scheffler, S. Sahoo, Y. Wang, T. Mukherjee, X. Hi, and C. Binek, Rev. Sci. Instrum. **79**, 055107 (2008)

22. R. Hasegawa, M. Kobayashi, and H. Tadokoro, Polym. J. **3**, 591 (1972)

23. A. G. Chynoweth, J. Appl. Phys. **27**, 78 (1956)

24. Available through Bruker Corporation, see https://www.bruker.com/products/x-ray-diffraction-and-elemental-analysis/eds-wds-ebsd-sem-micro-xrf-and-sem-micro-ct/esprit-2 for product details

25. J. A. Colón Santana, *Quantitative Core Level Photoelectron Spectroscopy: A Primer* (Morgan and Claypool Publishers, California, 2015)

26. H. G. Tompkins and J. A. Augis, Oxid. Met. **16**, 355 (1981)

27. L. Smardz, U. Köbler, and W. Zinn, J. Appl. Phys. **71**, 5199 (1992)

28. S. Maat, K. Takano, S. S. Parkin, and E. E. Fullerton, Phys. Rev. Lett. **87**, 087202 (2001)

29. C. R. Brundle, T. J. Chuang, and D. W. Rice, Surf. Sci. **60**, 286 (1976)

30. C. Bi, Y. Liu, T. Newhouse-Illige, M. Xu, M. Rosales, J. W. Freeland, O. Mryasov, S. Zhang, S. G. E. tu Velthuis, and W. G. Wang, Phys. Rev. Lett. **113**, 267202 (2014)

31. W. H. Meikeljohn and C. P. Bean, Phys. Rev. **105**, 904 (1957)

32. X. Lin, G. C. Hadjipanayis, and S. I. Shah, J. Appl. Phys. **75**, 6676 (1994)

33. B. F. Miao, Y. T. Millev, L. Sun, B. Yun, W. Zhang, and H. F. Ding, Sci. China-Phys. Mech. Astron. **56**, 70 (2013)

34. M. Kisielewski, A. Maziewski, and V. Zablotskii, J. Magn. Magn. Mater. **316**, 277 (2007)

35. Z. Y. Liu and S. Adenwalla, J. Appl. Phys. **93**, 2091 (2003)

36. M. T. Johnson, P. J. H. Bloemen, F. J. A. den Broeder, and J. J. de Vries, Rep. Prog. Phys. **59**, 1409 (1996)
37. T. Volkenandt, E. Müller, and D. Gerthsen, Microsc. Microanal. **20**, 111 (2014)
38. NIST X-ray Photoelectron Spectroscopy Database, Version 4.1 (National Institute of Standards and Technology, Gaithersburg, 2012); http://srdata.nist.gov/xps/
39. H. Vázquez, R. Oszwaldowski, P. Pou, J. Ortega, R. Pérez, F. Flores, and A. Kahn, Europhys. Lett. **65**, 802 (2004)
40. M. L. Perrin, C. J. O. Verzijl, C. A. Martin, A. J. Shaikh, R. Eelkema, J. H. van Esch, J. M. van Ruitenbeek, J. M. Thijssen, H. S. J. van der Zant, and D. Dulić, Nat. Nanotechnol. **8**, 282 (2013)
41. M. Galbiati, S. Tatay, C. Barraud, A. V. Dediu, F. Petroff, R. Mattana, and P. Seneor, MRS Bulletin **39**, 602 (2014)
42. S. M. Barlow and R. Raval, Surf. Sci. Rep. **50**, 201 (2003)
43. P. S. Ho, P. O. Hahn, J. W. Bartha, G. W. Rubloff, F. K. LeGoues, and B. D. Silverman, J. Vac. Sci. Technol. A **3**, 739 (1985)
44. H. Leidheiser, Jr. and P. D. Deck, Science **241**, 1176 (1988)
45. F. Bebensee, M. Schmid, H.-P. Steinrück, C. T. Campbell, and J. M. Gottfried, J. Am. Chem. Soc. **132**, 12163 (2010)
46. C. Shen, A. Kahn, and J. Schwartz, J. Appl. Phys. **89**, 449 (2001)
47. C. Shen, A. Kahn, and J. Schwartz, J. Appl. Phys. **90**, 6236 (2001)
48. A. Kahn, N. Koch, and W. Gao, J. Polym. Sci., Polym. Phys. **41**, 2529 (2003)
49. E. M. Conwell, Synth. Met. **83**, 101 (1996)

50. A. J. Cadby, P. A. Lane, M. Wohlgenannt, C. An, Z. V. Vardeny, and D. D. C. Bradley, Synth. Met. **111**, 515 (2000)

51. W. F. Egelhoff, Jr., Phys. Rev. B **30**, 1052 (1984)

52. W. F. Egelhoff, Jr., J. Vac. Sci. Technol. A **2**, 350 (1984)

53. D.-Q. Yang, Y. Sun, and D.-A. Da, Appl. Surf. Sci. **144**, 451 (1999)

54. S. C. Veenstra, U. Stalmach, V. V. Krasnikov, G. Hadziioannou, H. T. Jonkman, A. Heeres, and G. A. Sawatzky, Appl. Phys. Lett. **76**, 2253 (2000)

55. C. Shen, I. G. Hill, A. Kahn, and J. Schwartz, J. Am. Chem. Soc. **122**, 5391 (2000)

56. A. Bune, S. Ducharme, V. Fridkin, L. Blinov, S. Palto, N. Petukhova, and S. Yudin, Appl. Phys. Lett. **67**, 3975 (1995)

CHAPTER 6

FERROELECTRICITY AND THE PHASE TRANSITION IN LARGE AREA EVAPORATED VINYLIDENE FLUORIDE OLIGOMER THIN FILMS

This chapter is based on the published paper: *Ferroelectricity and the Phase Transition in Large Area Evaporated Vinylidene Fluoride Oligomer Thin Films*, K. Foreman, S. Poddar, S. Ducharme, and S. Adenwalla, J. Appl. Phys. **121**, 194103 (2017). Reprinted with the permission of AIP Publishing.

6.1 Introduction

Organic molecules can be selected, or designed, to suit specific needs [1] leading to a rapid increase in both their use in fundamental physics and materials investigations, as well as in device applications. The latter includes organic light emitting diode (OLED) displays [2-4], flexible electronics [5-7], and even potential applications using voltage-controlled magnetic anisotropy [8-10]. Organic ferroelectric materials effectively combine the customizability afforded by organic synthesis with the useful electro-physical behaviors of ferroelectric materials, applications of which range from piezoelectric transducers [11] to data storage [5, 12, 13]. The well-known polymer ferroelectric poly(vinylidene fluoride) (PVDF) [14] and its copolymers with trifluoroethylene (TrFE) have several properties that make them well-suited for various applications, including a low stiffness coefficient [15] and a high remanent polarization [16]. As with other organic materials, P(VDF-TrFE) can also be customized to suit

specific applications. For example, the transition temperature may be modified by tuning the ratio of VDF to TrFE [17].

This chapter reports an investigation of ferroelectricity in a promising organic material, the VDF oligomer. Obtaining definitive experimental evidence of ferroelectricity in new materials is an intricate process, since non-ferroelectric materials may mimic ferroelectric signatures [18]. For example, charge injection in an electret can result in ferroelectric-like hysteresis loops, with very long relaxation times. This work confirms the existence of ferroelectricity using a variety of measurements. More importantly, however, this work presents compelling evidence of the existence of the ferroelectric-to-paraelectric phase transition, which has not been previously identified in VDF oligomer crystals.

The VDF oligomer shares the same molecular and crystal structure as the polymer counterpart, PVDF [17, 19, 20]. This similarity, in turn, may explain the similar ferroelectric properties of the VDF oligomer and the polymer. However, the VDF oligomer holds a crucial advantage over the polymer: VDF oligomer thin films can be deposited in vacuum. Unlike PVDF, which is commonly deposited in ambient conditions using Langmuir-Blodgett deposition [21] or spin coating [22], vacuum deposition of the VDF oligomer preserves the cleanliness of the interface between the organic and adjacent layers [23], an essential need for spintronics and other devices. Earlier work [23-25] (Chapters 3-5) has established the conditions for optimal growth via thermal evaporation, investigated the physical properties of these thermally evaporated VDF oligomer thin films and established that these thin films both protect and are chemically inert with an underlying metal thin film, thereby preserving the interface.

Because of the potential device applications of VDF oligomer thin films, this work also investigates those properties relevant to devices, including the working temperature range and remanent polarization, the reliability and reproducibility of switching, and the time dependence of the remanent polarization. The latter is especially important for non-volatile memory applications. This work establishes the working temperature of VDF oligomer thin films and provides evidence for the existence of the ferroelectric-to-paraelectric phase transition using a combination of differential scanning calorimetry along with pyroelectric and capacitance measurements as a function of substrate temperature. Measurements of the dependence of capacitance on bias voltage elucidate the ferroelectric nature of the VDF oligomer and demonstrate the repeatability of polarization switching in these films. The loss tangent of VDF oligomer films is recorded as a function of voltage, revealing these films maintain low ac dielectric loss even during polarization reversal. Current-voltage measurements (I-V) are used to calculate the spontaneous polarization of these VDF oligomer films. Moreover, the capacitance, loss tangent, and I-V measurements were recorded from VDF oligomer films with areas over 2 mm^2, showing that high-quality films can be produced on scales suitable for devices. X-ray diffraction (XRD) measurements are used to assess the ferroelectric structure of as-grown VDF oligomer thin films. Measurements of the zero-field pyroelectric signal as a function of time indicate a stable, long-lived remanent polarization, a crucial result for device applications. Finally, using piezoresponse force microscopy (PFM), large area ferroelectric domain writing is demonstrated, opening the way to possible memory applications.

6.2 Sample Preparation and Experimental Methods

Samples were prepared in several configurations to suit particular measurements. Specific sample structures are listed below with each corresponding measurement, and the sample architectures are shown in the insets of the accompanying figures. Substrates were either glass slides or Si wafers. For samples requiring a bottom metallic electrode, Pt thin films (30 – 50 nm) were deposited at a rate of 0.5 Å/s in a magnetron sputtering deposition chamber with a base pressure of 1×10^{-8} Torr. For samples not requiring metallic electrodes, the VDF oligomer was deposited directly onto the substrate. The VDF oligomer thin films were deposited in a custom thermal evaporation chamber connected to the sputtering chamber via a gate valve [24]. The substrate temperature was maintained at 130 K during the deposition to ensure that the VDF oligomer chain conformation was in the desired ferroelectric β-phase [26]. The VDF oligomer was deposited at a rate of 1 Å/s, as confirmed by ellipsometry measurements [25]. The VDF oligomer powder, $CF_3\text{-}(CH_2CF_2)_n\text{-}I$, was provided by Kunshan Hisense Electronic Co., Ltd. and has a chain length of $n = 15 \pm 2$ as confirmed by nuclear magnetic resonance measurements. For samples requiring a top electrode, 30-nm thick Al films were deposited at a rate of 2 Å/s from a thermal evaporator at a pressure of 3.75×10^{-5} Torr. Thermal evaporation was used to deposit top metal electrodes, as sputtering was found to be unsuitable due to the highly energetic sputtered atoms which puncture the soft organic film, resulting in electrically shorted top and bottom electrodes.

The absorption and release of latent heat of a ferroelectric being driven through its phase transition is manifested as peaks in heat flow vs. temperature measurements using differential scanning calorimetry. VDF oligomer powder was loaded into an alumina pan

of a NETZSCH Model 204 F1 Phoenix calorimeter, sealed, and placed in the calorimetry chamber along with an empty reference alumina pan. The calorimetry chamber was purged with argon gas to avoid contamination and the heating/cooling rate was maintained at 2 °C/minute.

The pyroelectric current, which is proportional to the spontaneous polarization [27, 28], was measured using the Chynoweth method [29] (described in more detail in the following section), with a 1-mW, 658-nm wavelength diode laser modulated with an optical chopper at a frequency of 2 kHz. A thermoelectric heater was integrated into the experimental setup so that the pyroelectric current could be measured as a function of sample temperature. XRD measurements were performed using a Rigaku D/Max-B Diffractometer in θ-2θ mode with Co Kα radiation of wavelength 1.789 Å.

The dependence of the capacitance and loss tangent on voltage (C-V) were measured using a programmable HP 4192A LF impedance analyzer with an ac test signal of 0.1 V at 1.0 kHz. A LabVIEW-controlled thermoelectric heater was used to heat the sample in order to measure the capacitance as a function of temperature. The static I-V characteristic curves were measured for the VDF oligomer capacitors using a LabVIEW-controlled Keithley Model 2400 source meter. From the I-V curve, the value of the remanent polarization can be calculated [20]. High-resolution optical microscopy images along with ImageJ software [30] were used to measure the electrode area for these calculations.

Local domain imaging of ferroelectric VDF oligomer thin films was performed by PFM using a Bruker Dimension Icon atomic force microscope in piezoresponse mode, which is optimal for visualizing and manipulating vertical, out-of-plane domains. For

these studies, a 30-nm layer of Pt was sputtered onto a Si substrate, followed by the deposition of a VDF oligomer thin film. A conductive Pt-Ir coated PFM tip (Bruker model SCM-PIC-V2) with a nominal spring constant of 0.1 N/m was used for reading and writing ferroelectric domains. The soft organic films are bound by weak van der Waals forces [1, 23], necessitating the relatively soft PFM tip to ensure there are no topographical changes in the surface of the soft film during PFM measurements without compromising the piezoresponse signal. An ac voltage at a frequency of 45 kHz is applied between the tip and sample during domain reading/mapping. The writing of rectangular domains is accomplished by scanning the film surface with a dc bias up to ±10 V applied between the tip and the sample. In both cases, the platinum-coated silicon substrate acts as the ground.

6.3 Results and Discussion

Although the observation of bi-stable polarization hysteresis adequately defines ferroelectricity, study of the ferroelectric-to-paraelectric phase transition is central to the confirmation of the ferroelectric nature of a material, and great effort has been invested in establishing this transition in VDF-based copolymers [14, 31-33]. In addition, the operating temperature range is a key parameter for any candidate organic material for use in organic electronic devices. This work measures the relevant temperature ranges of both the VDF oligomer source powder and the thin films using three difference methods. Because first-order phase transitions are highly sensitive to the rate of change of temperature, care was taken to steadily increase the temperature by 2 °C/min in all three cases.

The heat flow per unit mass upon heating and cooling was collected via calorimetry for two consecutive cycles from bulk powder VDF oligomer. The measured heat flow (figure 6.1a) shows a broad peak upon heating with the onset around 60 °C and a maximum at 79 ± 5.5 °C. This peak indicates that the VDF oligomer undergoes a ferroelectric-to-paraelectric phase transition at 79 ± 5.5 °C in the bulk, followed by a melting peak at 110 ± 2 °C. Upon cooling, the crystallization peak from the melt occurs at 100 ± 1.5 °C and the paraelectric-to-ferroelectric phase transition occurs at 45 ± 1.5 °C.

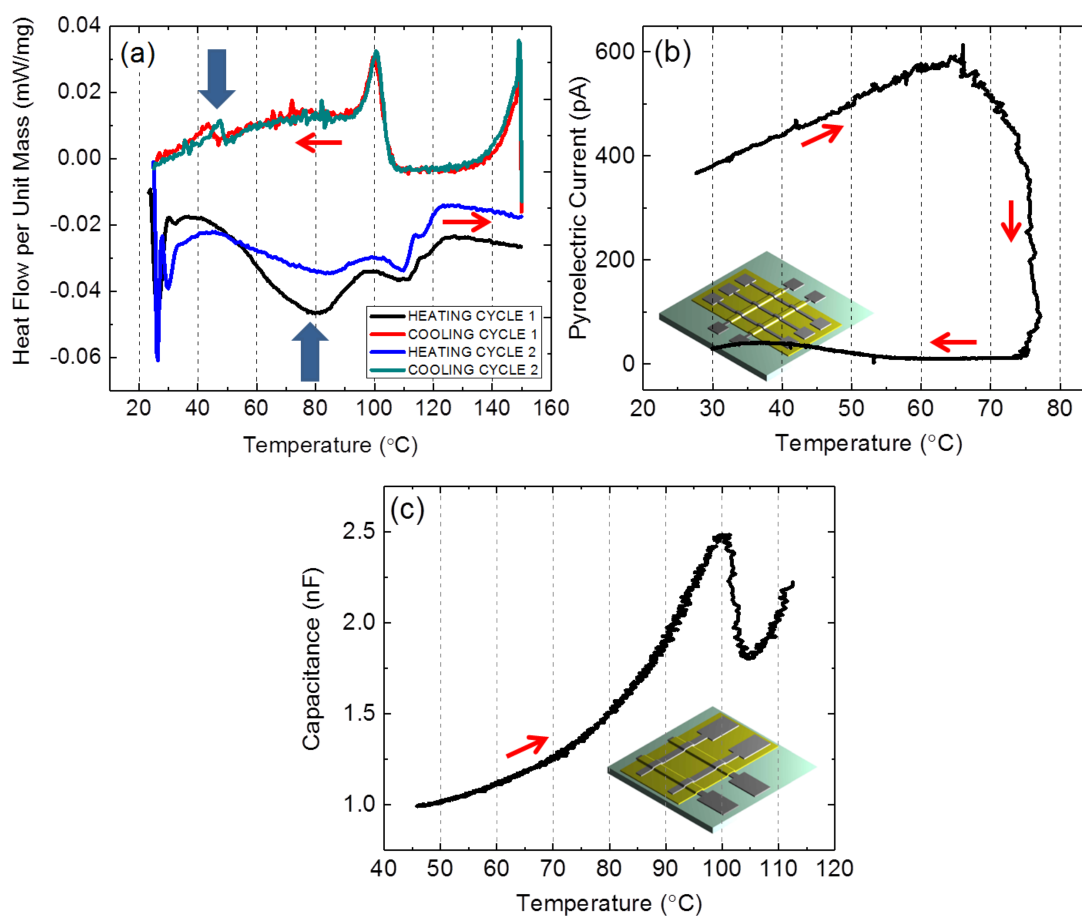

Figure 6.1: (a) Heating (black and blue) and cooling (red and cyan) calorimetry measurements. The phase transitions are marked with blue arrows. (b) Pyroelectric current as a function of substrate temperature

from a 100-nm thick VDF oligomer film. (c) Capacitance as a function of substrate temperature from a 200-nm thick VDF oligomer film. The red arrows in parts (a)-(c) indicate the direction of the curves, while the insets in parts (b) and (c) show the sample architecture for each measurement (the yellow layer is the VDF oligomer film).

Figure 6.1b shows the dependence of the pyroelectric current on substrate temperature measured for a glass/Pt (40 nm)/VDF (100 nm)/Al (30 nm) heterostructure with an electrode area of 200 × 200 μm^2. The ferroelectric polarization was first saturated by applying incrementally increasing voltages across the film. Once the polarization was saturated, the pyroelectric current was recorded (using the Chynoweth method [29]) as a function of substrate temperature upon heating. Consistent with previous measurements [25, 27], the pyroelectric current increases with temperature and is a maximum at the proposed phase transition temperature [28]. Upon cooling, the pyroelectric current was only 10% of the original saturated, room temperature value, indicating depolarization of the VDF oligomer film upon heating and is consistent with the expected behavior associated with heating above the phase transition temperature. From the pyroelectric measurement (figure 6.1b), the ferroelectric-to-paraelectric phase transition temperature of the VDF thin film is found to be 65 ± 1 °C on heating, 14 °C lower than the value found in the calorimetry measurements (figure 6.1a). Understanding this difference may require a detailed comparative study of the thermo-kinetics of the phase transformations in these systems in both thin film and bulk form.

Further evidence for the existence of the phase transition is given in figure 6.1c, which shows the capacitance as a function of substrate temperature measured on a glass/Pt (30 nm)/VDF (200 nm)/Al (30 nm) heterostructure with an electrode area of 1.5 × 1.5 mm^2. The capacitance, which depends on the dielectric constant of the VDF oligomer, shows a clear peak at 100 ± 1 °C, indicating a phase transition. The 35 °C difference in transition temperature of the films (figures 6.1b and 6.1c) is similar to that previously noted in P(VDF-TrFE) thin films [34], in which pyroelectric and dielectric constant measurements upon heating indicated transition temperatures of 78 °C and 110 °C, respectively. The dielectric constant exhibits thermal hysteresis during a first-order phase transition, thus the capacitance peaks at a higher temperature upon heating than upon cooling [34].

The C-V and I-V curves shown in figure 6.2 were measured on a glass/Pt (30 nm)/VDF (200 nm)/Al (30 nm) heterostructure with electrode areas of 1.5 × 1.5 mm^2. Figure 6.2a shows C-V loops for three consecutive cycles. The C-V loops show the characteristic butterfly shape indicative of ferroelectricity and the reproducibility of these C-V loops over three cycles reflects the stability of ferroelectric properties in these VDF oligomer thin films. Figure 6.2b shows the loss tangent as a function of bias voltage for the same sample, collected simultaneously with the capacitance loops shown in figure 6.2a. The value of the loss tangent for these thermally evaporated films is comparable to solution-cast PVDF films (0.06) [35] and cluster synthesized VDF oligomer films (0.07) [36] at the same frequency used here (1 kHz). When the ferroelectric polarization is saturated, the loss tangent is about 0.07-0.08, and remains less than 0.11 even during polarization reversal. This low value indicates that thermally evaporated VDF oligomer

has a relatively low dielectric loss, and is suitable for capacitor devices. Furthermore, the low dielectric loss of these VDF oligomer thin films is a strong indicator of the insulating nature of these films even across the fairly large area of 1.5×1.5 mm^2.

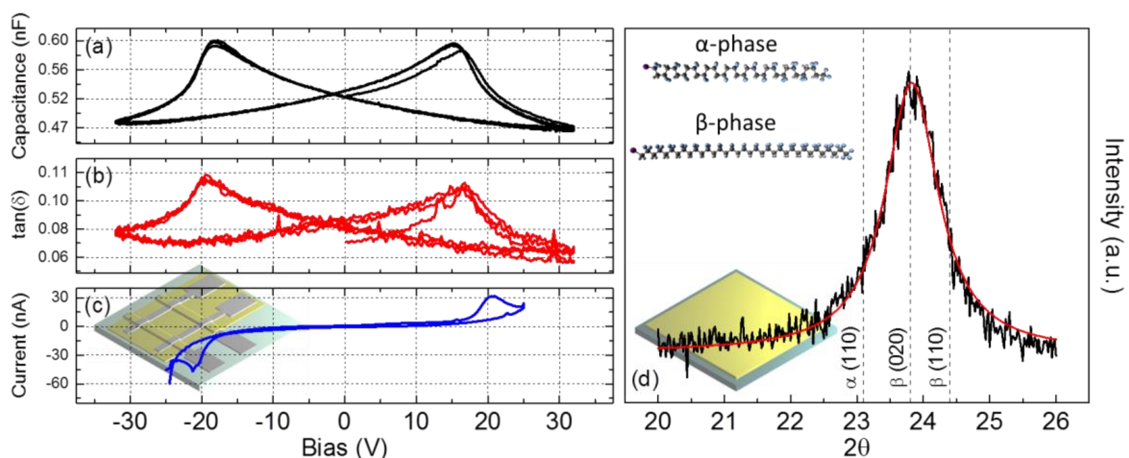

Figure 6.2: (a) Capacitance and (b) loss tangent for three consecutive voltage loops, demonstrating the characteristic butterfly loops of ferroelectric materials, for a 200-nm thick VDF oligomer film. (c) Current as a function of voltage for a 200-nm thick VDF oligomer film. The inset in part (c) shows the sample architecture for the measurements in parts (a)-(c). (d) Background corrected XRD peak of an as-deposited VDF oligomer thin film (fit in red). The upper insets show illustrations of the α-phase and β-phase chain conformations, while the lower inset shows the sample architecture for the measurement.

A typical I-V measurement from these heterostructures is shown in figure 6.2c. At higher voltages there is a nonlinear background due to conduction across the VDF oligomer. However, around ±21 V a peak in the measured current can be seen and is due to the polarization reversal associated with axial rotation of the VDF oligomer chains.

The voltage was swept at a constant rate of 0.25 V/s. The time integral of the switching current, after correcting for the leakage current, divided by the area of the electrode yields a value of twice the remanent polarization [20], and so from figure 6.2c, the remanent polarization is calculated to be 104 ± 2 mC/m^2. This value is less than the reported value of 130 mC/m^2 by Noda *et al*. [20], but higher than the remanent polarization of PVDF (60 mC/m^2) [16] and comparable to P(VDF-TrFE) (100 mC/m^2) [37]. Though the value for remanent polarization found here is lower than that reported in reference 20, it should be noted that the chain length of the VDF oligomer in that study differs from that used here. Past studies have shown that the chain length can affect the crystal structure of VDF oligomer thin films [38], which in turn can affect the measured polarization.

While C-V and I-V loops demonstrate the switchable polarization of the thin films, XRD can be used to determine the chain conformation and dipole orientation of these thermally evaporated, large area VDF oligomer films. Figure 6.2d shows the XRD peak of a 100 nm thick VDF oligomer film deposited on a Si wafer. A Lorentz peak fit indicates a peak location of 23.81°, clearly indicating that the dominant crystalline orientation and chain conformation of the as-grown VDF oligomer film is the (020) orientation of the β-phase, ideal for device applications, with the maximum ferroelectric polarization perpendicular to the sample plane [25]. In contrast, the dipole moments of the (110) orientation of the β-phase (which is the usual orientation for Langmuir-Blodgett deposited films of P(VDF-TrFE) [5, 39] are canted 30° away from the surface normal, resulting in a 13.4% decrease in the out-of-plane component of ferroelectric polarization. Langmuir-Blodgett deposition of β-phase VDF oligomer result in films with the carbon chains normal to the substrate, such that the dipole moments are oriented in the plane of

the film [40, 41], an orientation that is both difficult to measure and less useful in device applications.

The hysteretic behavior in figures 6.2a-c and the location of the diffraction peak in figure 6.2d demonstrate the consistently switchable polarization and optimal crystalline orientation of the as-grown VDF oligomer, respectively. Moreover, the large electrode areas of 2.25 mm^2 compare very favorably with those needed by organic-based electronic devices, such as an OLED pixel (on the order of μm^2) or a ferroelectric RAM bit (on the order of nm^2) and indicate that the films can be deposited in large, defect free areas suitable for device production.

An additional measure of the suitability of ferroelectrics for use in non-volatile devices is the long term stability of the ferroelectric polarization in the absence of an electric field. Figure 6.3a shows a typical pyroelectric hysteresis loop collected via the Chynoweth method from a glass/Pt (50 nm)/Co (1 nm)/VDF (175 nm)/Al (30 nm) heterostructure with an electrode area of 200×200 μm^2. The red arrows indicate the path of the hysteresis. At a constant temperature, the pyroelectric current is directly proportional to the ferroelectric polarization of the VDF oligomer thin film, thus a saturated pyroelectric current is equivalent to complete polarization. The initial measured pyroelectric current, prior to the application of an external voltage, is 5 pA, less than 1% of the saturation current of 650 pA. Additional hysteresis loops collected from other metal/oligomer heterostructures repeatedly show this small initial pyroelectric current, ranging from 1% to 10% of the saturation current, indicating that the net polarization of as-grown, unpoled VDF oligomer thin films is low.

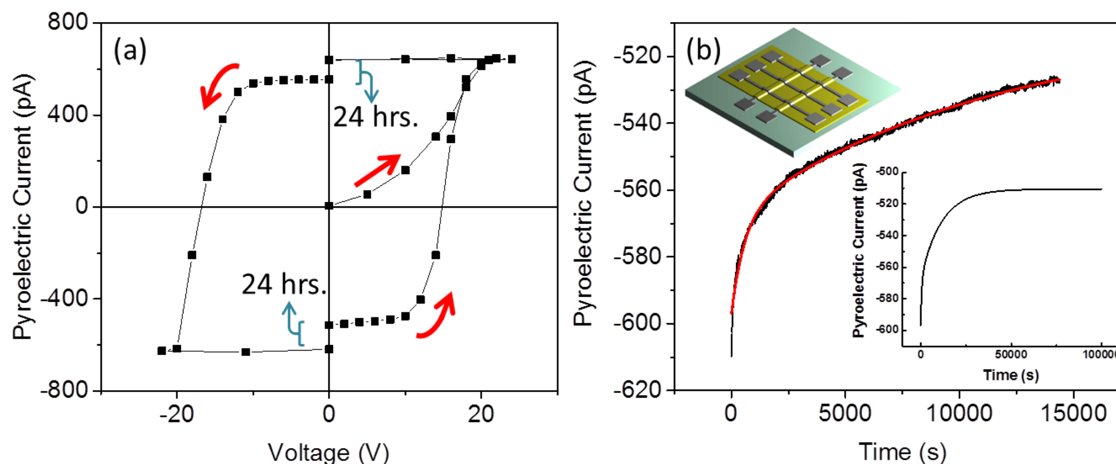

Figure 6.3: (a) Hysteresis in the pyroelectric response from a 175-nm thick VDF oligomer film. The film was left for 24 hours at each remanent state. The red arrows indicate the direction of the hysteresis loop. (b) Pyroelectric current as a function of time at the negative remanent state (i.e., at zero voltage). An exponential fit is shown in red. The lower inset shows the fitted function on the scale of 24 hours. The upper inset shows the sample architecture for these measurements.

The process of obtaining the hysteresis loop shown in figure 6.3a was as follows. The polarization state was prepared by applying a constant voltage held across the VDF oligomer thin film for five minutes, after which the voltage is disconnected and the current is measured for several seconds using a lock-in amplifier with a time constant of 300 ms. Once the pyroelectric current is recorded, the next incremental voltage is applied and the process continues until the entire hysteresis loop is obtained [29, 42]. For the loop shown, the exception to this procedure occurs at the positive and negative remanent polarization states. At these locations along the hysteresis loop, the pyroelectric current was recorded shortly after the application of voltage as usual. The sample was then left in

the remanent state, with no applied voltage, for 24 hours, after which the pyroelectric current was recorded again and collection of the hysteresis loop proceeded once more. The pyroelectric signal decayed by 13% (17%) after 24 hours at the positive (negative) remanent saturation state. The decay is interpreted as a gradual relaxation of the VDF oligomer chains back towards the as-grown low net polarization state, decreasing the net ferroelectric polarization perpendicular to the metal electrodes. Since the as-grown VDF oligomer film is predominantly in the (020) orientation (figure 6.2d), this zero-field decay is most likely due to the film breaking up into up and down domains.

Use in a non-volatile device makes it imperative that the VDF oligomer film retain a non-zero remanent polarization. Polarization relaxation in Langmuir-Blodgett films of P(VDF-TrFE) has been studied by monitoring the pyroelectric current as a function of time [43], and the same approach is used here. The time dependence of the pyroelectric current over a period of over four hours was measured and is shown in figure 6.3b, where t = 0 s corresponds to the current immediately after reaching the negative remanent polarization state. The red line is an exponential fit to the decaying pyroelectric signal. From the fit, the decaying signal is found to have a time constant of 6700 s. The inset of figure 6.3b shows the fitted function on a much longer time scale of about 24 hours. The fit shows very little additional decay after 12 hours, indicating that the small jump in the hysteresis loop shown in figure 6.3a represents most of the polarization decay at the remanent states. Extrapolation to 48 hours shows an additional decay of less than 1%. Indeed, a non-zero pyroelectric current can be measured on samples after having been left in the remanent polarization state for several months. From these data, it is concluded that even after an extended period of time, a significant portion of the

remanent polarization signal remains, in this case about 85%, and nearly all of the decay occurs within the first 12 hours. This non-zero, stable remanent polarization is a necessary condition for any potential non-volatile device applications.

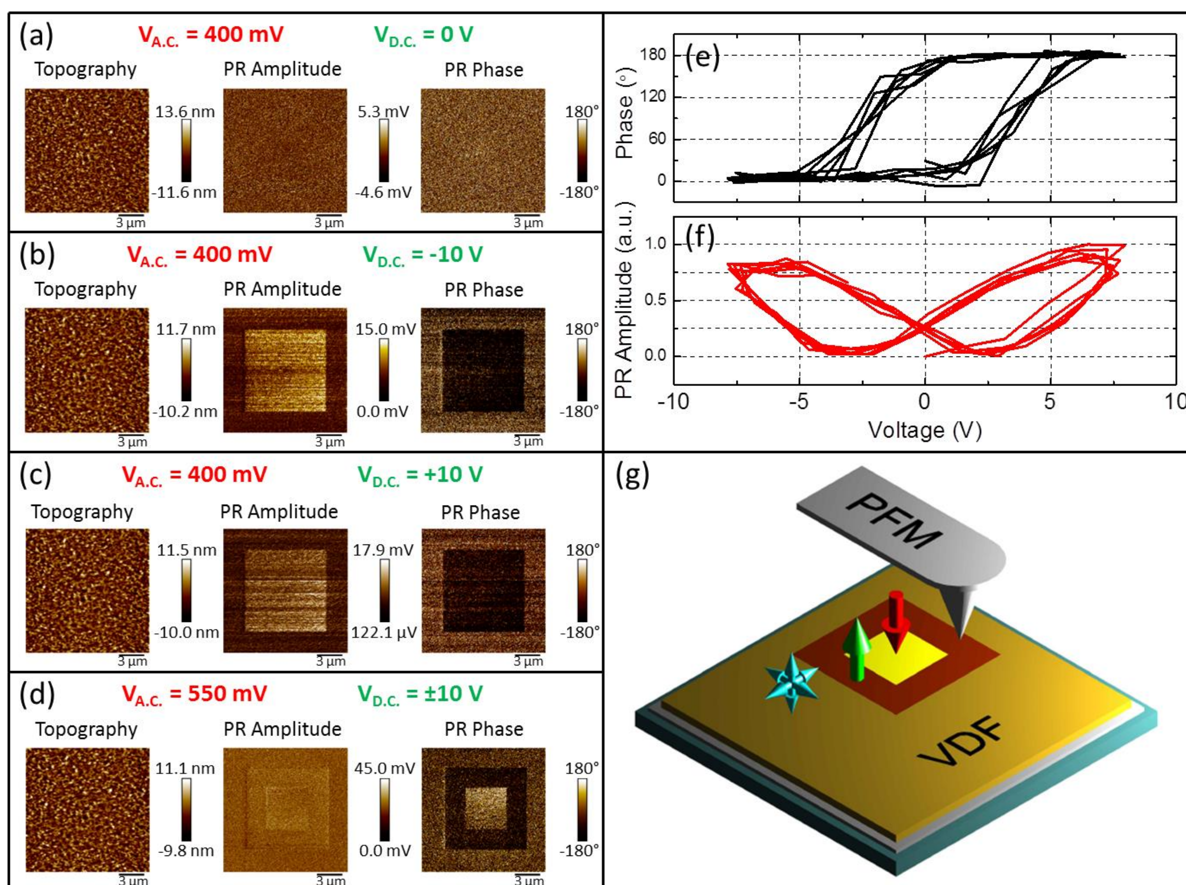

Figure 6.4: (a)-(d) PFM measurements of topography (left), piezoelectric response (PR) amplitude (center), and PR phase (right) from VDF oligomer thin films under various ac (red) and dc (green) bias conditions. All scale bars are 3.0 µm. Local (e) PR phase and (f) PR amplitude demonstrating clear hysteretic behavior. (g) An illustration of ferroelectric domain writing with a PFM tip, as demonstrated in part (d). The ferroelectric polarization of the poled VDF oligomer is represented by the

red and green arrows, while the blue arrows represent the unpolarized, as-grown VDF oligomer.

Figure 6.4 shows PFM measurements with a spatial resolution of 30 nm collected on various Si/Pt (30 nm)/VDF (50 nm) samples. The Si/Pt substrate serves as a bottom electrode, while the PFM tip itself serves as the top electrode, through which voltages are applied across the VDF oligomer thin film. Initially, a 12 μm × 12 μm area was imaged with ac voltage (V_{dc} = 0 V) to detect any as-grown domains (figure 6.4a). No domain structures were visible, indicating that the as-grown VDF oligomer films are nominally unpoled at the scale of the instrument resolution, in agreement with the low pyroelectric current of the as-grown film shown in figure 6.3a. To demonstrate domain reading/writing, a square domain of 8 μm × 8 μm within the same region imaged in figure 6.4a was written by applying a -10 V bias across the VDF oligomer thin film (figure 6.4b). After writing, the created domains were read via ac voltage with the dc bias off, revealing an increase in the piezoresponse amplitude in the poled area as well as a sharp phase contrast. A similar poling process albeit with +10 V across the VDF oligomer thin film in the same region yields similar results as shown in figure 6.4c. The choice of the dc writing voltage of ±10 V was based on past work [25] indicating that the average coercive field of these VDF oligomer thin films is 95 MV/m. Hence, a bias of ±10 V is sufficient to saturate the polarization in the 50 nm thick VDF oligomer film, which should have a switching voltage of about ±5 V.

In order to compare the piezoresponse amplitude of the positively and negatively poled regions, an 8 μm × 8 μm area was first poled with -10 V dc bias, followed by a

smaller 4 μm × 4 μm area, within the negatively poled region, written with +10 V dc bias (figure 6.4d). The resulting domain pattern revealed a high piezoresponse amplitude signal in the entire region with a 180° phase contrast between the out-of-plane poled, antiparallel domains created by the ±10 V dc bias. These PFM measurements clearly show the robust quality of the VDF oligomer films and the creation, erasure, and switching of locally created ferroelectric domains. To ensure the piezoresponse amplitude and phase contrast shown in figures 6.4b-d are in fact due to a *ferroelectric* response, local piezoresponse hysteresis measurements were also performed on similar Si/Pt/VDF oligomer heterostructures. Figure 6.4e and 6.4f show the phase and piezoresponse amplitude from such a measurement, clearly demonstrating classic ferroelectric hysteresis. Figures 6.3a, 6.4e, and 6.4f demonstrate the switchable, ferroelectric behavior of the VDF oligomer on both macro- and microscopic scales.

Recall from figure 6.3 that the ferroelectric polarization was completely saturated before recording the time dependence of the polarization decay. Therefore, the data in figure 6.3 essentially corresponds to a ferroelectric domain with an area of 200 × 200 μm^2. Though the domains shown in figure 6.4 are smaller than 200 × 200 μm^2, they are still on the order of μm^2 and far larger than the critical domain size due to the depolarization field (on the order of nm^2) [34, 44]. Therefore, it is expected that the domains shown in figure 6.4 should have similar temporal stability as those corresponding to the data shown in figure 6.3.

6.4 Conclusions

This work confirms ferroelectricity in VDF oligomer thin films, and more importantly, establishes the existence of the ferroelectric-to-paraelectric phase transition. Calorimetry, pyroelectric, and capacitance measurements all clearly show a phase transition in both bulk powder and thin films on heating. C-V and I-V measurements clearly show the ferroelectric stability of these thermally evaporated VDF oligomer thin films. The ferroelectric polarization of these films can be repeatedly switched with low leakage. The spontaneous polarization of these VDF oligomer thin films is found to be 104 ± 2 mC/m^2, larger than that for PVDF and close to the value for P(VDF-TrFE). The remanent polarization is relatively stable, relaxing 13% to 17% in 12 hours, and relaxing more slowly after that. XRD measurements indicate that the as-grown state of these all-vacuum deposited VDF oligomer thin films are deposited in the ferroelectric β-phase with the optimal (020) crystalline orientation. Thus, not only is the interfacial cleanliness maintained by the vacuum deposition, but the out-of-plane component of the ferroelectric polarization is maximized, hence these films do not require post deposition processing. Lastly, PFM measurements show that ferroelectric domains can be written in VDF oligomer thin films and that the phase contrast between antiparallel, out-of-plane domains is high.

In summary, the work in this chapter establishes the viability of thermally evaporated VDF oligomer thin films for use in a variety of applications and devices. The spontaneous polarization rivals that of the VDF oligomer rivals that P(VDF-TrFE), but can be deposited in vacuum, preserving interfacial cleanliness. Furthermore, these measurements were made on large area samples, indicating the superior quality of the

thermally evaporated VDF oligomer films can be maintain across areas suitable for devices. The stable remanent polarization and excellent domain contrast open channels for non-volatile memory applications in particular, thus establishing the VDF oligomer as strong candidate material in the rapidly developing field of organic electronics.

6.5 Acknowledgements

Financial support is provided by the National Science Foundation (NSF) through the Nebraska Materials Research Science and Engineering Center (MRSEC) Grant No. DMR-1420645 and by NSF Grant No. ECCS-1101256. This research was performed in part in the Nebraska Nanoscale Facility: National Nanotechnology Coordinated Infrastructure and the Nebraska Center for Materials and Nanoscience, which are supported by the National Science Foundation under Award ECCS-1542182 and the Nebraska Research Initiative.

6.6 References

1. J. Hwang, A. Wan, and A. Kahn, Mater. Sci. Eng. R-Rep. **64**, 1 (2009)
2. G. Gu, V. Bulović, P. E. Burrows, S. R. Forrest, and M. E. Thompson, Appl. Phys. Lett. **68**, 2606 (1996)
3. C. Hochfilzer, G. Leising, Y. Gao, E. Forsythe, and C. W. Tang, Appl. Phys. Lett. **73**, 2254 (1998)
4. S. Tokito, T. Tsutsui, and Y. Taga, J. Appl. Phys. **86**, 2407 (1999)
5. J. Song, H. Lu, K. Foreman, S. Li, L. Tan, S. Adenwalla, A. Gruverman and S. Ducharme, J. Mater. Chem. C, 4, 5914 (2016)

6. K. Fujita, T. Yasuda, and T. Tsutsui, Appl. Phys. Lett. **82**, 4373 (2003)
7. F. Eder, H. Klauk, M. Halik, U. Zschieschang, G. Schmid, and C. Dehm, Appl. Phys. Lett. **84**, 2673 (2004)
8. A. Mardana, S. Ducharme, and S. Adenwalla, Nano Lett. **11**, 3862 (2011)
9. P. V. Lukashev, T. R. Paudel, J. M. López-Encarnación, S. Adenwalla, E. Y. Tsymbal, and J. P. Velev, ACS Nano **6**, 9745 (2012)
10. R.-Q. Wang, W.-J. Zhu, H.-C. Ding, S.-J. Gong, and C.-G. Duan, J. Appl. Phys. **115**, 043909 (2014)
11. L. E. Cross, Mater. Chem. Phys. **43**, 108 (1996)
12. M. Ye. Zhuravlev, R. F. Sabirianov, S. S. Jaswal, and E. Y. Tsymbal, Phys. Rev. Lett. **94**, 246802 (2005)
13. A. Q. Jiang, C. Wang, K. J. Jin, X. B. Liu, J. F. Scott, C. S. Hwang, T. A. Tang, H. B. Lu, and G. Z. Yang, Adv. Mater. **23**, 1277 (2011)
14. T. Furukawa, Phase Transitions **18**, 143 (1989)
15. Y. Pei and X. C. Zeng, J. Appl. Phys. **109**, 093514 (2011)
16. T. Furukawa, M. Date, and E. Fukada, J. Appl. Phys. **51**, 1135 (1980)
17. K. Tashiro, *Ferroelectric Polymers: Chemistry, Physics, and Applications*, edited by H. S. Nalwa (Marcel Dekker, Inc., New York, 1995)
18. M. Poulsen and S. Ducharme, IEEE Trans. Dielectr. Electr. Insul. **17**, 1028 (2010)
19. K. Noda, K. Ishida, T. Horiuchi, K. Matsushige, and A. Kubono, J. Appl. Phys. **86**, 3688 (1999)
20. K. Noda, K. Ishida, A. Kubono, T. Horiuchi, H. Yamada, and K. Matsushige, J. Appl. Phys. **93**, 2866 (2003)

21. S. Palto, L. Blinov, A. Bune, E. Dubovik, V. Fridkin, N. Petukhova, K. Verkhovskaya, and S. Yudin, Ferroelectr. Lett. **19**, 65 (1995)

22. S. J. Kang, Y. J. Park, J. Sung, P. S. Jo, C. Park, K. J. Kim, and B. O. Cho, Appl. Phys. Lett. **92**, 012921 (2008)

23. K. Foreman, E. Echeverria, M. A. Koten, R. M. Lindsay, N. Hong, J. Shield, and S. Adenwalla, Mater. Res. Express **3**, 116403 (2016)

24. K. Foreman, C. Labedz, M. Shearer, and S. Adenwalla, Rev. Sci. Instrum. **85**, 043902 (2014)

25. K. Foreman, N. Hong, C. Labedz, M. Shearer, S. Ducharme, and S. Adenwalla, J. Phys. D: Appl. Phys. **49**, 015301 (2016)

26. A. Takeno, N. Okui, T. Kitoh, M. Muraoka, S. Umemoto, and T. Sakai, Thin Solid Films **202**, 205 (1991)

27. A. V. Bune, C. Zhu, S. Ducharme, L. M. Blinov, V. M. Fridkin, S. P. Palto, N. G. Petukhova, and S. G. Yudin, J. Appl. Phys. **85**, 7869 (1999)

28. M. E. Lines and A. M. Glass, *Principles and Applications of Ferroelectrics and Related Materials* (Clarendon, Oxford, 1977)

29. A. G. Chynoweth, J. Appl. Phys. **27**, 78 (1956)

30. C. A. Schneider, W. S. Rasband, and K. W. Eliceiri, Nature Methods **9**, 671 (2012)

31. T. Furukawa, G. E. Johnson, H. E. Bair, Y. Tajitsu, A. Chiba, and E. Fukada, Ferroelectrics **32**, 61 (1981)

32. T. Furukawa, Ferroelectrics **57**, 63 (1984)

33. R. G. Kepler and R. A. Anderson, Adv. Phys. **41**, 1 (1992)

34. A. V. Bune, V. M. Fridkin, S. Ducharme, L. M. Blinov, S. P. Palto, A. V. Sorokin, S. G. Yudin, and A. Zlatkin, Nature **391**, 874 (1998)
35. L. L. Sun, B. Li, Y. Zhao, G. Mitchell, and W. H. Zhong, Nanotechnology **21**, 305702 (2010)
36. B. Balasubramanian, K. L. Kraemer, S. R. Valloppilly, S. Ducharme, and D. J. Sellmyer, Nanotechnology **22**, 405605 (2011)
37. H. Ohigashi, K. Omote, and T. Gomyo, Appl. Phys. Lett. **66**, 3281 (1995)
38. Herman, S. Umemoto, T. Kikutani, and N. Okui, Polym. J. **30**, 659 (1998)
39. M. Bai and S. Ducharme, Appl. Phys. Lett. **85**, 3528 (2004)
40. R. Korlacki, J. T. Johnson, J. Kim, S. Ducharme, D. W. Thompson, V. M. Fridkin, Z. Ge, and J. M. Takacs, J. Chem. Phys. **129**, 064704 (2008)
41. P. Sharma, S. Poddar, R. Korlacki, S. Ducharme, and A. Gruverman, Appl. Phys. Lett. **105**, 022906 (2014)
42. A. Bune, S. Ducharme, V. Fridkin, L. Blinov, S. Palto, N. Petukhova, and S. Yudin, Appl. Phys. Lett. **67**, 3975 (1995)
43. A. V. Sorokin, V. M. Fridkin, and S. Ducharme, J. Appl. Phys. **98**, 044107 (2005)
44. J. Junquera and P. Ghosez, Nature **422**, 506 (2003)

CHAPTER 7

THE FUTURE OF THE VINYLIDENE FLUORIDE OLIGOMER: REMAINING CHALLENGES, FUTURE EXPERIMENTS, AND POSSIBLE APPLICATIONS

7.1 Introduction

Thus far, this dissertation has thoroughly explored the successful deposition of VDF oligomer thin films, reported on various material and ferroelectric properties of these films, and investigated the interface between these films and metallic thin films. This overview-style chapter will provide an outlook on the future of the VDF oligomer by underscoring several remaining challenges associated with this material and then briefly highlighting possible future experiments and/or technological applications of VDF oligomer thin films using real, proof-of-concept data.

7.2 Remaining Challenges and Questions Concerning the VDF Oligomer

Chief among the remaining challenges associated with the VDF oligomer is improving sample yield which, in turn, requires ever increasing understanding of the deposition parameter space. In Chapter 4, successful sample yield was related to the deposition parameters via film topography, the understanding of which led to a marked increase in yield. Still, the successful yield of the VDF oligomer thin films is far below that of LB deposited P(VDF-TrFE) films. It is not unreasonable to expect a near 100% successful yield for the LB films, while a generous estimate of successful yield of VDF oligomer thin films is no greater than about 75%. Using the definition of "successful yield" given in Chapter 4, this means that one of four metal/VDF oligomer/metal

junctions fails unpredictably. Though highly inconvenient, this failure rate does not necessarily prohibit fundamental research involving the VDF oligomer. However, this failure rate must be addressed should VDF oligomer thin films ever be used in devices.

A related problem is the lack of reliability of large area ($> 3 \times 3$ mm^2) VDF oligomer films, an issue that was also mentioned in Chapter 4. The sample architecture shown in figure 4.7a would be well-suited for Polarized Neutron Reflectometry (PNR) (which will be discussed below). However, over such large areas, the $1/r^2$ thickness variation in the VDF oligomer film plays a similar role to roughness and causes failure. Indeed, on several occasions, damage was observed in real-time propagating from the edges of such a sample towards the center, i.e. from the region of thinnest VDF oligomer to the region of thickest VDF oligomer, upon the application of voltage.

Both of the above problems could possibly be addressed by a redesign/rebuild of the organic thermal evaporator detailed in Chapter 3. Increasing the distance between the sample and the effusion cell would help reduce the $1/r^2$ curvature of large area films. Furthermore, many deposition systems, including the sputtering system used in this work, are capable of substrate rotation to ensure even film deposition. The thermal evaporator described in Chapter 3 is not capable of substrate rotation, and adding this capability may greatly increase film uniformity. Admittedly, however, designing a chamber that is simultaneously capable horizontal sample transport, sample loading and unloading, vertical sample-stage motion, liquid nitrogen substrate cooling, *and* substrate rotation would be quite the engineering feat.

The surface roughness problem may also be solved post deposition. Figure 7.1a shows an AFM image of a rough VDF oligomer thin film after deposition at a high

crucible temperature, similar to that shown in figure 4.3a. The maximum peak-to-valley distance, Δz, of this VDF oligomer film is 71 nm. However, prior to the deposition of a top electrode, approximately 25 nm of polyethylene was deposited onto the VDF oligomer via LB deposition. Figure 7.2b shows an AFM image of the sample after the deposition of the polyethylene. After the deposition of the polyethylene, Δz is 18 nm, a decrease of 53 nm. A top electrode was then deposited to attempt to measure the pyroelectric hysteresis. Although some pyroelectric current was measured, a full hysteresis loop was not collected before sample failure.

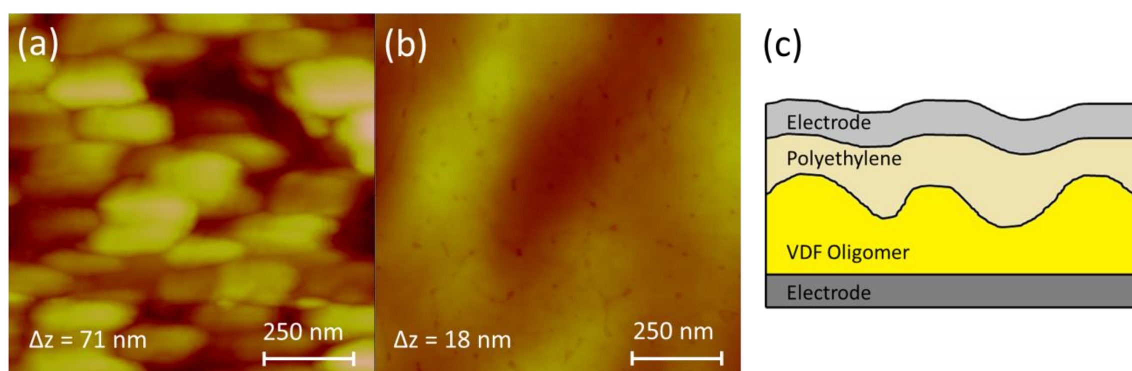

Figure 7.1: (a) AFM image of VDF oligomer thin film surface. (b) AFM image of LB deposited polyethylene surface atop the VDF oligomer film in part (a). (c) Illustration of possible sample cross-section depicted a smooth top electrode.

Figure 7.1c depicts a possible mechanism for the improved surface roughness and thus, improved successful yield. A top electrode deposited on top of the LB deposited polyethylene in figure 7.1b will be, on average, smoother than if it were deposited directly on the VDF oligomer in figure 7.1a. If a voltage is then held across the film, the

magnitude of the resulting electric field may be more uniform, in contrast to the situation depicted in figure 4.4, and the sample may be more robust and reliable.

It should be noted, however, that only about three total attempts were made to deposit polyethylene on VDF oligomer thin films, far too few attempts to draw any definitive conclusions. Figure 7.1 merely demonstrates a proposed, possible approach to improve successful yield, and it may be worthwhile investigating samples of this type more thoroughly.

Another challenge/open question that may be related to successful yield concerns microscopic defects in the films. For example, usually the $–CH_2$ side of one monomer, or "head", is connected to the $–CF_2$ side, or "tail", of the next monomer along the chain, as depicted in figure 1.9. However, reversal of a monomer results in a head-to-head and tail-to-tail defect along the chain. One study reports that these defects may occur as often as 1 in 10 monomeric units in PVDF [1]. Furthermore, these defects have been shown to affect, at the very least, the crystal structure, phase transition, and the magnitude of the dipole moment per monomer [2, 3]. Microscopic defects, such as head-to-head and tail-to-tail defects, have never been addressed or investigated in the bulk VDF oligomer powder and the effect of these defects on thin film performance remains an open question.

7.3 Magnetoelectric Coupling

Voltage-controlled magnetism is of major scientific interest [4-6] due to the interesting fundamental physics governing the effect as well as potential technological applications utilizing such control. Voltage-controlled magnetic anisotropy has been

predicting theoretically in Co/PVDF heterostructures [7] and observed experimentally in Co/P(VDF-TrFE) heterostructures [8]. In these structures, the ferroelectric material is in intimate contact with the ferromagnetic thin films. At the surface of the metallic, ferromagnetic thin film, electrostatic screening of the electric field associated with the polarization of the ferroelectric layer modifies the *d*-orbital occupancy of the transition metal [9]. Since the metallic layer is ferromagnetic, the screening charge is spin polarized [7, 10]. Thus, the electric field causes unequal screening for spin-up and spin-down electrons at the interface [7, 8, 10, 11]. The spin-dependence of screening charge can change the magnetocrystalline anisotropy energy by up to 50% upon repolarization of the ferroelectric material [7, 8]. If the thickness of the ferromagnetic layer is chosen carefully, this change in magnetocrystalline anisotropy energy may lead to a change in the easy-axis direction, essentially coupling the ferromagnetic magnetization to the ferroelectric polarization [7].

Given the similarity between PVDF and the VDF oligomer, one should expect to observe similar magnetoelectric coupling in Co/VDF oligomer heterostructures. Figure 7.2 shows evidence of magnetoelectric coupling in a glass/Pt (50 nm)/Co (1 nm)/VDF (150 nm)/Al (20 nm) heterostructure. Out-of-plane magnetic hysteresis was measured using the PMOKE setup shown in figure 2.9 for each ferroelectric polarization state of the VDF oligomer. There is a clear difference in the magnetic hysteresis for each polarization state, an indication of magnetoelectric coupling.

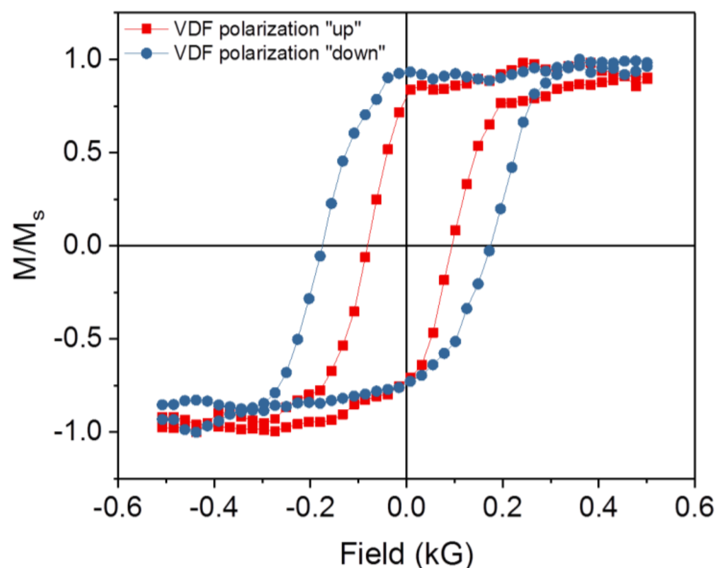

Figure 7.2: Demonstration of magnetoelectric coupling in Co/VDF oligomer heterostructures.

Though preliminary results show magnetoelectric coupling in Co/VDF heterostructures, more work is needed to elucidate the magnitude of the effect. For example, PMOKE (out-of-plane) and LMOKE (in-plane) magnetic hysteresis measurements for both ferroelectric polarization states measured from the same heterostructure are needed to determine the change in anisotropy energy (via the "area method" [12]). A principle challenge concerning these measurements is associated with the presence of the metallic top electrode needed to polarize the VDF oligomer. The metallic electrode attenuates the signal from the laser used in the MOKE measurements, resulting in a dramatically reduced signal-to-noise ratio, especially in the LMOKE configuration where the incident angle of the laser is far from normal. This attenuation problem could possibly be addressed by finding alternative top electrodes that will allow more light to be transmitted, such as indium tin oxide or poly(3,4-

ethylenedioxythiophene), commonly known as PEDOT, both of which are transparent conductors.

Although there are still challenges to overcome, the data shown in figure 7.2 foreshadows exciting research involving the VDF oligomer in the realm of voltage-controlled magnetism.

7.4 Polarized Neutron Reflectometry

During a PNR measurement, spin polarized neutrons are reflected off a sample at grazing incidence and the reflectivity of the spin up ($\mathbf{R}^{\uparrow}$) and spin down ($\mathbf{R}^{\downarrow}$) neutrons are measured as a function of momentum transfer, Q [13]:

$$Q = \frac{4\pi}{\lambda} \sin\theta \tag{7.1}$$

where λ is the wavelength of the neutrons (which can be comparable to interatomic distances) and θ is the angle of incidence. Since neutrons have a magnetic moment, this technique can be used to measure a magnetic depth profile of the sample [13]. The reflectivity of the neutrons depends on the orientation between the magnetization of the sample and the neutron spin. Therefore, the reflectivity of spin up and spin down neutrons is different for certain orientations, and the spin asymmetry, given by:

$$Spin\ Asymmetry = {(R^{\uparrow} - R^{\downarrow})}/{(R^{\uparrow} + R^{\downarrow})} \tag{7.2}$$

is a measure of the magnetization of the sample. Specifically, due to magnetic field boundary conditions, the spin asymmetry is a measure of the in-plane component of the magnetization.

Using the free-to-download program reflpol, made available by NIST [14], PNR data can be simulated for the Co/VDF oligomer heterostructures used throughout this work. Figure 7.3a shows the reflectivity profile for both spin up and spin down neutrons from a heterostructure in which the magnetization of the Co was constrained to be in the plane of the sample, while figure 7.3b shows the reflectivity profile from a heterostructure in which the magnetization was constrained to be out of the plane of the sample. From these simulations, the spin asymmetry for both magnetization states can be calculated, as shown in figure 7.3c. As expected, there is a large spin asymmetry for the in-plane magnetization case, and little spin asymmetry for the out-of-plane case.

From figure 7.3c, it is apparent that PNR is highly sensitive to changes to the in-plane component of magnetization. Granted, the simulation assumed a highly idealized, full 90° rotation of the magnetization, but PNR is still sensitive enough to detect very small changes in magnetization. Therefore, PNR measurements should be able to detect any changes in the magnetization of the Co due to repolarization of the ferroelectric VDF oligomer in the Co/VDF oligomer heterostructures.

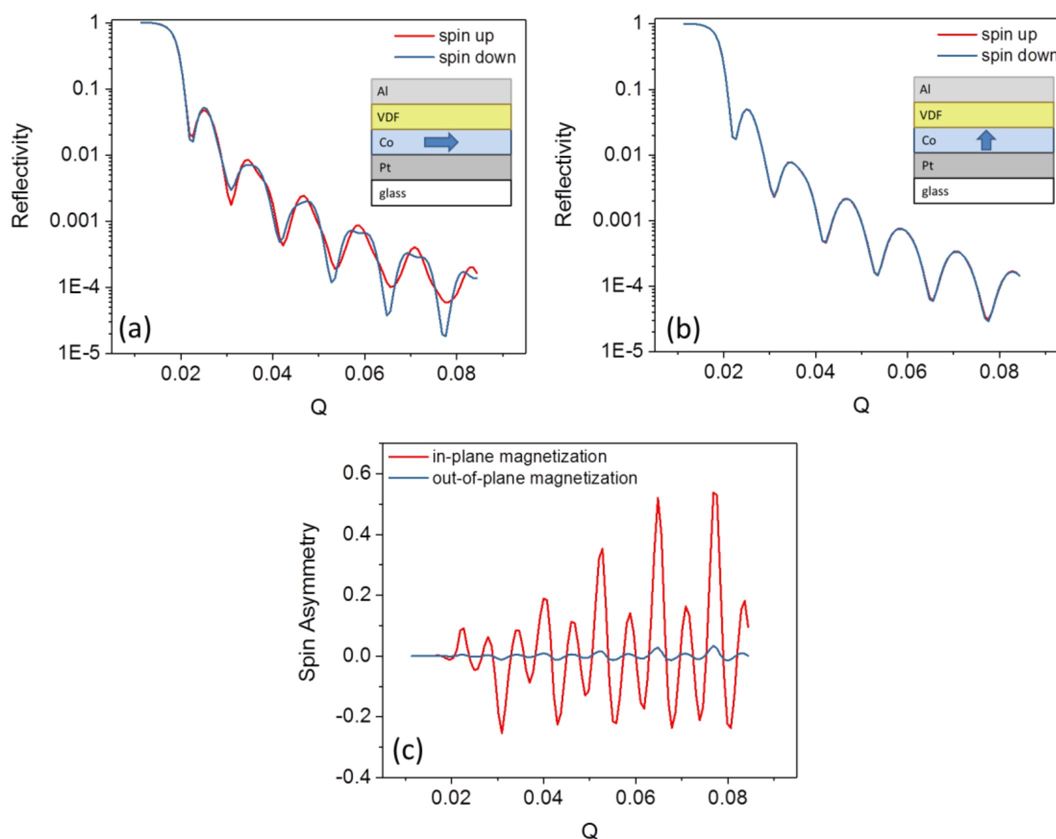

Figure 7.3: (a) PNR profile for a Co/VDF oligomer heterostructure with in-plane Co magnetization. (b) PNR profile for a Co/VDF oligomer heterostructure with out-of-plane Co magnetization. (c) spin asymmetry calculated from the simulations in parts (a) and (b).

The advantage of using PNR to look for magnetoelectric coupling rather than MOKE is that the spin polarized neutrons are insensitive to the presence of the top, metallic electrode. The disadvantage, as described in section 7.2 above, is that the measurement requires a somewhat large area sample (1 cm^2). Currently, these large area samples suffer from a large thickness variation in the VDF oligomer, and subsequently have a low yield as described in Chapter 4.

Ideally, future experiments on magnetoelectric coupling in these Co/VDF oligomer heterostructures would not rely exclusively on MOKE or PNR alone, but rather both measurement techniques acting in concert.

7.5 Ferroelectric Tunnel Junctions

Ferroelectric tunnel junctions (FTJs) have drawn considerable interest due to the potential technological applications of such devices [15, 16]. An FTJ is a device with two distinct resistance states associated with the polarization state of the ferroelectric material. Thus, the resistance can be switched from "high" to "low" or vice versa by repolarizing the ferroelectric layer. Since the polarization of the ferroelectric material is maintained even in the absence of an external electric field, an externally applied voltage is not necessary to maintain the resistance state. Therefore, FTJs are well-suited for non-volatile memory applications.

The effect responsible for this switchable resistance is tunneling electroresistance (TER), which can be understood as follows. The metallic electrodes in an FTJ are made of different materials that have different charge screening lengths. Therefore, the electrostatic potential profile that electrons encounter when tunneling from one electrode to the other across the ferroelectric tunneling barrier is asymmetric, i.e. different for each ferroelectric polarization state [15]. This polarization dependence of the potential profile leads to different tunneling probabilities for each polarization state, and thus, different resistances.

Figure 7.4 shows the resistance measured across a glass/Pt (50 nm)/Co (1 nm)/VDF (15 nm)/Al (30 nm) heterostructure for both ferroelectric polarization states of

the VDF oligomer thin film. There is a clear change in resistance upon repolarization of the VDF oligomer. Linear fitting is used to find the resistance, and the TER ratio is found using [17]:

$$TER = \frac{R_{\uparrow} - R_{\downarrow}}{R_{\downarrow}} \times 100\% \tag{7.3}$$

where $R_{\uparrow}$ and $R_{\downarrow}$ are the resistances measured when the VDF oligomer is polarized in the "up" direction (polarization vector pointing towards the top electrode) and the "down" direction (polarization pointing towards the bottom electrode), respectively. Using equation 7.3, the TER ratio for the data shown in figure 7.4 is found to be 1,425%.

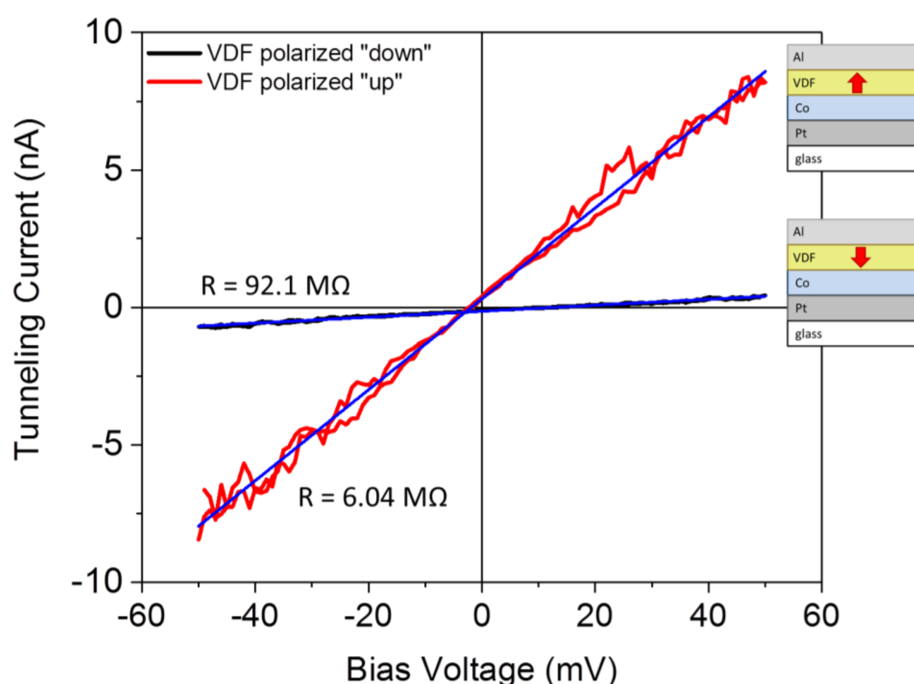

Figure 7.4: Demonstration of resistance dependence on VDF oligomer polarization, possibly due to the TER effect. Linear fits are shown in blue.

Two things should be noted about the data shown in figure 7.4. First, the tunneling barrier, in this case the 15-nm thick VDF oligomer film, was rather thick compared to barriers in other studies, which are often less than 10 nm thick [15-17]. Secondly, the TER ratio, 1,425%, is also rather large compared to other studies, which usually report (room temperature) values ranging from 10% to 100% [18, 19]. These factors may cast doubt on whether the change in resistance shown in figure 7.4 is truly due to the TER effect. Nevertheless, the results do indicate a clear change in resistance upon repolarization, making this avenue of research regarding the VDF oligomer a worthwhile future endeavor.

7.6 Conclusions

This work has undertaken an exploration of the organic ferroelectric VDF oligomer. In this dissertation, it was demonstrated that the VDF oligomer thin films can be deposited in its ferroelectric phase in vacuum conditions, preserving the interface with adjacent layers. Material and ferroelectric properties were reported for the first time, including the existence of the ferroelectric-to-paraelectric phase transition.

This chapter validates those efforts to grow, optimize, and characterize VDF oligomer thin films, and demonstrate possible returns on these efforts in the near future. Though there are still challenges and unanswered questions regarding the VDF oligomer, the proof-of-concept measurements presented here illuminate paths of future research on this interesting and useful material.

7.7 References

1. C. W. Wilson III and E. R. Santee Jr., J. Polym. Sci. Part C **8**, 97 (1965)

2. A. J. Lovinger, Science **220**, 1115 (1983)

3. A. J. Lovinger, D. D. Davis, R. E. Cais, J. M. Kometani, Polymer **28**, 617 (1987)

4. H. Ohno, D. Chiba, F. Matsukura, T. Omiya, E. Abe, T. Dietl, Y. Ohno, and K. Ohtani, Nature **408**, 944 (2000)

5. M. Bibes and A. Barthélémy, Nat. Mater. **7**, 425 (2008)

6. R.-Q. Wang, W.-J. Zhu, H.-C. Ding, S.-J. Gong, and C.-G. Duan, J. Appl. Phys. **115**, 043909 (2014)

7. P. V. Lukashev, T. R. Paudel, J. M. Lopez-Encarnacion, S. Adenwalla, E. Y. Tsymbal, and J. P. Velev, ACS Nano **6**, 9745 (2012)

8. A. Mardana, S. Ducharme, and S. Adenwalla, Nano Lett. **11**, 3862 (2011)

9. J. Zhang, P. V. Lukashev, S. S. Jaswal, and E. Y. Tsymbal, arXiv:1612.02724 [cond-mat.mtrl-sci]

10. S. Zhang, Phys. Rev. Lett. **83**, 640 (1999)

11. T. Cai, S. Ju, J. Lee, N. Sai, A. A. Demkov, Q. Niu, Z. Li, J. Shi, and E. Wang, Phys. Rev. B **80**, 140415(R) (2009)

12. M. T. Johnson, P. J. H. Bloemen, F. J. A. den Broeder, and J. J. de Vries, Rep. Prog. Phys. **59,** 1409 (1996)

13. C. F. Majkrzak, K. V. O'Donovan, and N. F. Berk, *Polarized Neutron Reflectometry*, National Institute of Standards and Technology, available at: https://www.ncnr.nist.gov/staff/hammouda/distance_learning/pnrchapti.pdf

14. Available at: https://www.ncnr.nist.gov/reflpak/release/reflpak-2003.11.05/INSTALL.html

15. M. Ye. Zhuravlev, R. F. Sabirianov, S. S. Jaswal, and E. Y. Tsymbal, Phys. Rev. Lett. **94**, 246802 (2005)

16. M. Ye. Zhuravlev, Y. Wang, S. Maekawa, and E. Y. Tsymbal, Appl. Phys. Lett. **95**, 052902 (2009)

17. Y. W. Yin, J. D. Burton, Y.-M. Kim, A. Y. Borisevich, S. J. Pennycock, S. M. Yang, T. W. Noh, A. Gruverman, X. G. Li, E. Y. Tsymbal, and Q. Li, Nat. Mater. **12**, 397 (2013)

18. Y.-W. Yin, M. Raju, W.-J. Hu, X.-J. Weng, K. Zou, J. Zhu, X.-G. Li, Z.-D. Zhang, and Q. Li, Front. Phys. **7**, 380 (2012)

19. V. Garcia *et al*. Science, **327**, 1106 (2010)

APPENDIX A

X-RAY PHOTOELECTRON SPECTROSCOPY DATA ANALYSIS

XPS spectra were collected on Co/VDF heterostructures prepared with and without breaking vacuum after the Co deposition. As the Ar^+ ion etch removed Co material, the signal associated with the Co(2p) peak became weaker. To find the positions of the Co(2p) peaks for the spectra taken close to the Co/Pt seed layer interface, the individual spectra were first run through a 20 point smoothing algorithm. Figure A.1a shows an as-collected spectrum (black line) and a smoothed spectrum (red line). Once smoothed, the first derivative is taken to better identify the peak location. Figure A.1b shows the first derivative of both an as-collected spectrum (black line) and the first derivative of a smoothed spectrum (red line). A Gaussian peak is then fit to the first derivative of the smoothed spectra to find the location of the peaks. An example is shown in figure A.1c.

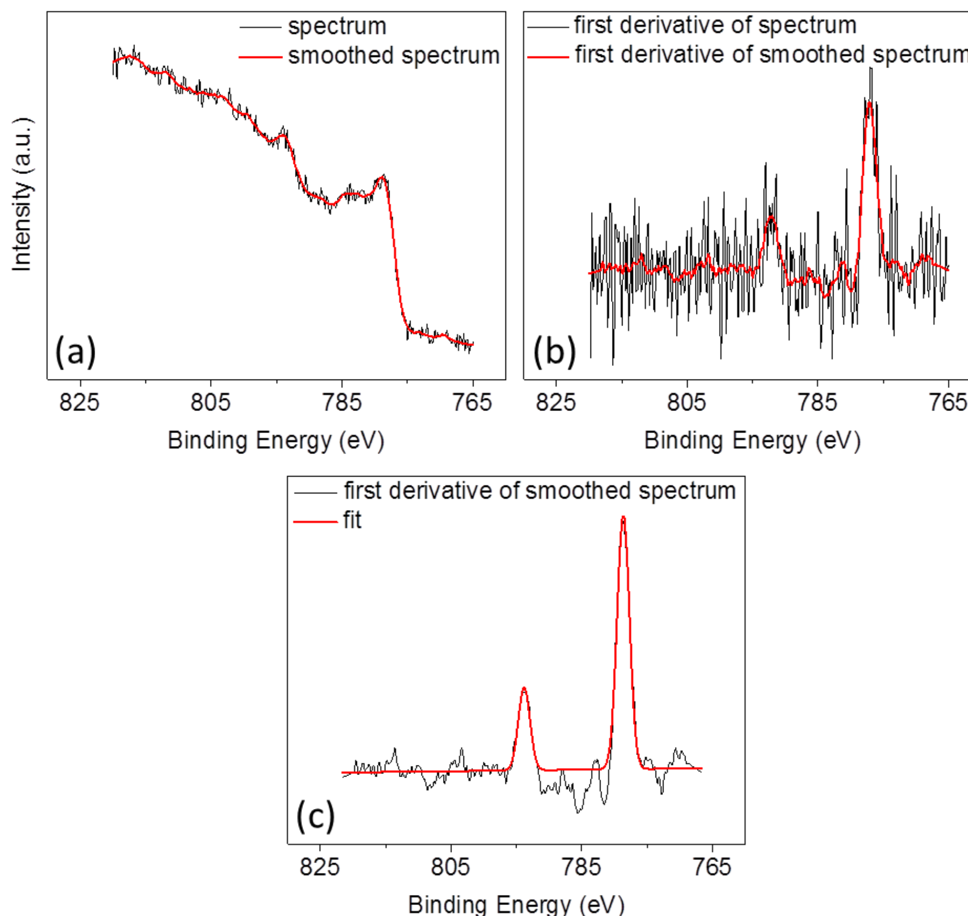

Figure A.1: Peak extraction for Co(2p) spectra collected close to the Co/Pt interface. (a) Example of Co(2p) spectrum, both as-collected (black) and smoothed (red). (b) First derivative of as-collected (black) and smoothed (red) spectrum. (c) First derivative smoothed Co(2p) spectrum (black) and Gaussian fit (red).

For Co(2p) depth profiling, such as that shown in figure 5.6 of Chapter 5, the Pt(4f) peak was monitored throughout data collection. Figure A.2 shows the Pt(4f) spectra collected after each Ar^+ ion etch, indicating a very small peak which increases in height as material is etched away. When the height of the Pt(4f) peak saturates, the Ar^+

etch has reached the Pt layer, and spectra collection is stopped. PMOKE measurements on these samples after XPS measurements confirm this, as they show no magnetic signal, confirming the etching of the Co.

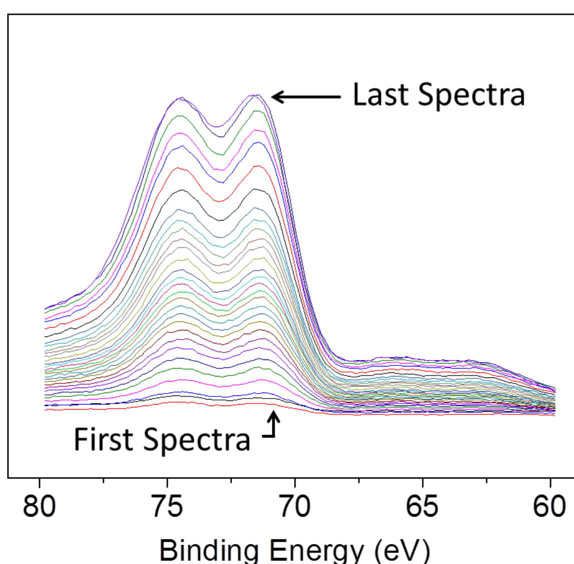

Figure A.2: XPS spectra of Pt(4f) peaks. Between each spectrum, material is etched away, and the magnitude of the peak increases. When the intensity of the Pt(4f) peak stops increasing after subsequent etches, it is assumed that the etching process has reached the Pt seed layer and no Co remains.

For the F(1s) depth profiling, such as that shown in figure 5.7 of Chapter 5, the F(1s) peak was monitored throughout data collection. Figure A.3 shows the F(1s) spectra collected after each Ar^+ ion etch. The peak starts large, with its magnitude remaining relatively large after each Ar^+ ion etch, until enough VDF oligomer has been removed that the spectra are collected near the Co/VDF interface. As the interface is approached,

the F(1s) peak begins to diminish, and when it disappears entirely, it is inferred that the VDF oligomer film has been etched away and the Co/VDF interface has been reached.

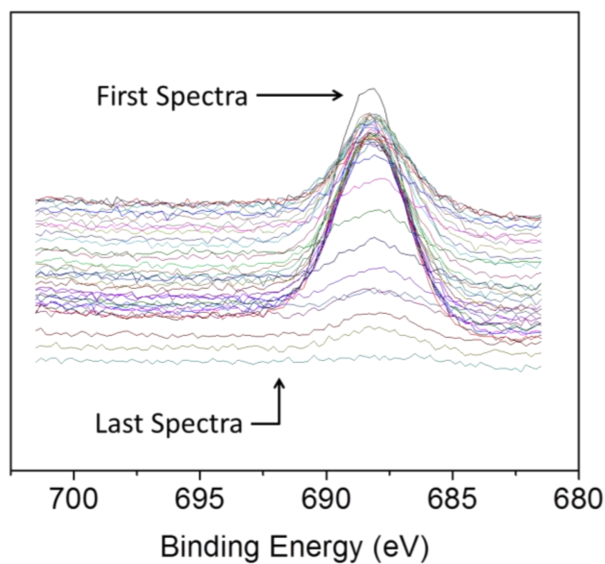

Figure A.3: XPS spectra of F(1s) peaks. Between each spectrum, VDF oligomer is etched away, and the magnitude of the peak decreases. When the intensity of the F(1s) peak disappears, it is assumed that the etching process has reached the Co/VDF interface, and no VDF oligomer remains.

APPENDIX B

SELECT PRESENTATIONS

Ferroelectric Properties of Large Area Evaporated Vinylidene Fluoride Thin Films

March Meeting of the American Physical Society, New Orleans, Louisiana

March 13th – 17th, 2017

Magnetoelectric Coupling and Interfacial Effects in Organic Ferroelectric/Metallic Ferromagnetic Heterostructures

13th Joint Intermag/Magnetism and Magnetic Materials Conference, San Diego, California

January 11th – 15th, 2016

Electric-Field Control of Magnetization in Metal/Organic Heterostructures (poster)

Materials for Energy Systems Symposium, Lincoln, Nebraska

July 21st, 2015

Ferroelectric Influence on Magnetic Anisotropy in Organic Ferroelectric/Co Heterostructures

March Meeting of the American Physical Society, Denver, Colorado

March 3rd – 7th, 2014

Ferroelectric Control of Magnetic Anisotropy in a Co/P(VDF-TrFE) Heterostructure (poster)

Fundamental Physics of Ferroelectrics and Related Materials, Ames, Iowa

January 27th – 30th, 2013

Ferroelectric Control of Magnetic Anisotropy in a Co/P(VDF-TrFE) Heterostructure

12th Joint Intermag/Magnetism and Magnetic Materials Conference, Chicago, Illinois

January 14th – 18th, 2013

Ferroelectric Control of Magnetic Anisotropy in a Co/P(VDF-TrFE) Heterostructure: A Polarized Neutron Reflectometry Study (poster)

Nebraska Research and Innovation Conference, Lincoln, Nebraska

October 9th, 2012